EXPERIMENTAL CHARACTERIZATION OF AEROSOL FLOW THROUGH MICRO-CAPILLARIES

A Thesis
Submitted to the Graduate Faculty
of the
North Dakota State University
of Agriculture and Applied Science

By

Michael Jake Robinson

In Partial Fulfillment of the Requirements
for the Degree of
MASTER OF SCIENCE

Major Department:
Mechanical Engineering and Applied Mechanics

October 2012

Fargo, North Dakota

North Dakota State University
Graduate School

Title

Experimental Characterization of Aerosol Flows

Through Micro-Capillaries

By

Michael Jake Robinson

The Supervisory Committee certifies that this ***disquisition*** complies with North Dakota State University's regulations and meets the accepted standards for the degree of

MASTER OF SCIENCE

SUPERVISORY COMMITTEE:

Dr. Iskander Akhatov
Chair

Dr. Orv Swenson

Dr. Bora Suzen

Dr. Zakaria Mahmud

Approved:

11/7/2012	Dr. Alan Kallmeyer
Date	Department Chair

ABSTRACT

Understanding the forces which dictate fluid particle interaction is of high interest in the field of aerosol jet Direct Write (DW). Several methods utilizing shadowgraphy and Mie scattering were used to visualize particle flow exiting micro-capillaries. Experiments were designed such that results would offer insight into the effects of Stokes and Saffman force on particle trajectories. Comparison to these results allowed for the development of a theoretical model which was validated and used to optimize nozzle geometries for particle focusing. Optimized nozzle geometries resulted in the conclusion that under certain conditions Saffman force is applicable given an appropriate correction factor. Experimental results showed the successful collimation of aerosol particles into beams with widths as small as the particles diameter. Additionally, a Small Particle Sizing Algorithm (SPSA) utilizing standard shadowgraphy techniques was developed allowing for the simultaneous sizing and positioning of particles ranging from 3-10 µm in diameter.

ACKNOWLEDGMENTS

I would like to express my appreciation to those who offered advice, guidance and support during the pursuit of my graduate degree. First, I would like to acknowledge my committee advisor, Iskander Akhatov. This work is a direct result of his inspiration and leadership. Additionally, the remaining committee members, Orven Swenson, Zakaria Mahmud and Bora Suzen, deserve recognition for their support of this research as well as their contributions in the classroom. I also recognize the contributions from all the professors and assistants in the Mechanical Engineering Department and North Dakota State University for their contributions to my continued education.

The remaining members of my research group, Artur Lutfurakhmanov, Sourin Bhattacharya, and Jake Fink also deserve recognition. Special recognition is given to Justin Hoey. Without his efforts, this research could not have been accomplished. I would also like to thanks the remaining CNSE employees whom I was fortunate to collaborate with during this research.

Finally and most importantly I would like to express my deepest appreciation and thanks to my family, who has challenged, supported and cared for me my entire life. My siblings Matthew, Lisa and Amy are and will always be my best friends. None could ask for a better role model than my father, Dr. Monty Robinson. And finally, my mother Carol Robinson, to whom this work is dedicated, has been the most loving and caring person that I have ever known. Thank you for making me the person I am today.

TABLE OF CONTENTS

LIST OF TABLES

LIST OF FIGURES

LIST OF SYMBOLS

a	Particle radius
C_{Sa}	Saffman correction factor
d	Particle diameter
dt	Davis software setting for time between laser pulses
$\mathbf{e}_y$	Unit vector along the y-axis
$\sum \mathbf{F}$	Sum of all forces acting on particle
$\mathbf{F}_{Sa}$	Saffman force
$\mathbf{F}_{St}$	Stokes force
G_{LB}	Local background intensity
G_{LT}	Gray level threshold intensity
G_{OM}	Object minimum background
GI	Gradient indicator
Re_f	Shear Reynolds number
Re_p	Particle Reynolds number
$\boldsymbol{t}$	Threshold value in Otsu's method
u	Axial component of gas velocity
u_p	Axial component of particle velocity
$\mathbf{v}$	Velocity vector of the carrier gas
$\mathbf{v}_p$	Velocity vector of particle
VC	Normalized value of contrast

$\boldsymbol{w_i}$	Probabilities of classes in Otsu's method
Δt	Experimentally measured time between laser pulses
$\boldsymbol{\sigma_i^2}$	Variance of class in Otsu's method
ρ	Gas density
ρ_p	Particle density
λ	Wavelength of light

1. INTRODUCTION

In a scientific community where yesterday's technology is archaic and tomorrow's impossible, the demand for new and innovative practices regarding all aspects of research and development is extraordinarily high. In no sector is this demand more prevalent than in electronics, and specifically microelectronics. Additionally, calls to reduce carbon footprints and operate in a manner consistent with sustainable practices have also spurred further research into "green" technologies such as photovoltaics and solar cells. Unfortunately, technological advancements in microelectronics and photovoltaics are frequently stifled by the need for smaller faster and more efficient devices. Efforts to overcome these bottlenecks can be made on numerous levels such as material selection, component interaction and feature size control. Feature size is determined by a number of factors beginning with the method by which the features are created. Aerosol jet Direct Write (DW) is a method which allows for rapid prototyping and has applications in roll to roll processes. Additionally, aerosol jet technologies are free of some of the challenges associated with other techniques. While lithography can create features on the nanoscale (compared to DW which operates in the sub-micron to millimeter regime [1]), it is an expensive process as it requires cleanroom processes. Tip based depositions require direct contact with substrates, which can cause damage to both tip and substrate. Energy beam techniques sometimes have the ability to create 3-D features but do so at a rate on the order of µm per second. Flow based methods use a syringe through which flow is induced by a pressure differential. Materials with low viscosities tend to leak and materials with high viscosity require pressures large enough such that it is considered dangerous to the operator. Aerosol jet printing offers an alternative DW method which has the ability to compete with existing technologies due to its high printing rate (up to 200 mm/sec), non-invasive deposition method, and the variety of materials that can be deposited [1].

This research is part of an effort to gain understanding about the focusing forces present in micro-capillaries. Once understood these forces can be used to create perfectly collimated particle beams which would result in the ability to decrease printable feature size. The goals of this thesis were three fold. First, various visualization tools were investigated which served to gather information such as beam width and particle velocity. Second, once determined as accurate experimental processes, the tools were used to gather the required information to validate a theoretical model which accounts for the relevant focusing forces and predicts particle trajectories. This model could then be used to develop an optimized geometry for collimating particles under varying conditions such as size, flow rate and material. Third and finally, the experimental tools were used to confirm if that model was accurately predicting the particle trajectories for new nozzle geometries and conditions. The tools used were shadowgraphy, Mie scattering and a custom developed small particle sizing algorithm (SPSA) that are briefly described herein.

Shadowgraphy was used for developing two types of beam visualization, gathering particle velocities, and collecting the required data for the SPSA. The first beam visualization technique, the slicing method, aimed to evaluate thin axial slices of the beam at various distances across the beam. The particle beam was then reconstructed and visualized in three dimensions using custom processing algorithms. The second visualization technique (shadowgraphy with relaxed parameters) recorded particle locations in the x-y plane. The particle locations were converted to a histogram from which a beam width could be extracted. Particle velocities could be measured from any experiment where double frame acquisition was used with the appropriate timing parameters. In this technique a particle was identified in two successive frames separated by a discrete time interval. Using the measured distance between the particles and the times between exposures allowed for velocity calculations. Shadowgraphy was also used for the particle sizing algorithm which measured diffraction profiles from polystyrene latex (PSL) spheres. From these diffraction profiles two parameters were measured, image size and image slope. These parameters were found to uniquely identify a particle's size and location relative to the focal plane. Calibration curves were created from PSL spheres in a hope that they would be able to be used to size and positions polydisperse silver aerosol particles, but results suggested that the SPSA may be material sensitive.

The final characterization tool, Mie scattering, proved to be to most successful as it permitted rapid data acquisition with very accurate results. This method used a high speed camera to capture light scattered from a particle beam illuminated by a continuous wave laser. The intensity of scattered light was assumed proportional to particle density and could be used to determine particle beam widths. This technique was also found to be valuable for centering the particle beam in the depth of field of the high speed camera. Together these tools were used to accomplish the goals of this thesis.

2. LITERATURE REVIEW

Hoey et al. [2] defines, “Direct-write printing is an additive technology used to controllably deposit features onto samples in patterns defined by computer-aided design/computer-aided manufacturing software allowing rapid prototyping of various geometries without the use of lithography”. While similar, DW has been distinguished from conventional rapid prototyping by the following nuances[1]: the track width ranges from sub-microns to millimeters, printable materials include, metals, ceramics, polymers, biological materials, and electronically and optically functional materials, and finally, the substrate is an integral part of the final product.

Direct writing has been segregated into several subcategories depicted in Figure 1. Droplet, Energy Beam, Flow and Tip. Energy Beam, Flow, and Tip based deposition techniques mentioned previously are outside the scope of this research.

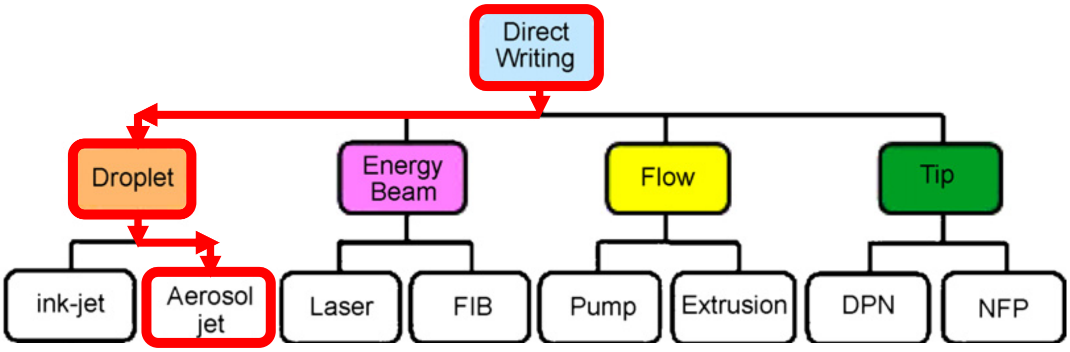

Figure 1. Direct writing methods categorized by Hon et al. [1].

2.1. Droplet Based Direct Write Methods

Droplet based deposition is further divided into two categories. The first being ink-jet printing. This technique finds applications in numerous fields ranging from solar cells [3] to 3-D manufacturing [4] to textiles [5] to organic transistors [6] to biosensors [7] and beyond. Continuous mode Inkjet printing operates on the following simplified design. Ink is delivered to the print head from which it is discharged using a piezoelectric transducer. Charging electrodes charge the particles which are then filtered and redirected by field plates which deliver ink to the substrate. Excess ink is captured and recirculated. Drop on Demand (DOD) ink-jet printing describes a process where an ink reservoir delivers ink as needed to a cavity where an actuator forces material through a small orifice which ejects streams of ink that break up into a collimated string of droplets. These droplets are on the order of hundreds of microns [1].

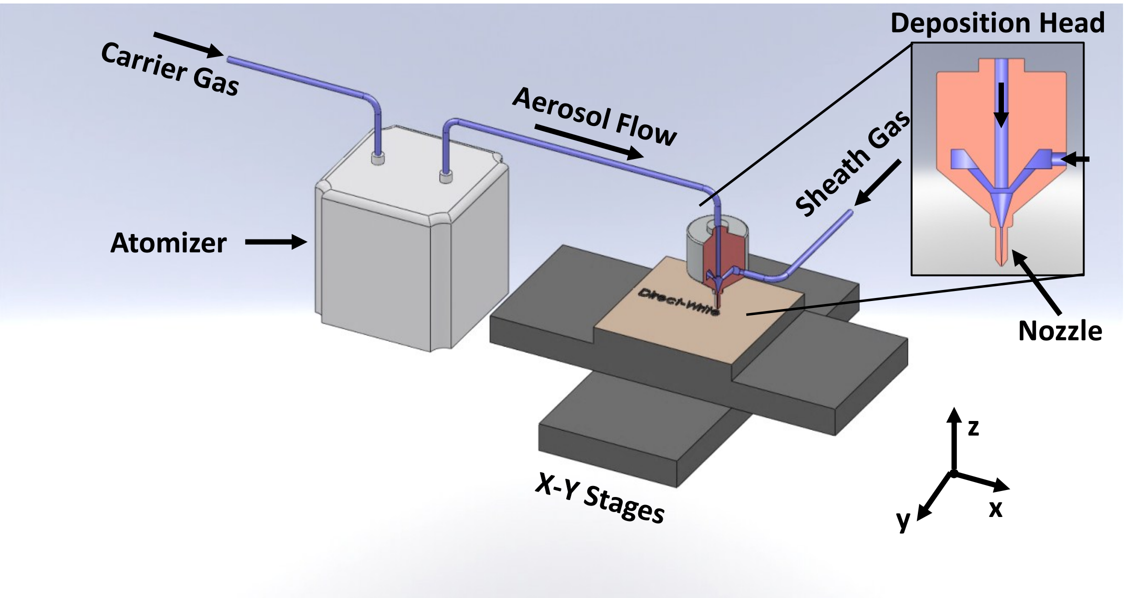

Figure 2. Diagram of Aerosol Jet DW process [2].

The second branch of droplet based printing is Aerosol Jet DW illustrated in Figure 2. This process is as follows. First, deposition material is entrained in carrier flow via an atomizer. Aerosol flow is then delivered to a deposition head where a second separate flow, sheath flow, is added coaxially causing pre-focusing of the aerosol particles. The aerosol is then focused further in a micro-nozzle and deposited on substrates which can be moved via x-y stages to create features.

2.2. Particle Visualization

Visualization of fluid particle interactions lies at the heart of many aerosol research studies. Subsequently, this high degree of interest has resulted in the application of existing visualization techniques such as shadowgraphy, scattering methods, and interferometry to experimental methods in DW research. These along with other relevant methods and their association with particle visualization are described herein.

Shadowgraphy techniques can be applied for visualization of particles as well as flow fields. For example, Lim et al. [8], used shadowgraphy to visualize 50 µm particles generated by a vibrating orifice aerosol generator. Velocity measurements were obtained in real-time though the used of the FlowMap Shadow Sizer module of the global sizing velocimeter (Dantec Dynamics Ltd., Bristol UK). Shadowgraphy will be discussed later in further detail.

Similar to shadowgraphy, Particle Image Velocimitry (PIV) is typically applied to visualization of flows. In this method, very small particles or “smoke” are entrained in the fluid flow. These particles need to be sufficiently small enough such that their mass does not affect their motion significantly. Instead the particles follow the streamlines of the flow and can be visualized using scattering techniques. A differentiation between shadowgraphy and PIV lies in the desired data extracted from the experiment. With shadowgraphy, typically the particle trajectories are of interest; in PIV the particles serve only as a means by which the flow field can be understood. PIV requires high particle concentration for accurate results and the laser beam perpendicular to the camera axis. Comparatively, shadowgraphy often requires low concentration, as clusters of particles make particle distinction difficult.

Scattering techniques are very commonly used for particle visualization due to their non-intrusive nature. Typical set ups involve a laser beam or sheet which illuminates a particle beam or dispersed aerosol axially or perpendicularly. Scatter type is categorized by the size of the illuminated particle. Rayleigh, Debye, and Mie scattering are three categories which typically pertain to aerosols. The categories are classified by $d<0.05*\lambda$, $0.05*\lambda<d<\lambda$, and , $0.05*\lambda<d$, respectively, where , d is the particle diameter and , λ is the wavelength of the incident light [9]. The use of scattering techniques has found application in many aerosol characterization experiments. Numerous apparatuses are commercially available from vendors such as LaVision, TSI, and Aerometrics

Koch et al. [10] used Mie scattering techniques to visualize plumes created from laser ablation of dielectrics in air. Also, shadowgraphy was used for visualizing the shockwave fronts created during these experiments. Material ejection resulted in aggregates of approximately 10 μm in diameter. Lee et al. [11] used scattering techniques to measure beam widths of PSL particles focused with aerodynamic lenses operating at atmospheric pressure. PSL particles, dried using a diffusion dryer, were subjected to an argon-ion laser sheet axially. Similarly, Fuerstanau [12] used thin plate orifice and PSL spheres in a vacuum chamber illuminated coaxially by a 1.0 mm 2 W Argon-Ion laser. Exposure times of 10 minutes allowed for visualization of the collimation of these particles. Additionally, the orientation of the laser allowed for visualization of the particles at the orifice exit as the scattering off the orifice was minimal due to the coaxial orientation of the setup.

TSI/Aerometric's Laser Doppler Interferometry (LDI), also referred to as Phase Doppler Interferometry (PDI), commercially available apparatus operates as follows. A single laser pulse of known frequency and power is split into two identical beams following two separate paths. The paths reunite at the area of interest where the particle is located and an interference pattern is formed from the scattered light. This pattern is viewed with a photo-detector. The recorded interference pattern offers insight into both particle size and velocity. As the particle is moving, the associated Doppler shift, which is proportional to the particles velocity, can be measured from the interference pattern. The particle size can be determined as it is inversely proportional to the spatial frequency of the interference pattern. TSI/Aerometric reports the ability to measure particle sizes ranging from 0.5-10,000 microns.

In 1996, Toker and Stricker [13] implemented holographic interferometry in a Mach-Zehnder apparatus for visualization of the radial distribution and changes in the refractive index of the vaporization of individual suspended droplets of chloroform acetone and diethyl ether. Relatively large droplets ranging from 2000 and 3000 μm in initial diameter were used.

Another commonly used method involves the measuring of particle depositions on a substrate by an aerosol beam. Various collection substrates are used such as glass slides [14] or vacuum oil coated substrates [15] depending on the aerosol composition. In 2007 Lee et al. [16] utilized both Rayleigh scattering effects and deposition measurements on to a greased aluminum substrate to evaluate aerodynamic lenses ability to produce an aerosol jet for single particle mass spectrometry. Deposition periods for Lee's experiment took upwards of 90 minutes. Similarly, Benner et al. [17] deposited particles onto silica wafers coated with vacuum grease. Deposition occurred for approximately 15-20 minutes after which a small circle, visible to the naked eye, was present. The diameter of this circle was measured with a microscope. This group also used a charge detector method.

Characterization of beams consisting of charged particles offers an alternative measurement technique. This method uses highly charged particles often generated with aerodynamic lenses flowing in a vacuum. Detectors register a change in current when exposed to charged particles. One technique [17] varies pressure differences across the lenses to change the focus of the particles. When the beam was diffuse few particles were collected by the charge detector pickup tube. Comparatively, when the beam was focused a large amount of charge particles were detected. This qualitative result, allowed for best focusing of the beam, after which deposition measurements were taken to measure beam widths. Liu et al. [18] investigated the process in the following manner. Aerodynamic lenses and small nozzles were used to focus dioctyl sebacate and NaCl particles in a vacuum. The focused particles were collected by a Faraday cup. Upstream from the cup, a “knife edge” was used to partially block the beam. As the knife edge crossed the particle beam, the current was measured in the cup. The current was correlated to beam widths where the results displayed a Gaussian beam with widths approaching the Brownian limit for dioctyl sebacate spherical particles.

Shadowgraphy is a common and well documented method used to size small particles which can be applied to experimental characterization of aerosol flows [19]. However, any means of optical sizing of small particles (<10 μm in diameter) is inherently limited due to diffraction which is experienced by all particles, but becomes increasingly relevant as particle diameter decreases.

As light interacts with small particles, portions of the shadow created are illuminated, creating ring patterns, by the diffracted light. The result is known as a Fresnel diffraction pattern. Fresnel diffraction patterns are a function of the wavelength of incident light, particle diameter, and distance from the particle. The transition from background intensity to shadow intensity is gradual making edge definition ambiguous. This is particularly inconvenient for the sizing of a small particle because the gradient edge transition area is a large percentage of the particle diameter.

Currently, small particles can be sized consistently using methods described by Kim and Kim [20] and used by the Davis shadowgraphy software for sizing particles with diameters greater than 8 μm. As particles move out of the depth of field, diffraction distorts the apparent size and edge transition area of the recorded shadowgram, making determination of the diameter of these particles difficult. Numerous efforts have been made with varying degrees of success to increase the envelope over which particles can be sized. In 1960, De Corso [21] used the width of the first diffraction ring as a characteristic for determining the particles' position relative to the object plane. Acquired images were manually inspected to estimate ring width which was correlated to optical axis distance (distance from object plane). This process was time consuming and largely subject to human error. More contemporary methods seek to remove the tedious and erroneous aspects of manual inspection though automation and image processing.

Particle identification is the first step in most automated sizing techniques and involves the recognition of potential particles and the determination of their centroid. Typically, an algorithm would then determine the degree of focus of candidate particles by measuring some parameter reflecting the sharpness of the shadows outer edge, or by examining the ‘halo’ created around the particle. This parameter is commonly referred to as the “in-focus criterion”. If the particle satisfies the in-focus criterion, it is then identified as an acceptable particle, and its diameter measured. Diameter measurement techniques can employ image preprocessing to remove background noise and correction factors based on image characteristics to determine the final predicted diameter.

Yule et al. [22] investigated the halo width as an in-focus criteria. By analyzing the shadowgram, they could calculate the halo width and a measured diameter of a particle. Results showed increases in halo width and underestimation of the diameter of the particle as particles moved from the depth of field.

Two other widely used parameters in particle sizing are gray level threshold and a means by which the gradient transition area can be quantified. Gray level threshold is used for both particle identification and as an in-focus criterion, while the transition area is generally only applicable as an in-focus criterion. Setting an appropriate gray level threshold between the background intensity and the shadow intensity allows the location of candidate particles. Once located, an Area of Interest (AOI) can be set enclosing the candidate particle and providing boundaries over which to analyze using the prescribed in-focus criterion/criteria.

Kim and Kim [20] established a method using a TV imaging system which selects optimal gray level thresholds and accounts for depth of field effects to size particles using a 105 mm focal length lens. Due to the deterioration of the image contrasts of small particles at high magnification from diffraction, they limited their magnification to 6X. Their experiments investigated liquid particles discharged from a fuel injector as small as 3.9 μm in diameter and as large as 71.9 μm. In order to account for diffraction effects they determined an acceptable way to calculate gray level threshold (G_{LT}) for individual particles based on the local background (G_{LB}) and object minimum background (G_{OM}) as well as a parameter known as Normalized Value of Contrast (*VC*). These parameters were used jointly as in-focus criteria. G_{LT} was calculated using the following equation:

$$G_{LT} = G_{LB} - 0.5 * (G_{LB} - G_{OM}), \tag{1}$$

The normalized value of contrast is then determined by

$$VC = \frac{G_{LB} - G_{OM}}{G_{LB}}, \tag{2}$$

This method had mixed results ranging from very successful measurements; in one case sizing a 3.9 μm particle with less than 1% error to inaccurately sized 100 μm particles with error reportedly as large as 45%. Koh et al. [23] proposed using the Gradient Indicator (*GI*) as a second in-focus criterion in addition to G_{LT}. By quantifying the gray level gradient around the edge of the particle image using the Sobel Operator, the variations of GI and the distance from the focal plane could be found for a given particle size. Based on the results a critical index value for a particular size was determined. Particles with a GI larger than their associated critical index were considered focused. In addition, Schaub et al. [24] showed that simplified theoretical intensity gradients matched experimental gradients for 50 μm water droplets illuminated by incoherent light. These results confirmed that theoretical gradients could be used as an in-focus criterion for the sizing of particles in dynamic sprays.

As discussed, improvements in data acquisition, image processing techniques and novel methods which define and measure characteristics directly related to particle diameter have helped to overcome the barriers that have limited optical sizing. This paper presents an optical sizing method, known as the SPSA, for particles ranging from 1.0 μm to 10.0 μm in diameter through the automated processing of Fresnel diffraction patterns. It increases the sizing envelope and has the ability to calculate particle position along the optical axis.

3. BEAM CHARACTERIZATION TECHNIQUES

3.1. Theoretical Modeling

The second goal of this research, validation of a model which requires an understanding of the forces which focus the aerosol beam, was accomplished though a collaborative relationship with Artur Lutfurakhmanov, who was responsible for the modeling of aerosol flows in micro-capillaries. The modeling techniques are briefly described here but are fully available [25]. Gas velocity and density inside and outside of the capillary were determined using a commercially available product, ANSYS CFX, where the continuity, momentum and energy equations were solved. As the capillary geometry was axially symmetric, a five degree sector was considered to minimize computational cost. After gas flow was successfully modeled using ANSYS CFX, simulation results were exported in Matlab for further calculation of particles' velocities and trajectories. Custom Matlab code was used to solve Newton's second law:

$$\frac{4}{3}\pi a^3 \rho_p \frac{d\mathbf{v}_p}{dt} = \sum \mathbf{F}, \tag{3}$$

where, ρ_p is the particle density, a is the particle radius, $\mathbf{v}_p$ is the aerosol particle's velocity vector and, the sum of all forces acting on the particle is $\sum \mathbf{F}$. The two primary focusing forces due to fluid particle interaction were Stokes force:

$$\mathbf{F}_{St} = 6\pi a \mu \left(\mathbf{v} - \mathbf{v}_p\right), \tag{4}$$

and Saffman force:

$$\mathbf{F}_{Sa} = 6.46 a^2 \left(u - u_p\right) \sqrt{\rho \mu \left|\frac{\partial u}{\partial y}\right|} Sign\left(\frac{\partial u}{\partial y}\right) \mathbf{e}_y \tag{5}$$

where μ is the gas viscosity, $\mathbf{v}$ is the velocity vector of the carrier gas, u and u_p are the axial components of the gas and particle velocity, respectively, ρ is the gas density, and $\mathbf{e}_y$ is the unit vector along the y axis. Also, it was necessary to apply the following correction to Saffman force (C_{Sa}):

$$C_{Sa} = \begin{cases} 0.2343\left[1 - e^{-0.1\mathrm{Re}_p}\right]\sqrt{\dfrac{\mathrm{Re}_f}{\mathrm{Re}_p}} + e^{-0.1\mathrm{Re}_p}, & 0.1 \le \mathrm{Re}_p \le 40 \\ 0.0371\sqrt{\mathrm{Re}_f} & , 40 < \mathrm{Re}_p \le 100 \end{cases} , \tag{6}$$

resulting in the corrected Saffman force:

$$\mathbf{F}_{Sa} = 6.46a^2\left(u - u_p\right)\sqrt{\rho\mu\left|\frac{\partial u}{\partial y}\right|}\,Sign\left(\frac{\partial u}{\partial y}\right)C_{Sa}\mathbf{e}_y . \tag{7}$$

Here, Re_f is the shear Reynolds number, Re_p is the Reynolds number of the particle.

Additional forces were neglected due to an order of magnitude analysis which suggested that in addition to Stokes, Saffman force was the most likely to affect particle trajectories. Additional assumptions include neglecting surface roughness, gravity, condensation, evaporation, and collision with walls and other particles. Also, particles size and shape were assumed to be monodisperse and spherical.

Using this modeling technique, particles could be introduced at any position radially and axially inside the geometry. Trajectories for numerous, gasses, flow rates, particle sizes, densities, etc. were calculated as needed for comparative purposes with the experimental results.

3.2. Aerosolization

Aerosolization is a critical and sensitive part of both printing processes and beam characterization. For this research it was desirable to have the ability to aerosolize and analyze particle beams consisting of both liquid inks and dry powders. Liquid inks offer comparison to actual printing methods with similar parameters. While characterization of beams consisting of dry powder offers parallels to micro-coldspray applications, dry powders offer another desirable quality, monodispersity. During shadowgraphy experiments, diffraction causes out of focus particles to appear larger than their actual size. Because the Stokes force is a function of particle diameter, mistakenly oversized particles would be incorrectly predicted to experience more focusing. It was necessary to examine beam widths from particles with known sizes and densities. Using monodisperse silica ensured that focusing forces were only a function of the particle-gas velocity differential and allowed for direct comparison to the theoretical model. Compared to the aerosolized liquid ink droplets produced by ultrasonic aerosolization, which ranged in size from 1.0 to 10.0 µm, dry powders are available in tight distributions. Silica microspheres, acquired from Cospheric Inc., mass median diameter (d50) was 3.8 µm ± 10% CV (by volume) with a density of 1.80 g/cc.

3.2.1. Ultrasonic Aerosolization

The ultrasonic atomizer was used for atomization of liquid silver ink supplied by PV-Nanocell (Migdal Ha'Emek, Israel). The ink was diluted with deionized water to a concentration of 2:1 by volume and loaded into a glass vile with a cap-mounted inlet and outlet. The system incorporated a cooling system, type k thermocouple, and adjustable vial holder. The cooling system consisted of approximately 18 inches of 1/4” copper tubing through which house water flowed at 0.24 gallons per minute. This maintained a constant temperature of 22-24°C as measured by the thermocouple. The adjustable vial holder provide 6 degrees of freedom allowing the vial to be positioned anywhere in the bath. Best aerosolization was seen when the vial was directly above the piezoelectric, with a range of an eighth to a quarter of an inch of the vial submerged in the water bath. Also, adjusting the tilt of the vial from 5 to 20 degrees off vertical improved aerosolization.

3.2.2. Low Flow Dry Powder Aerosolization

The low mass flow powder aerosolizer was used for aerosolization of silica spheres, Figure 3, and tested with silver powder but could be used with copper, tin, and aluminum.

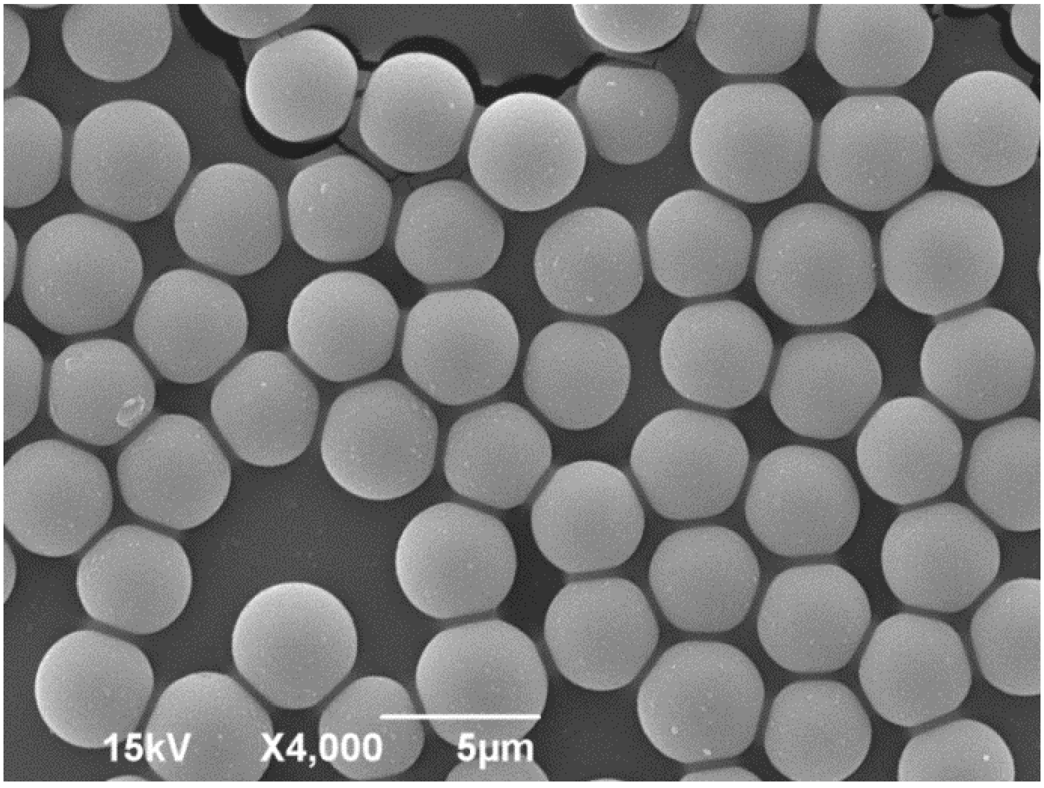

Figure 3. Monodisperse silica spheres measured to be 3.8 μm in diameter.

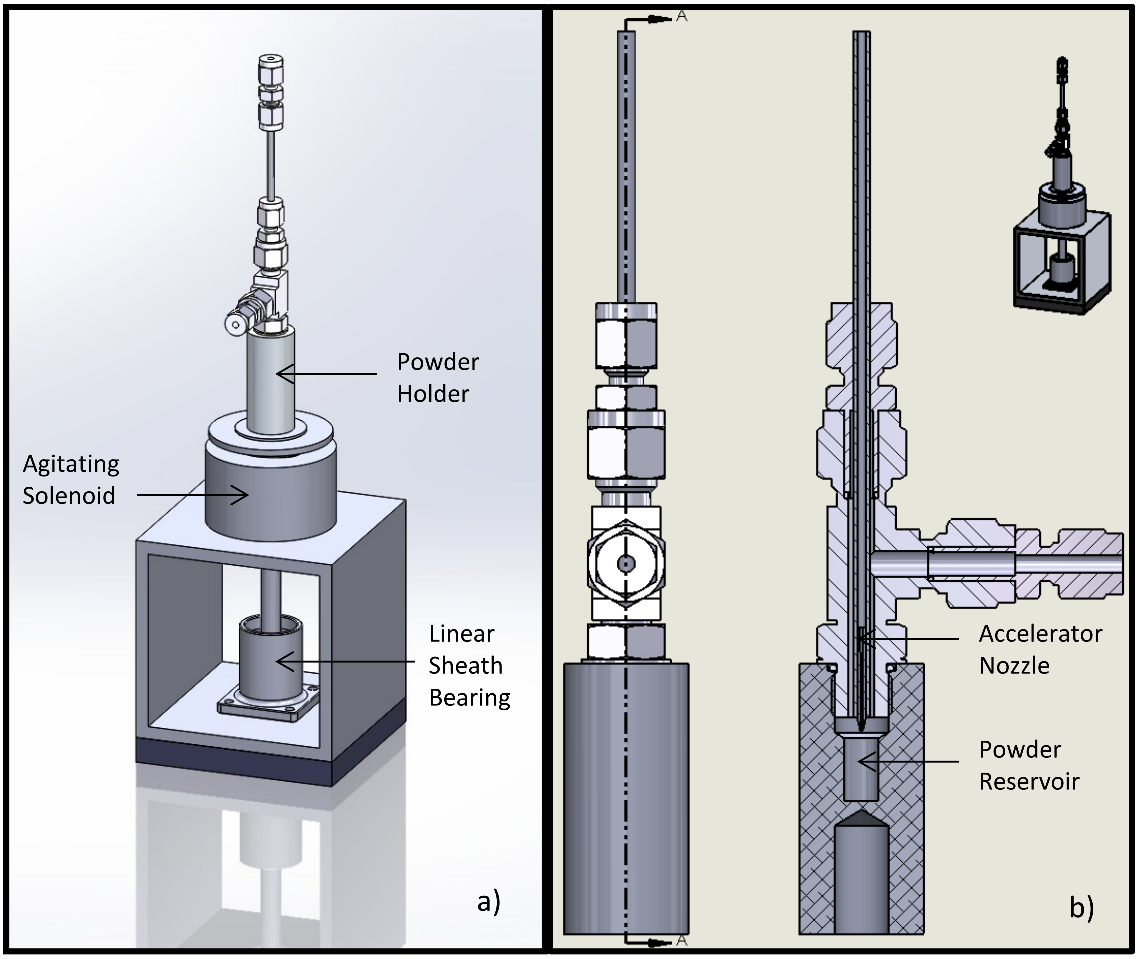

Figure 4. Solid Works drawing of a) low flow dry powder atomizer and b) coaxial powder holder design.

This custom built atomizer, Figure 4, consists of an inlet accelerator nozzle, powder reservoir, agitation system, and a coaxial counter flow outlet design. The agitation system creates a fluidized bed inside the reservoir and is adjustable in both frequency and amplitude via two potentiometers. The accelerator nozzle is a Gaiser, 75 µm exit diameter, which accelerates the inlet carrier flow to high speeds. Swagelok fittings are used to connect sections of the aerosolizer to eliminate leaks. House nitrogen is delivered to two MKS mass flow controllers which regulate the flow within a tenth of a standard cubic cm. per minute. 1/8” polyurethane tubing delivers the nitrogen gas from the flow controllers into 1/8” inner diameter 1/4” outer diameter stainless steel tube. This stainless steel tubing has a smaller outer diameter than the inner diameter of the bore-through Swagelok “T” fitting allowing it to run through the straight section into the powder holder. The Gaiser nozzle is friction fit into the end of this pipe such that the nozzle is oriented in the direction of the flow. This nozzle accelerates the flow to high speeds and blows a jet of nitrogen into the powder reservoir and aerosolizes the powder. The aerosolized powder flows around the outside of the stainless steel tube and out the ‘T’ of the Swagelok fitting. The aerosolized powder is delivered to the deposition head via 1/8” polyurethane tubing. This counter flow coaxial design results in a compact closed loop which requires small powder loadings of approximately 150 mg of silica. The powder holder, stabilizing rod and heat sink allow for extended operation with minimized wear.

3.3. Nozzle Geometries

Various nozzle geometries were used during the experiments and are described in this section. The linear converging nozzle shown in Figure 5 was provided by Aurora Micro Machine. This nozzle was created through the use of rotating wire Electronic Discharge Machining (EDM). The material was tungsten carbide. The outer diameter of this nozzle was 1/16” with a length of ¾”. The inlet and outlet diameters were measured to be 820 μm and 240 μm, respectively. This nozzle offered a well characterized and simple geometry which facilitates comparison with the theoretical model. This nozzle is depicted in Figure 6.

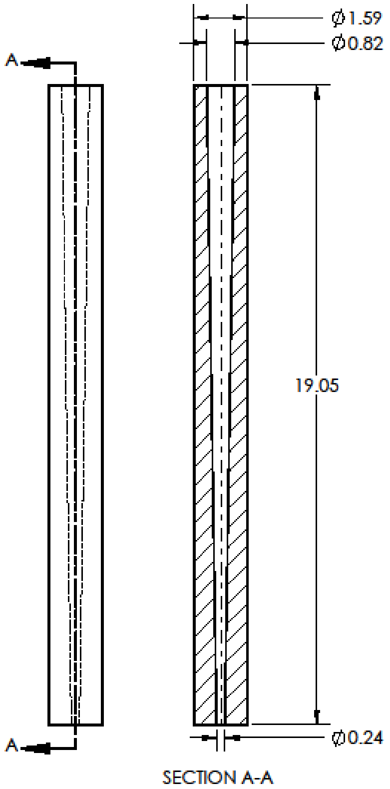

Figure 5. Tungsten carbide linear converging nozzle (dimensions are in mm).

Figure 6. Image of tungsten carbide nozzle next to dime for size comparison.

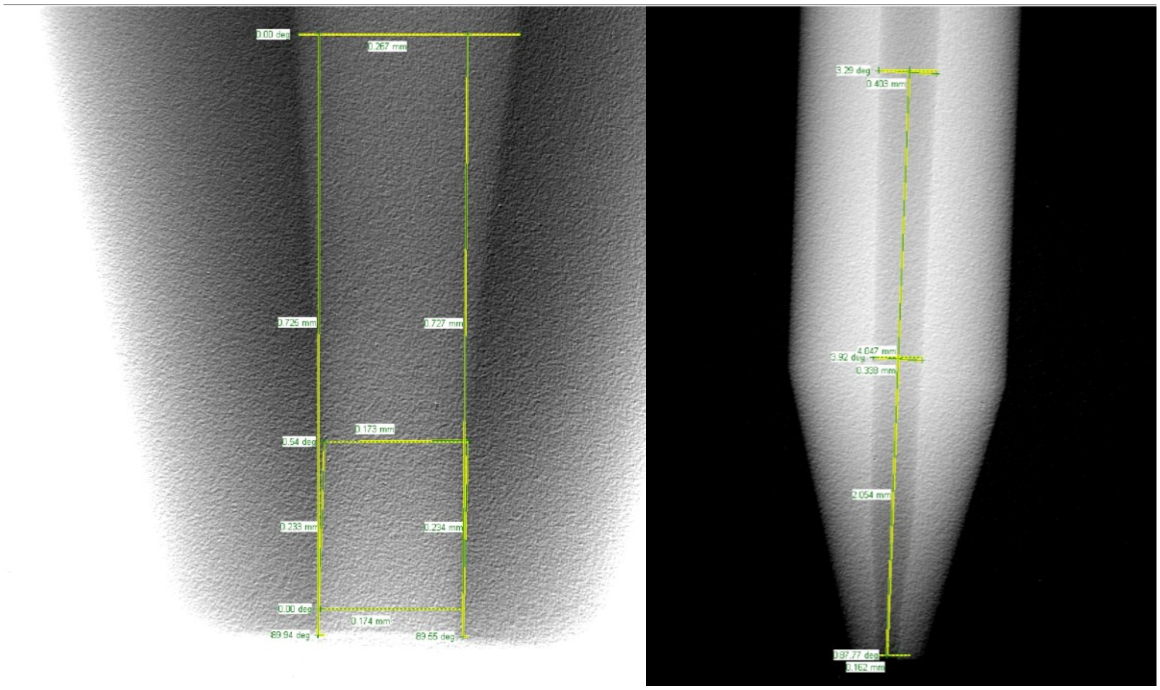

Figure 7. X-ray image of a) ceramic nozzle with 175 μm inner exit diameter and b) zoomed view of same nozzle showing straight section at nozzle exit, reprinted from Akhatov et al. [26], Copyright 2008, with permission from Springer.

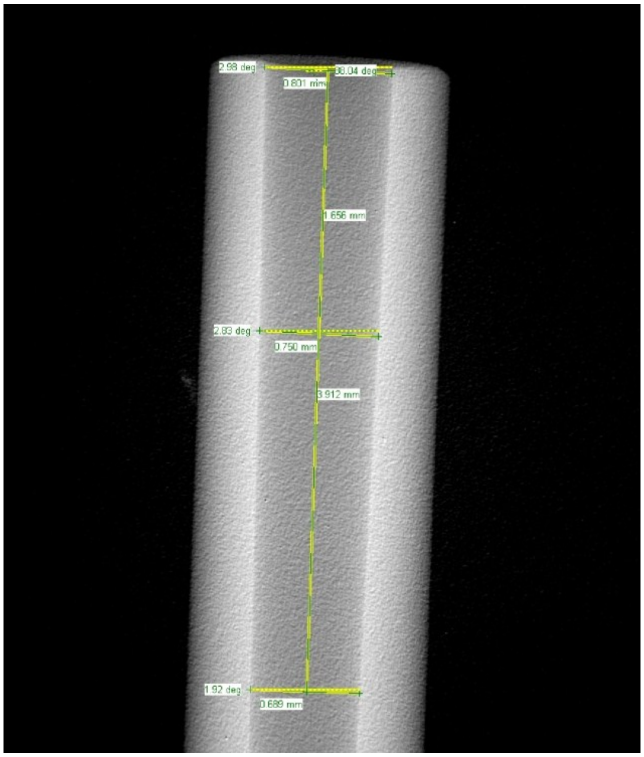

Figure 8. X-ray image of ceramic nozzle with 800 μm inner inlet diameter, reprinted from Akhatov et al. [26], Copyright 2008, with permission from Springer.

The Gaiser ceramic nozzles were supplied by CoorsTek, Inc. These nozzles have more complicated inner geometries but were available at the beginning of the research and were available in different exit diameters and lengths. These nozzles' inner geometries consist of a two-stage converging, single-stage straight section and a short diverging section. This geometry was measured using X-ray imaging and is illustrated in Figure 7, Figure 8, and Figure 9.

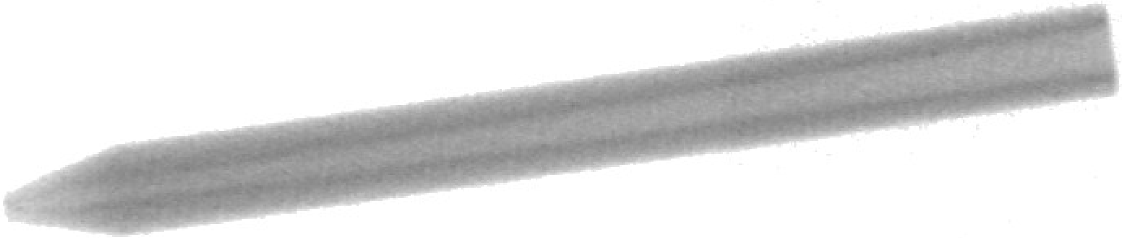

Figure 9. Inner geometry profile from 175 µm inner exit diameter nozzle, reprinted from Akhatov et al. [26], Copyright 2008, with permission from Springer.

During the slicing experiments, a short converging section was cut from a 125 exit diameter ceramic nozzle and used. This "cut nozzle" had a length, inner inlet and inner exit diameter of 17.14 mm, 832 µm and 355 µm, respectively. It provided a linearly converging diameter which could more easily be modeled.

While acquiring the inlet conditions a short nozzle was required. To achieve this, a ceramic nozzle was cut to a length of 6.86 mm. The inner inlet diameter was measured to be 810 µm, consistent with the 175 µm ceramic nozzle, and the exit diameter was measured to be 620 µm. Further experiments called for coupling straight sections to the nozzles in order to pronounce the effect of Saffman force. These straight sections were made of tungsten carbide and created again with wire EDM. The lengths, inner and outer diameters of the straight sections are summarized in Table 1 and shown in Figure 52.

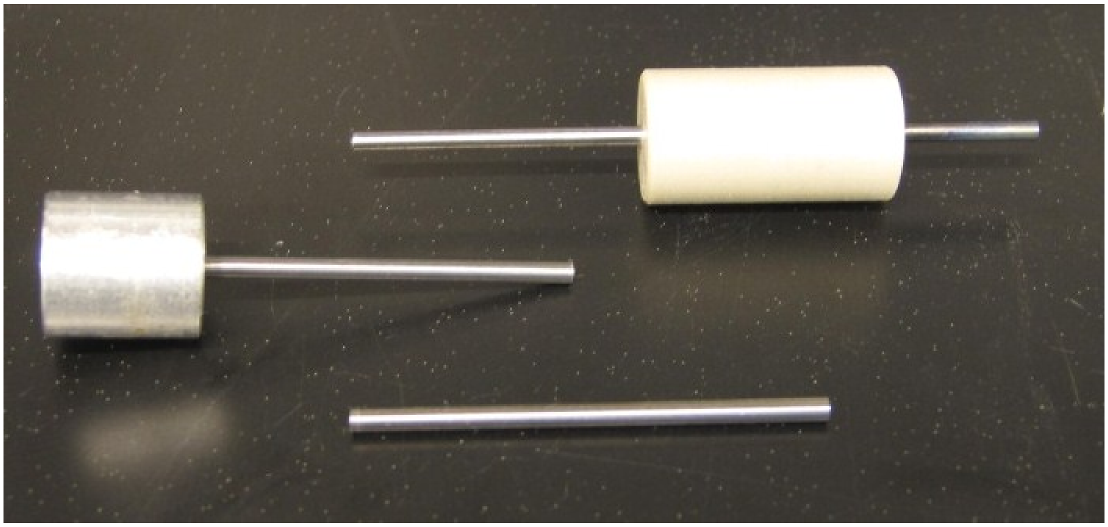

Figure 10. 30 mm straight capillary alone, in aluminum and peek couplers.

Table 1. Straight section geometries of tungsten carbide tubes.

Outer Diameter	*Lengths (mm)*	*Inner Diameter (µm)*
1.580 mm	11.84	200
	17	
	30	
1.5875 mm	11	264
	17	
	30	

These capillaries were connected to the converging nozzles using coupling sleeves. These sleeves were made from both peek and aluminum. Peek offered tighter seals because they were drilled such that the tungsten carbide would not fit without heating the coupler. Once the peek is expanded the tungsten carbide pieces could be inserted, allowed to cool and shrink creating a tight fit. A challenge with the peek tubes was making the nozzle align concentrically with the straight section. The aluminum could be machined more accurately and offered a higher degree of concentricity when aligning the nozzle and straight section. Misaligned nozzles result in abrupt edges at the nozzle/capillary interface which disturb flow and interfere with focusing.

3.4. Shadowgraphy

3.4.1. Experimental Shadowgraphy Apparatus

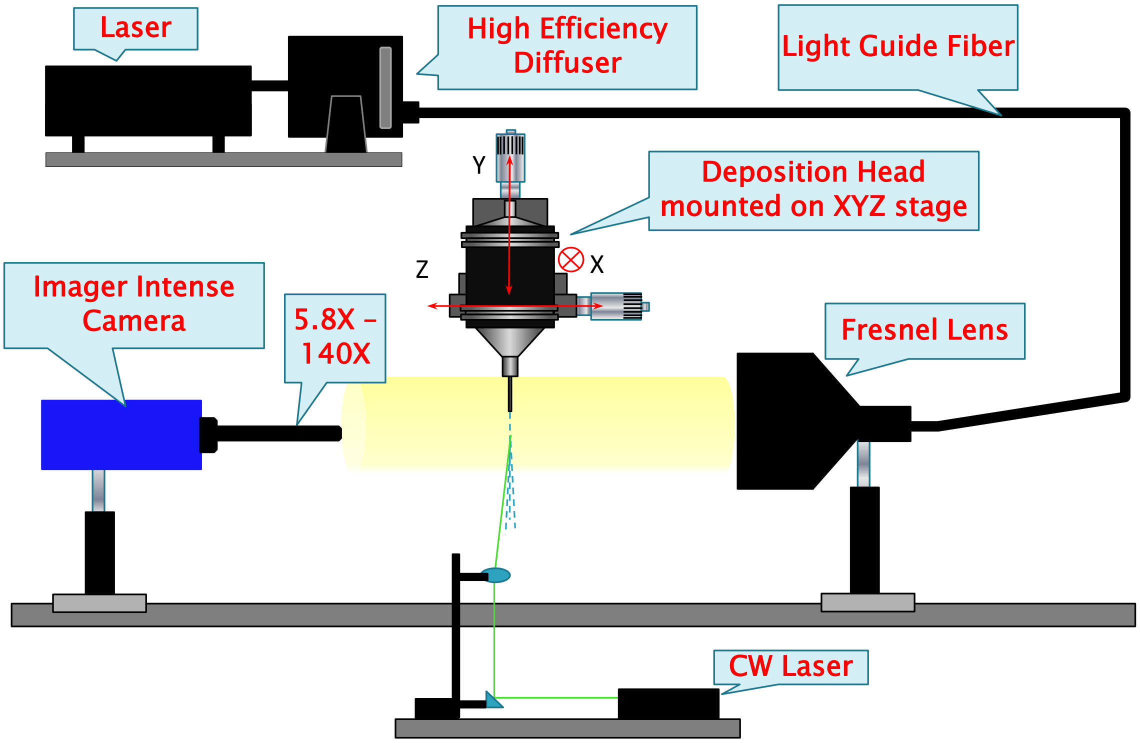

Figure 11. Experimental apparatus for shadowgraphy experiments with CW laser for centering.

The experimental apparatus, Figure 11, operated in the following manner: Pulsed incoherent light was produced by pumping fluorescent dye in the high efficiency diffuser with a Quantel USA Inc. dual cavity Nd:YAG 532 nm Q-switched laser. A light guide fiber delivered the incoherent light through a collimating Fresnel lens. The light was then attenuated by neutral density filters. Filter optical densities were selected such that an intensity of approximately 2500-3500 counts was achieved while the laser power was maximized. This created consistency between laser pulses without over exposing the Imager Intense Camera. The camera optical system included a 12X variable zoom lens and a 10X objective lens that has a depth-of-field of less than 12 µm. A linear translation stage was used as a mount for the deposition head and was controlled by a Newport ESP 100 Motion Controller. The entire system was located on an active isolation self-leveling frame with an optical honeycomb breadboard. Nitrogen gas flow is regulated with two MKS mass flow controllers capable of stabilizing flow from 0 sccm to 125 sccm each with accuracies of approximately ± 0.1 sccm. The flow is fed into the atomizer and deposition head via 1/8” polyurethane tubing. When first generating flow it was important to first turn the flow controller on to a low value (less than 10 sccm) then increase gradually. Also, it was important to initiate flow prior to starting atomization. These steps helped to prevent clogging. The deposition head was acquired in 2004 by Optimec. It is their first iteration and features a two flow design. A carrier gas with entrained particles is attached at the top of the deposition head. Sheath gas is introduced annularly before the particles reach the nozzle. This helps pre-focus the particles and create a boundary between the particles and the nozzle wall.

Davis Software version 7.2.2 was used for preprocessing which included particle identification and location in the x-y plane and velocity measurements. The processing parameters for the majority of shadowgraphy experiments performed fell under two categories: tight and relaxed. Tight processing parameters strived to select only particles in the highest focus and exclude all particles that were out of the cameras depth of field. Relaxed processing parameters were applicable when data was desired from across the entire particle beam as compared to only a thin slice of the beam. Relaxed parameters were able to identify particles at least 100 μm from the depth of field. Table 2 shows these parameters. Information regarding these parameters can be found in the LaVision Sizing Maser Shadow product manual [27].

Table 2. Davis settings for tight and relaxed parameters.

Parameter	*Tight*	*Relaxed*
Particle Recognition		
Global Threshold	35%	20%
Low Level Threshold	30%	45%
High Level Threshold	70%	55%
AOI Expansion	200%	800%
Maximal Low Level Area	300% of high level area	500% of high level area
Minimal Centricity	60%	30%

After processing the shadowgraphy data, for each particle, the particle number, image number, predicted diameter, x-coordinate, y-coordinate, axial velocity and radial velocity, are combined into a particle list which is processed by various Matlab algorithms.

It was frequently beneficial to locate the center of the particle beam prior to and during experiments. This was accomplished in a number of ways. The simplest but least accurate method was to use shadowgraphy and manually move the edge of the nozzle into focus. This method assumes that the particle beam's center is the same as the nozzles center and that the nozzle is a perfect cylinder. While this assumption is clearly false, this technique does offer a convenient and fast way to get close to the center. While no experiments were used to confirm the accuracy of this centering method, operators generally found that the nozzle edge was within at least 20-30 µm of the particle beam center. The second centering method utilizes Mie scattering from illumination with a continuous wave (CW) laser. This class IIIb diode pumped solid state laser operated at 532 nm producing green light rated at max output of 200 mW. Laser mirrors were used to irradiate the particle beam perpendicular to the optic axis of the camera. A time exposure of 20-40 ms per frame was used to record the light scattered from the particles producing a streak corresponding to the particles path. Assuming the scattered intensity is proportional to the particle density the beam can be centered in the cameras frame. Also, the edges of the beam should have a high gradient, and the peak of the camera should be noisy as highly focused individual particles register small spikes in intensity. With high quality particle beams, centering with the CW laser was accurate within 5-10 μm. This was much less accurate when the particle beam became dispersed as the particle distribution was volatile. The third and final method used to find the center of the particle beam is described in the Slicing method which is outlined in section 3.4.2.

3.4.2. Slicing Method via Shadowgraphy

The slicing method was used to calculate the axial velocity of liquid silver ink through the cut nozzle described in section 3.3. This was then compared to theoretical results. The pure ink was PV-Nanocell silver nanoparticle ink (Migdal Ha'Emek, Israel). This was diluted in an atomization vial with water at a ratio of 1:2 to create the liquid silver ink which is also used for printing. The vial was then mounted in the ultrasonic atomizer. This atomization technique was sensitive to the vial's location with respect to the piezoelectric. This helps promote standing wave on the surface which increases atomization. In circumstances where atomization was lacking, adjusting the vials location or height in the water frequently resolved the issue. Figure 12 shows the ultrasonic atomizer with the ink vile in a typical orientation.

Acquiring data using this method involved 4 steps. First, a centering experiment was performed. Second, the data from the centering experiment was processed in Matlab using the center finding algorithm. Third, returning to the experiment the beam was moved to the newly calculated center where a large amount of data was recorded (approximately 10,000 images). Fourth, from the data taken at the center, the axial velocity was plotted as function of radial position. This process was necessary both to ensure that the data was taken at the center of the particle beam, and to determine how accurately the center of the particle beam could be found using the continuous wave laser alone.

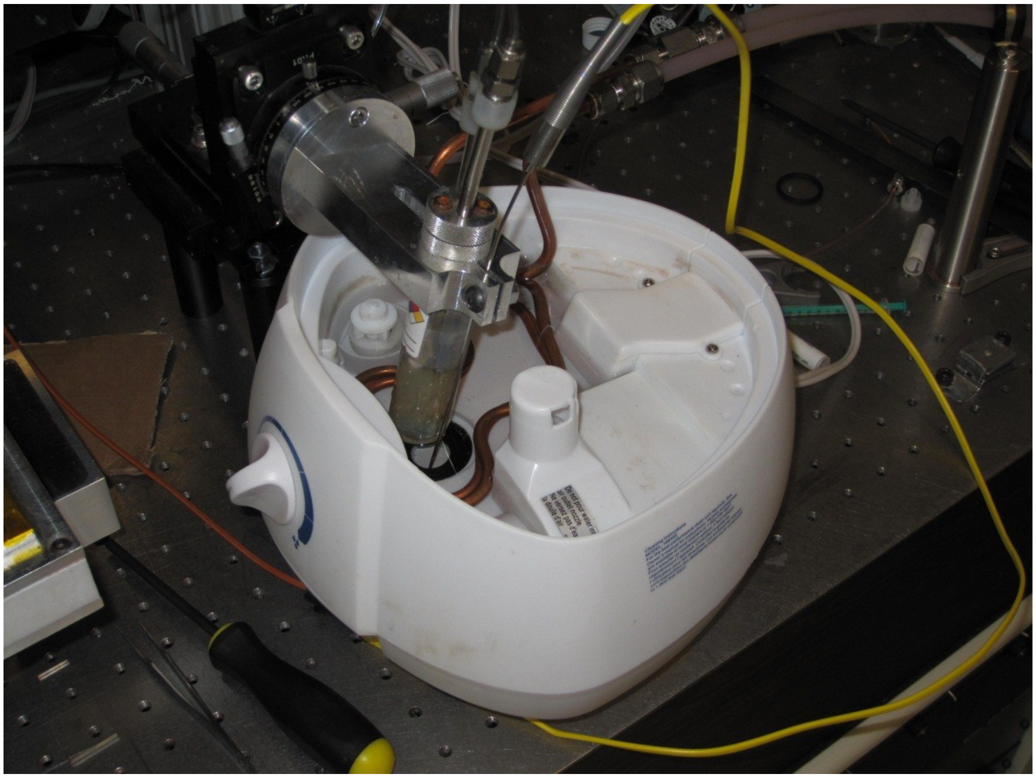

Figure 12. Ultrasonic atomizer with ink vial tilted slightly to improve atomization.

Because particle velocities are dictated by gas velocities, in order to measure the peak particle velocity data must be collected in the center of the particle beam. At this time, the accuracy of centering with the CW laser was unknown so an experiment was designed to find the center of the particle beam. In the centering experiment, shadowgraphy was used first to focus on the edge of the nozzle which corresponded to an approximate center. Second, the nozzle was raised until it was just out of the field of view. Next, atomization and gas flow was initiated. Visual inspection via shadowgraphy was used to confirm that particles were flowing out of the nozzle. If particles were present, the continuous wave laser was used for more precise centering of the particle beam. Once the center of the beam was found with the CW laser, as described in 3.5, the system was switched back to shadowgraphy for image acquisition. Images were acquired in axial “slices” across the entire beam in random 15 µm steps along the z-axis using the Newport ESP Motion Controller. This random stepping was performed because little was known about how the processing parameters would quantitatively affect the range over which particles were recognized and it was important to acquire data from the entire beam width. Because the outer edges of the beam had a lower particle density than the center the number of images taken in each slice varied based on how far it was from the approximate center.

Table 3. Slicing experiment outline.

Experimental Parameters				Experiment:	5232011
Zstep	15	microns			
Zmax	75	microns		Run Time	
Zmin	-75	microns		Stepping	1:15
Run Time	4:39	minutes		Processing	0:60
Sheath Gas	40	sccm		Delimiting	0:30
Carrier Gas	20	sccm		Matlab	0:25
Pressure	0.09	psig		Center Images	0:55
Ink Temp	23.3	Deg. C		Processing	0:35
Filter	546	nm		Total	4:45
Slice	Random #	# of Images	Accq	Frame 1	Frame 2
75	6	2000	Y	2500	2900
60	1	2000	Y	2900	3000
45	8	1500	Y	2100	2300
30	9	1000	Y	2100	2100
15	3	1000	Y	2500	2700
0	2	1000	Y	2500	2700
-15	11	1000	Y	2000	2200
-30	7	1000	Y	2200	2400
-45	5	1000	Y	2400	2500
-60	4	1500	Y	2400	2700
-75	10	2000	Y	2000	2200
Reference	na	100	Y	2000	2200
Counts after centering				3000	3000

Additionally, to ensure that the laser pulses were consistent throughout the experiment, the background intensity was recorded at each slice. The resulting image sets were processed using the DaVis processing software with tight processing parameters (described in Table 2) ensuring that the identified particles are all in a high degree of focus. This eliminates all the particles which are not in the associated slice. A typical centering experiment with relevant parameters is outlined below in Table 3.

After acquiring the centering data and processing with DaVis, the resulting particle lists were further processed in the custom Matlab algorithms, Data_Filter, and Z_Offset. During this processing the flow is not stopped, only the atomizer is turned off. Data_Filter.m is used to remove all velocity vectors and particles that are incorrectly identified by DaVis. This is done by incorporating acceptable radial and axial velocity ranges and a particle size cap. Restricting the radial velocity component ensures that velocity vectors are in the same direction of the flow. Errors arise when two similarly sized particles are in the same frame but are located to the left or right of each other. Restricting the axial velocity ensures that particles are not accidently assigned too large or too small velocities which can occur if two similar sized particles happen to be directly above and below each other. Finally limiting particle size ensures that clusters or false particles are removed from the data. Figure 13 illustrates these situations. After, filtering the particles, the data is loaded into Z_Offset.m which identifies the center of the particle beam based on highest particle velocity. All particles are assigned a z-coordinate consistent with the slice in which they were acquired. The particles are then plotted together in a 3-D graph, of x-position (µm), z-position (µm) and velocity (m/s).

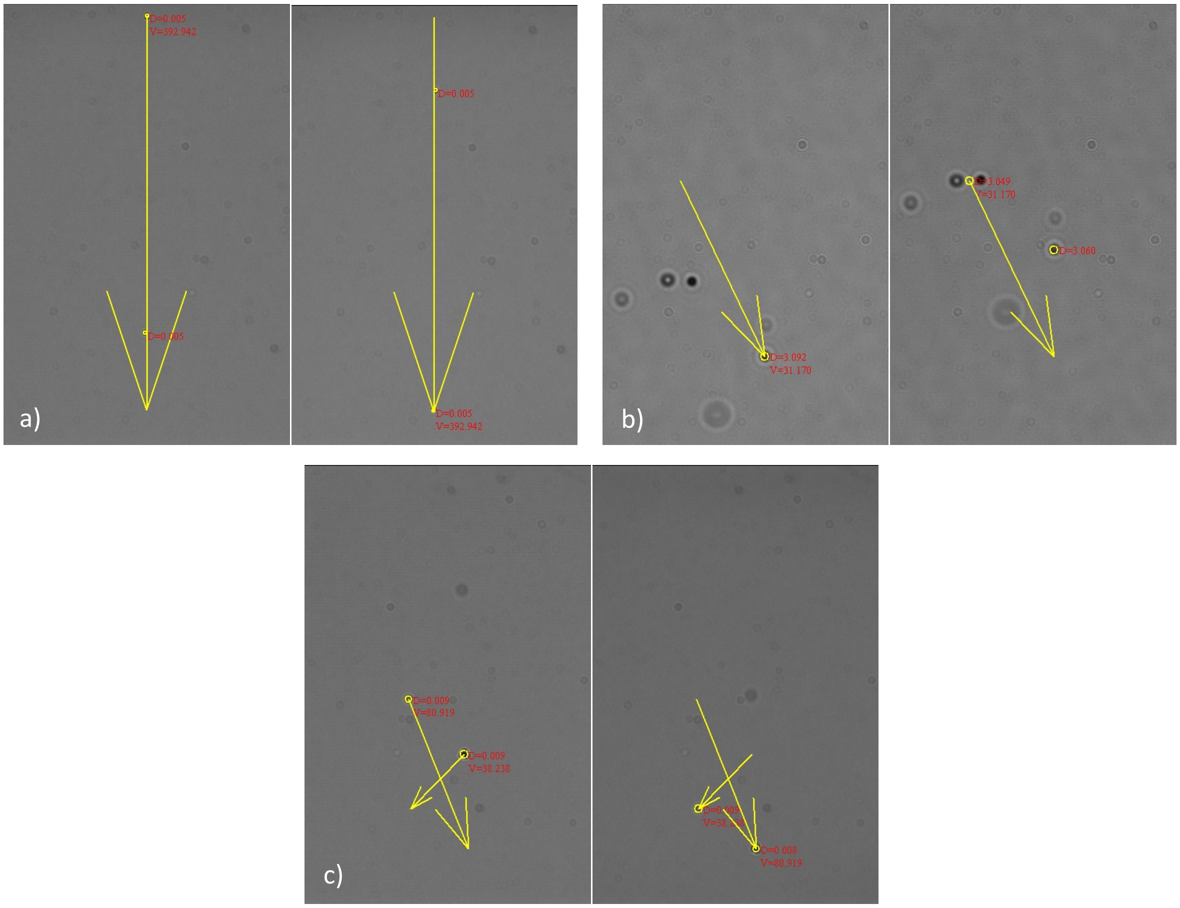

Figure 13. Examples of incorrectly recognized velocity vectors: a) velocity vector is elongated due to overlapping b) particle has been located where there is no particle and c) particles have been miss identified in second frame.

Parabolic curves are fit to all the points in a given slice, and the maximum of this parabola identified as shown in Figure 14. Figure 15 and Figure 16 show the particle velocity distribution and number density, respectively. The particle distribution expectedly show an increase in particles near the center of the beam but also shows a relatively sharp edge in the x direction where particles abruptly stop. The parabolic fits are meshed with a function in Matlab returning a surface plot illustrating the velocity with a color gradient. This image shows clearly the velocity distribution of the particle beam.

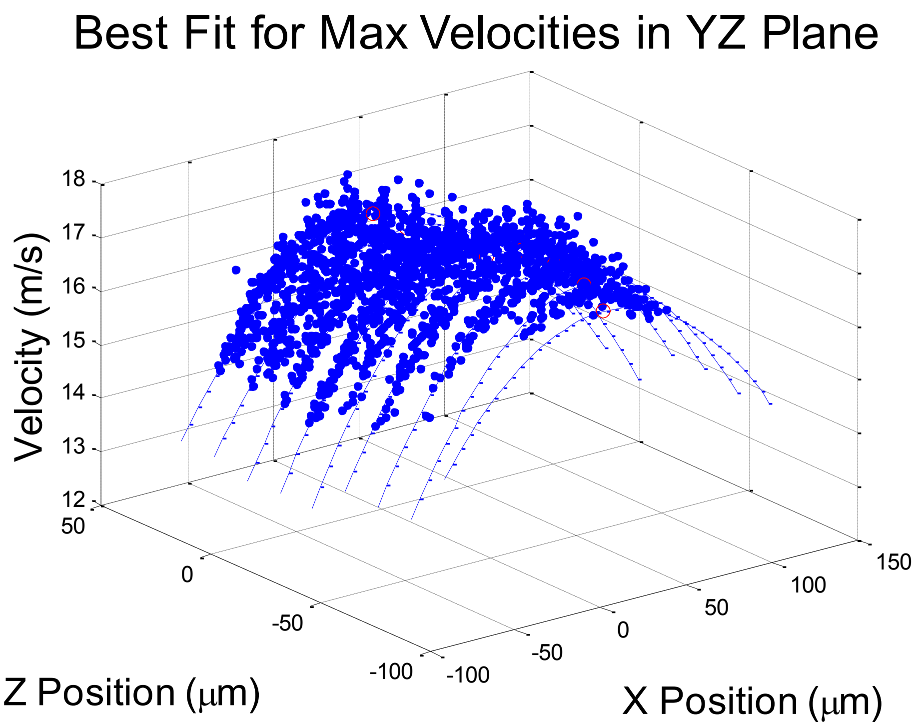

Figure 14. Parabolic fits to slices from cross sectional beam profile data gathered from slicing experiment of silver ink flowing through cut nozzle at 60 sccm.

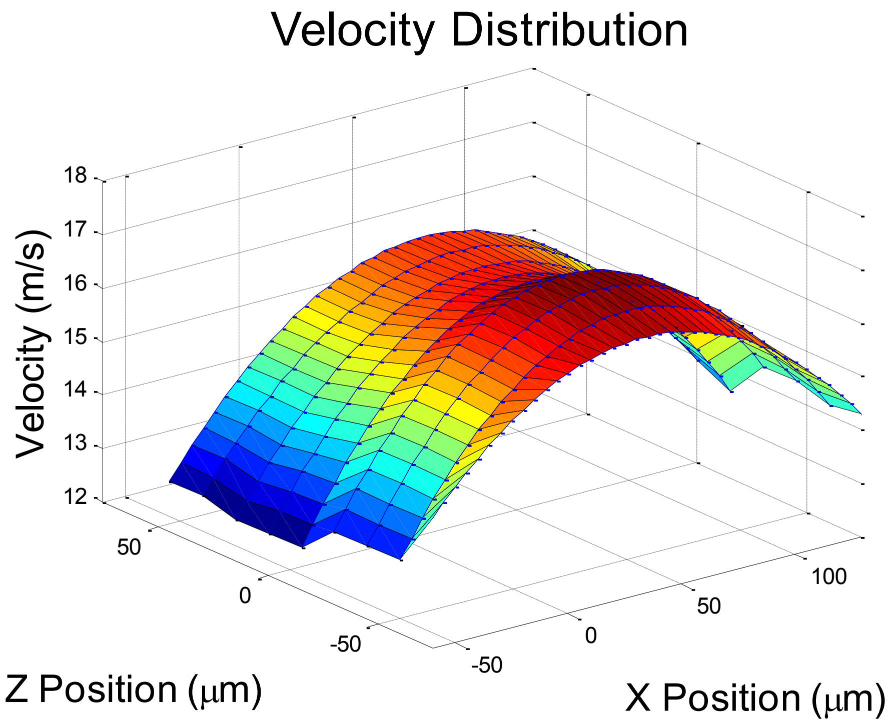

Figure 15. Velocity distribution created by Z_Offset.m from data gathered via the slicing method from silver ink flowing through the cut nozzle at 60 sccm.

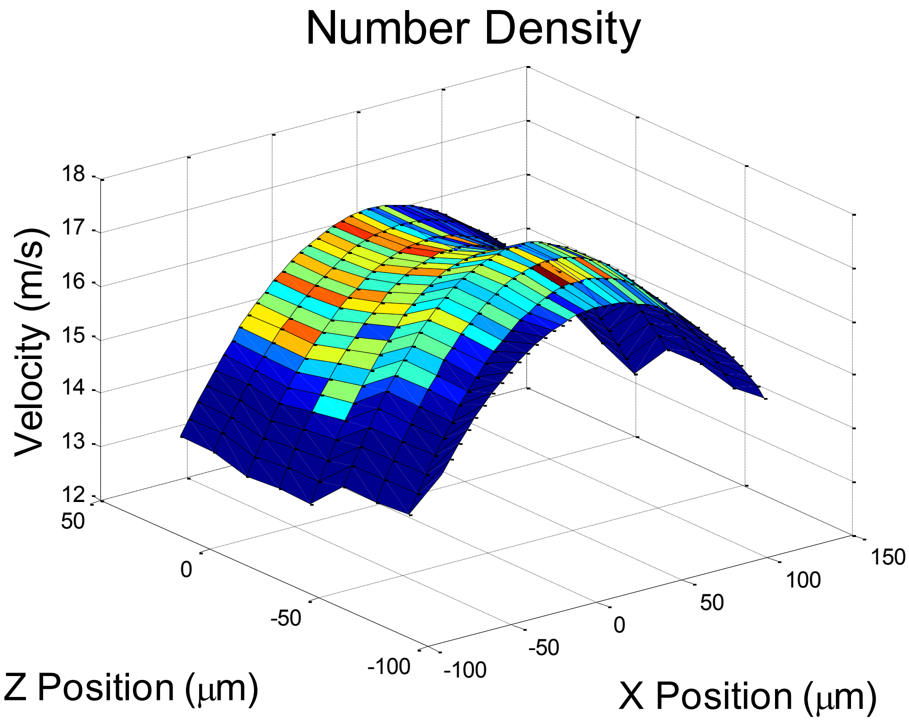

Figure 16. Number density created by Z_Offset.m from data gathered via the slicing method from silver ink flowing through the cut nozzle at 60 sccm.

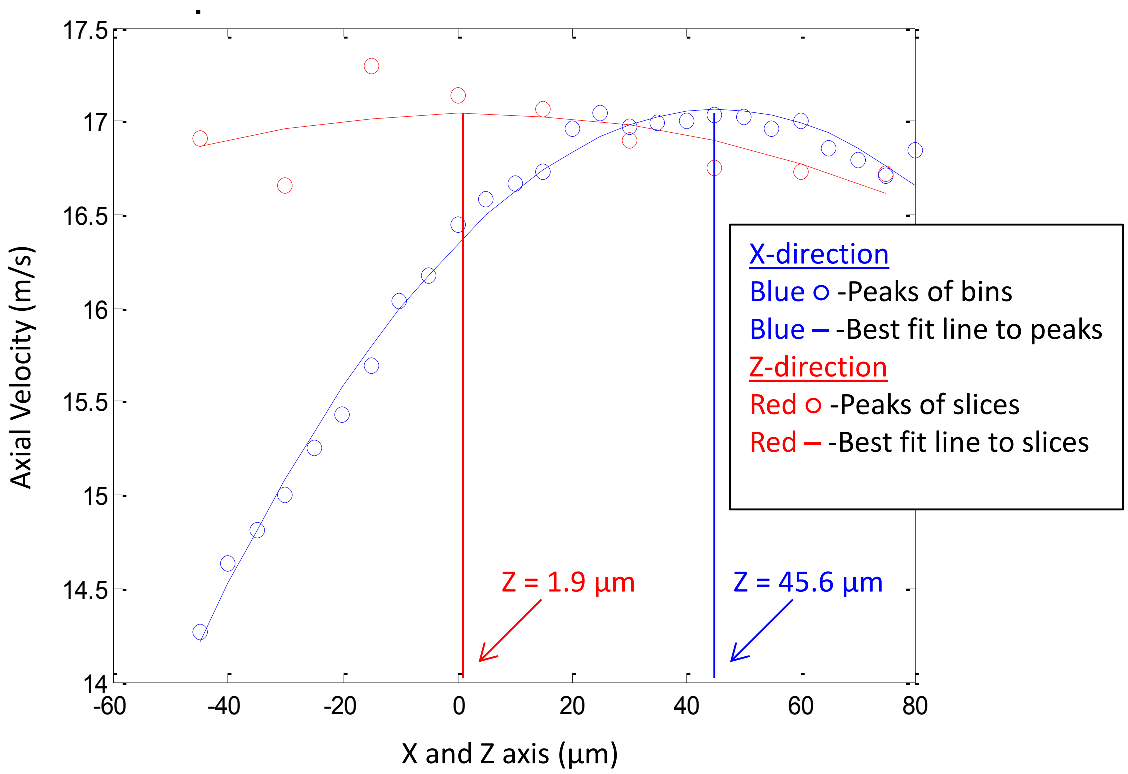

Figure 17. Curvature of particle beam calculated by Z_Offset.m and X_Offset.m.

Then, another parabolic line is fit to the peak velocities for each slice. This shows us the curvature in the z-direction. The vertex of the parabola which represents the curvature in the z-direction is the center of the beam in the z-direciton . The offset between the center via focusing with the cw laser and the calcualted center is measured and represents the necessary correction to move the center of the beam into the focal plane of the camera.

The deposition head is translated accordingly, and a large data set of approximately 10,000 shadow images is acquried at the center of the particle beam. After the shadowgraphy data at the center of the beam has been acquired, it is processed using X_Offset and CenterSliceProcessing.m. These algorithms adjust for offset in the x-direction and calculate the radial position. The particles are separated by size range, small (1-2 µm), medium (3-4 µm), and large (5-6 µm). The axial velocity is plotted as function of radial position as seen in Figure 18, and trends fit to this data. The result offers comparison of focusing between various particle sizes.

Expectedly, Figure 18 shows that the smaller particles have higher velocites than the larger particles which tend to lag the gas more due to inertial effects. This data was then compared to theoretical results for two particle ranges, 1-2 µm and 2-3 µm. The results are shown in Figure 19 and Figure 20. These results showed that the particle velocities were slightly below the theoretical velocites but only by about 4% and 3% at peak velocites for 1-2 µm and 2-3 µm particles, respectively. As radial velocity increased the difference in particle velocity decreases

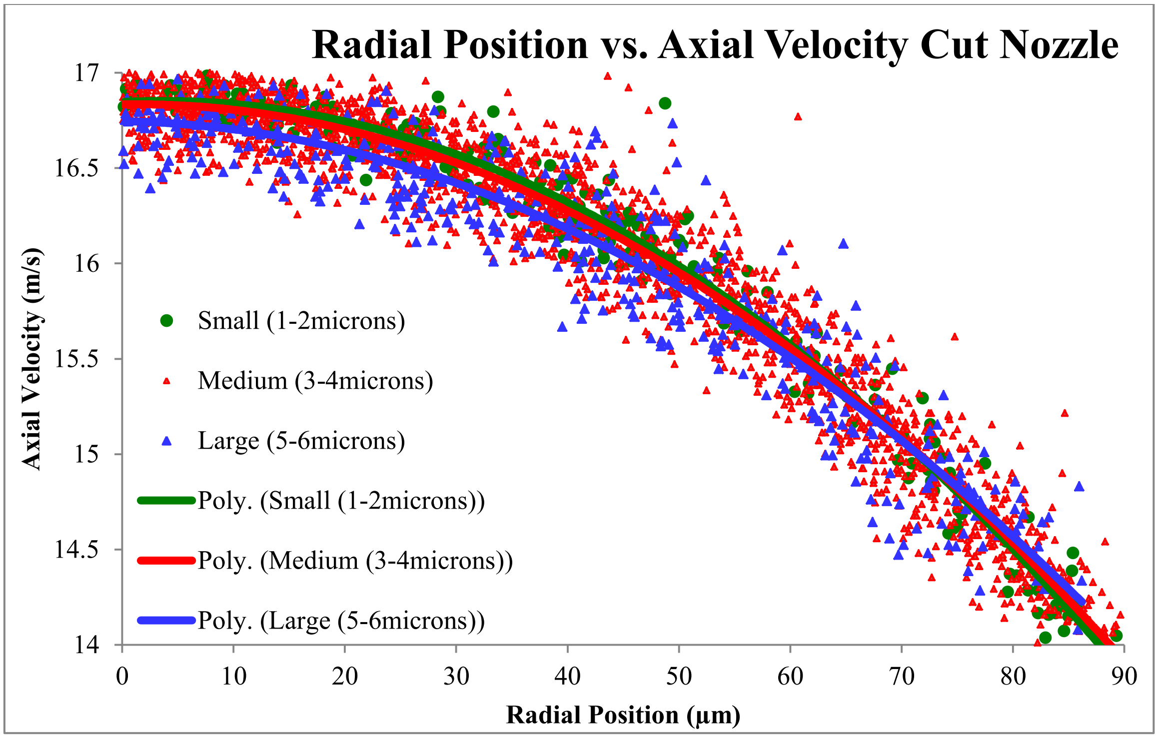

Figure 18. Graph of Radial Position vs. Axial Velocity from cut nozzle experiment.

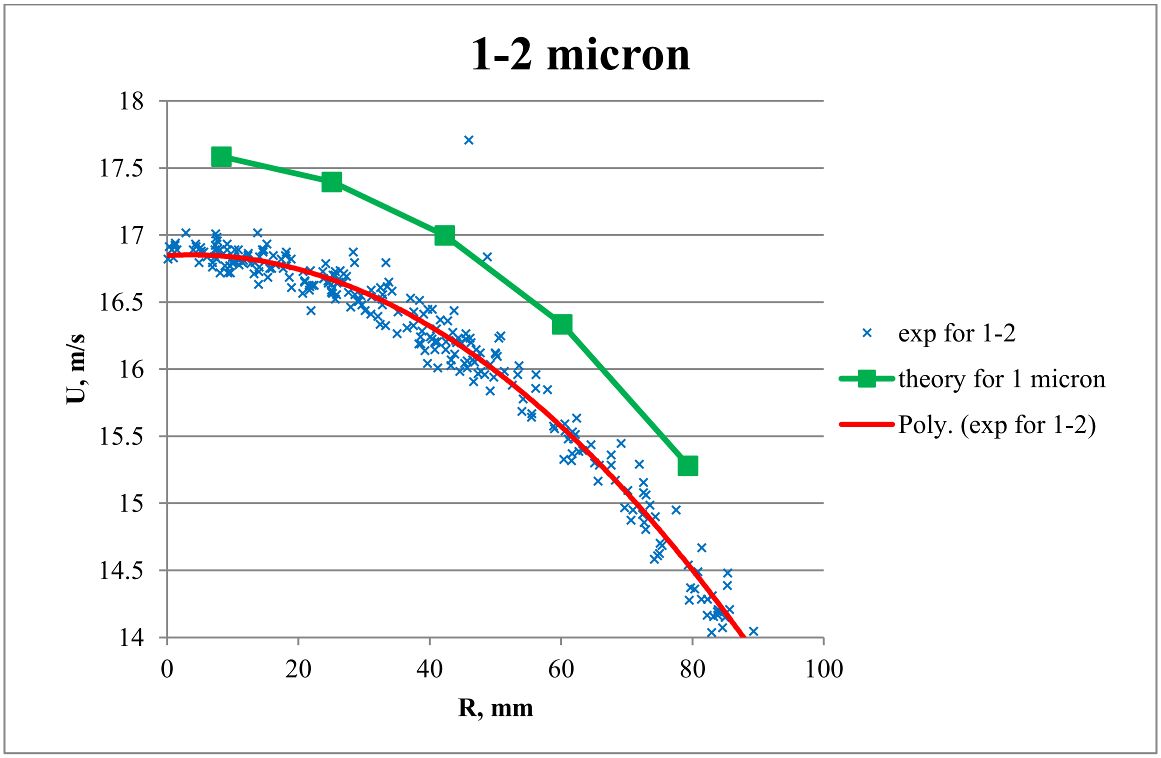

Figure 19. Comparison of Experimental and Theoretical Results for 1-2 micron particles in cut nozzle.

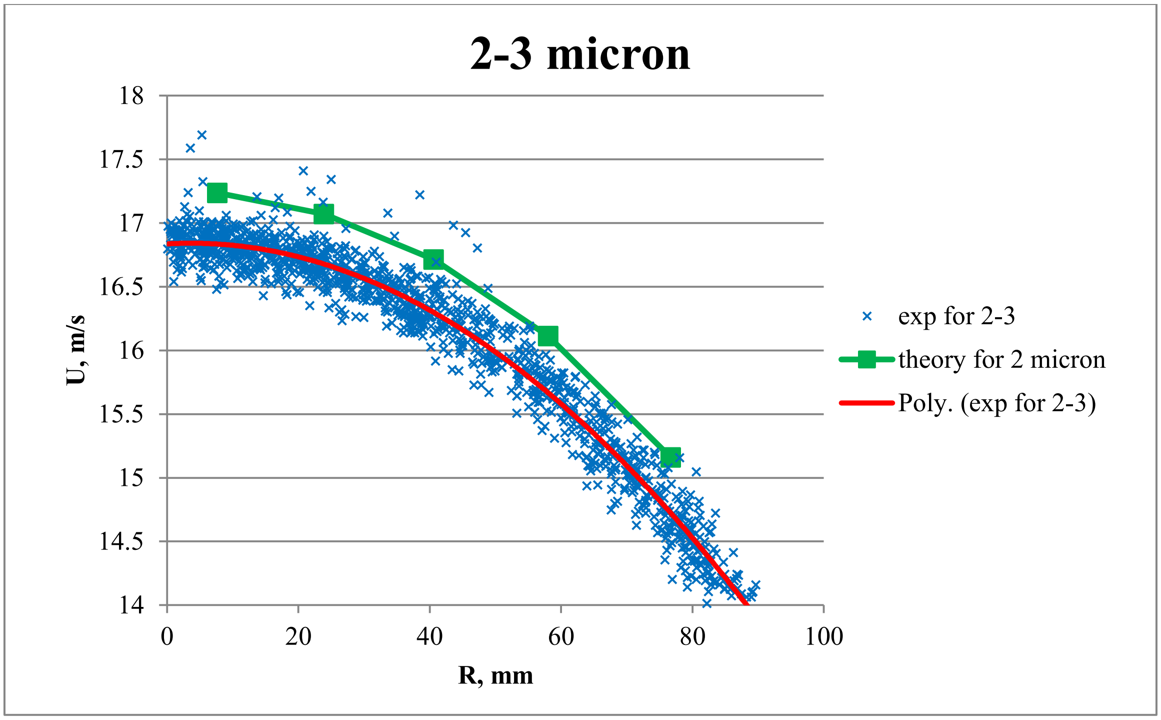

Figure 20. Comparison of Experimental and Theoretical Results for 2-3 micron particles in cut nozzle.

The slicing method effectively located the particle beam center and compared experimental velocities with theoretical velocities. Algorithms were developed and used to filter particle velocities and size, and calculate x-coordinate and z-coordinate offsets. Particle velocities were seen to be within 3-4% of theoretical predictions for small and medium particle sizes. Additionally, due to the lack of curvature in the z-axis of Figure 17, it appears as though the range over which the tight processing parameters recognize particles is much larger than the 15µm step. This gave creedence to the idea that it may be possible to view particles across the entire beam width simultaneously, eliminating the need for the stepping process. The centering results also show that centering with the continuous wave laser is an accurate method.

3.4.3. Relaxed Processing Parameters

The slicing method used tight processing parameters in an attempt to recognize only particles within a thin slice of the beam. However, the experimental results suggested that relaxing the parameters would allow viewing of the entire beam. Not only will this technique allow for gathering velocity measurements, but the acquired data can be used to generate an additional route for beam characterization, beam width. In this characterization technique the beam width is measured by creating a particle distribution histogram from which the beam width can be measured. Several other improvements were incorporated during this new technique as well. The silver ink was replaced with the monodisperse silica spheres (3.8µm in diameter) atomized by the low flow dry powder atomizer facilitating a more accurate comparison with the model. Also, data sets were acquired at different distances from the nozzle exit. This permits comparison of the entire beam instead of only at the nozzle exit and gives insight into how the particles are focusing far from the nozzle exit. Finally the ceramic tube was replaced with a tungsten carbide linear converging nozzle. This nozzle was selected for modeling ease and because the inner geometry was well characterized. After applying these changes, experimental beam width and velocity results were compared to theoretical results.

3.4.4. Beam Widths via Shadowgraphy with Relaxed Processing

Beam width experiments were performed using the shadowgraphy apparatus. Approximately 0.1 grams of silica powder was loaded into the powder holder. The powder was stored at 120 C° for a 12 hour period prior to the experiment to dry the powder. As silica is hydrophilic it was important to use dried powder during the experiments to prevent clumping of the particles which increased clogging during the experiments. After the atomizer was loaded, the carrier flow was initiated. The mass flow controllers were turned on prior to connecting the carrier hose to the atomizer because a large flow burst was forced through the hose when the mass flow controller was turned on. This caused a large amount of powder to be forced though the deposition head and out of the nozzle which frequently clogged the deposition head or slightly altered the nozzle geometry with buildups at the nozzle entrance and/or exit. Carrier flow was raised slowly in 10 sccm increments until the desired carrier flow was achieved, then the sheath flow as raised in the same manner. Pressure was allowed to stabilize before any experimental data was acquired. The pressure readings were recorded at various flow rates and used as a monitoring system for both systems leaks (pressure drops) and clogging (pressure spikes). In the event that the starting pressure was not consistent with previous pressures for the same experiment, the experiment was aborted and the entire system was cleaned. Cleaning the system involved removing the nozzle and cleaning it by forcing compressed air in the reverse flow direction. The nozzle was then inspected with a microscope where any remaining clogs would be visible. If clogs were unable to be cleared using compressed air, a 5-10 minute sonication in isopropanol was usually sufficient to remove the silica buildup. After sonication compressed air was used to clear and dry the nozzle after which it was again inspected. In the rare cases where neither the compressed air nor sonication was successful, small wires (0.004-0.008 inch diameter) were threaded through the nozzle, and the nozzle rotated to disturb buildups. If a nozzle was still clogged after the previous cleaning methods, the nozzle would be sonicated in a highly basic solution of potassium hydroxide.

The deposition head clearing only required the isopropanol sonication and the compressed air methods. An example of a partially clogged nozzle is shown in Figure 21.

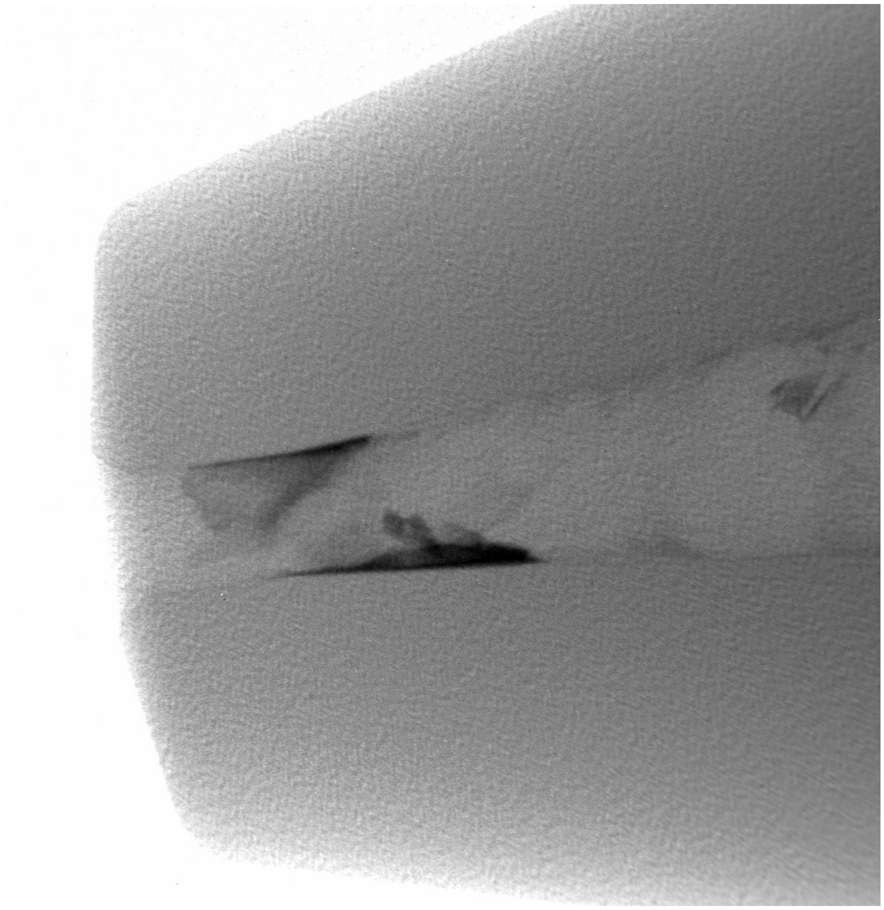

Figure 21. X-ray image of partially clogged ceramic nozzle, reprinted from Akhatov et al. [26], Copyright 2008, with permission from Springer.

When first using the experimental system, operating pressures were lower than expected. The system was checked thoroughly for leaks which were caused by loose fittings and were removed by simply tightening the fittings further or replacing the thread sealing tape. Leaks were considered removed when the volume flow rate set by the mass flow controllers matched the volume flow rate through the nozzle. The flow through the nozzle was measured by measuring the water displaced by nitrogen with an inverted graduated cylinder. A large 1 liter beaker was half filled with water. Then, a 100 mL graduated cylinder was filled entirely and inverted into the larger beaker such that no bubbles remained inside the smaller cylinder. A Swagelok fitting was used to attach a polyurethane tube to the nozzle and the exit of the tube bubbling into the 1 liter beaker. The inverted graduated cylinder was positioned over the exit of the hose and the bubbles captured for a known time period. After the initial leaks were removed, leak tests were performed regularly to monitor the system for additional leaks. No additional leaks were discovered.

During the cleaning of the deposition head, it was noted that a large amount of silica was collecting inside a vertical stainless steel ¼ inch shaft connecting the carrier line to the inner cone where the sheath gas meets the carrier gas. The design was modified in an effort to decrease the particle build up inside this section of the deposition head and to move the particles closer to the center axis of the inner cone. This was accomplished by extending the dirty carrier line through the shaft and actually to the exit of the inner cone. The polyurethane tubing was slightly larger than that inner cone making a quality friction fit possible. The tube was heated and pulled until necking occurred allowing for the smaller diameter to be pulled into the cone. The tubing was then pulled until the necked region was past the cone exit and the excess was trimmed leaving a snug connection. While a small buildup still occurred inside the tubing, compared to the larger steel shaft, the buildup was greatly reduced and the centerline of the flow was confined to a smaller area.

With the deposition head and nozzle free of buildup and the pressures matching previous experiments, experimental data was collected. The CW laser was used for centering, laser power was adjusted such that background intensity registered 2500 counts, and the *dt* setting was set to 1 μs. Images, generally ranging from 1000 to 5000 frames, were taken at various distances usually in 1 mm steps beginning at the nozzle exit. The corresponding particle lists were exported and processed using the Matlab algorithm ShadowBWCalc.m. This program first plots the position of all the particles for a given distance from the nozzle. Figure 22 shows the locations of the silica particles flowing at 180 sccm at the exit of the inlet condition nozzle. Next, the particles are binned based on their x-locations and a histogram is created. The histogram in Figure 23 is for 180 sccm flow through the inlet condition nozzle. After creating the histogram, a Gaussian curve is fit to the data as shown in Figure 24. The beam width of this curve can then be measured at different heights such as full width half max, 1/e and 1/e^2. The resulting beam widths were then complied creating a beam width profile. These profiles were compared to the modeling results as shown in Figure 25

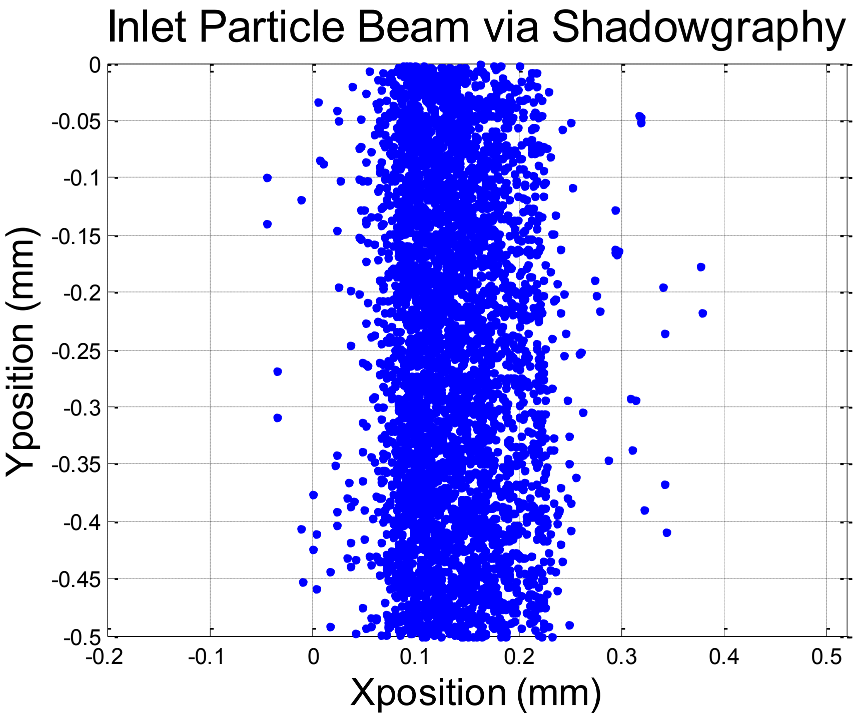

Figure 22. Particle location of silica particle flowing at 180 sccm through inlet condition nozzle.

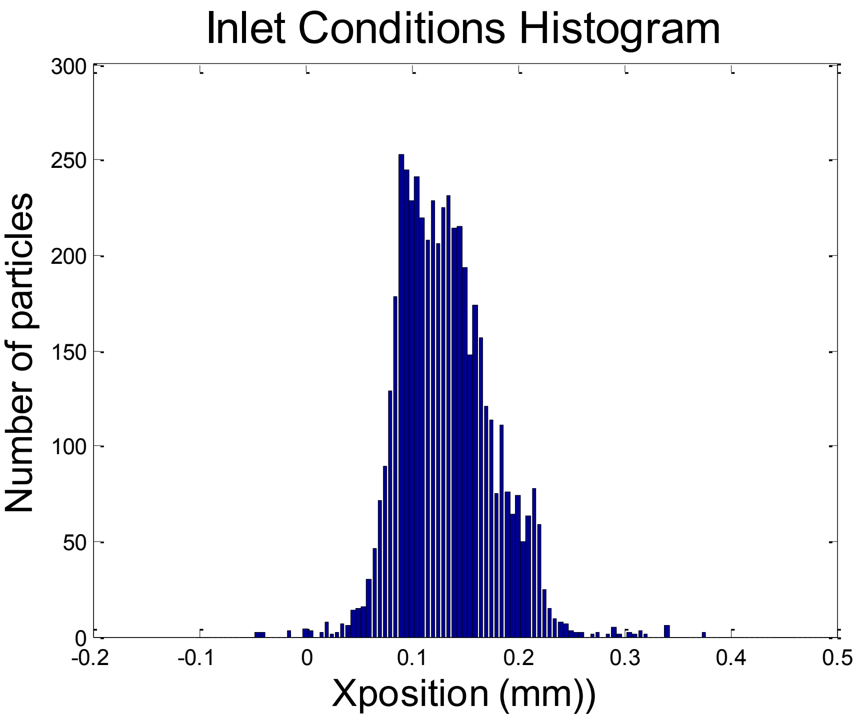

Figure 23. Histogram for inlet conditions at 180 sccm for silica particles through linear converging nozzle.

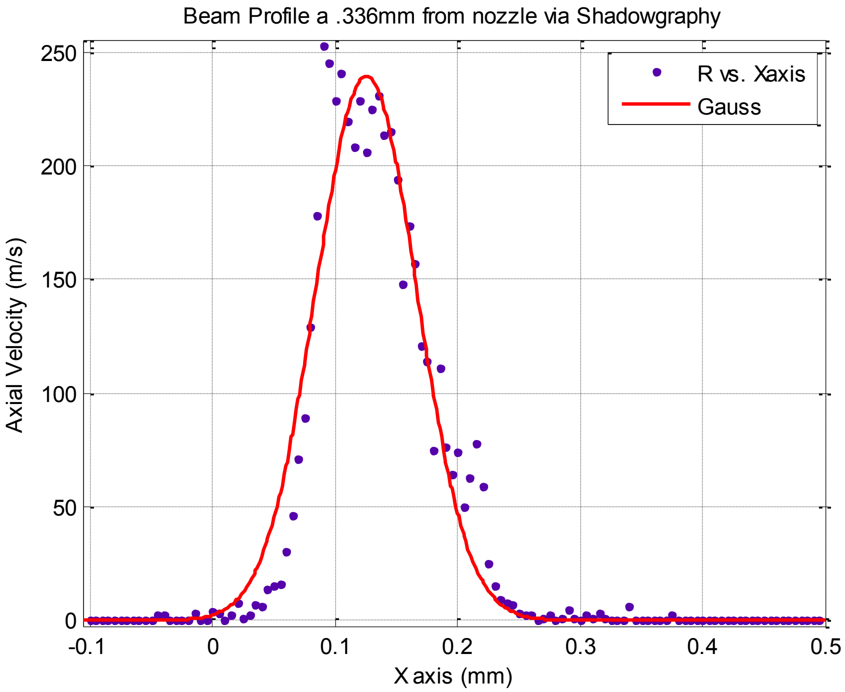

Figure 24. Matlab generated Gaussian fit to histogram for 180 sccm flow through inlet condition nozzle.

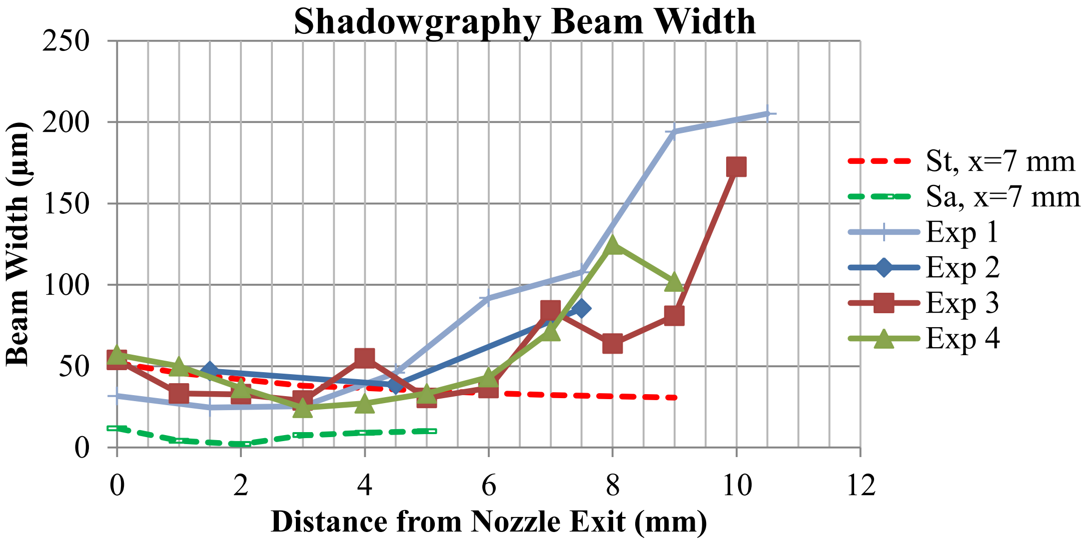

Figure 25. Comparison of modeling results and experimental results for 180 sccm flow though the linearly converging nozzle.

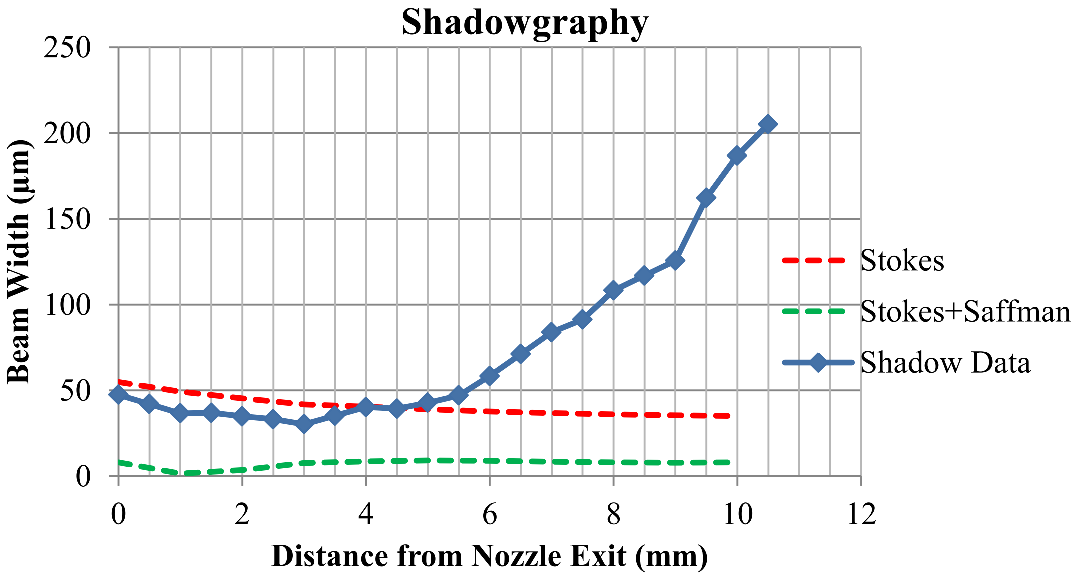

Figure 26. Averaged experimental results compared to modeling results for 180 sccm flow through the linearly converging nozzle.

The experimental results in Figure 26 show that the beam widths are slightly smaller than the model predicts with only applying Stokes force. This trend matches to a distance of about 3 mm after which the beam begins to diverge. Stokes force does not account for this divergence. Saffman force however does predict a divergence beginning at 2 mm. The width of the beam matches closer to Stokes force but the shape of the beam has slight resemblance to a beam where Saffman force plays a role.

Shadowgraphy is a direct measurement technique and offers very accurate results, but due to the relatively low data output, requires long acquisition periods. This low data output stems from the rate at which the data was acquired which only occurs during the 10 nanosecond laser pulse. A short laser pulse is required to acquire a quasi-instantaneous image of the particle. As this is determined by the laser system, there are no parameters for increasing the pulse duration. With no control over the duration of the laser pulse, the rate data acquisition can only be increased by decreasing the time between pulses. This is limited then to the rate at which the computer can communicate with the camera. For double frame acquisition, required for velocity calculations, the computer can process images at 4.96 Hz. This results in a maximum rate of approximately 50 ns of data acquisition per second of run time or 180 μs per hour. Because of this slow data acquisition rate a more efficient method for calculating beam widths is preferable. While acquiring beam widths with shadowgraphy is highly accurate as it is a direct measurement of the particles locations, the resulting beam widths may still be missleading. Error can arise during the fitting of the gaussian curve to the particle distribution histogram. The results are sensitive to bin size for small beam widths.

3.4.5. Particle Velocity with Shadowgraphy and Relaxed Processing

In addition to calculating beam widths using shadowgraphy, the particles velocity can be measured and used to compare the model to theoretical results. The particles' velocities are a function of their locations with respect to the center of the gas flow;

particles nearest the center experienced greater acceleration and had higher velocities. Because the particle locations were unknown, it was impossible to determine their radial distance from the center of the gas flow, making comparison for off axis particles impossible. However, it was known that the fastest moving particles would be traveling along the centerline of the gas flow. This suggested that comparing the peak particle velocity of the theoretical results with the peak particle velocities of the experimental results should yield similar results. Shadowgraphy was used to collect data sets which were converted to particle lists. The corresponding velocities were filtered to remove erroneous vectors such as the examples illustrated in Figure 13. The accurately identified velocity vectors were then sorted, and the maximums recorded. This process was performed at different vertical locations (y-axis) ranging from the nozzle exit to 7 mm past the exit. Also to ensure that the center of the beam was captured, data was collected and processed at different depths in the particle beam (z-axis) specifically z = 0 and ±50 μm (as defined by centering with the CW laser). The results, presented in Figure 27, show a good match at the nozzle exit, but immediately begin to diverge from the theoretical results. The experimental results show increasing lower peak velocities as the distance from the nozzle exit increases. A challenging aspect of measuring the peak axial velocties was gathering large enough data sets to ensure that the data set's peak velocity was accurate. The experiements were long enough for the software to recognize a large number of particles, but relatively few velocity vectors were identified. After investigating, it was realized that the processing parameter controlling the time between exposures (dt) was set to 10 μs, which resulted in the fast moving particles traveling distances longer than the height of the screen. The experiments were repeated using a dt of 1 μs. The results are shown in Figure 28. The experiments in Figure 27 have been averaged and included in Figure 28.

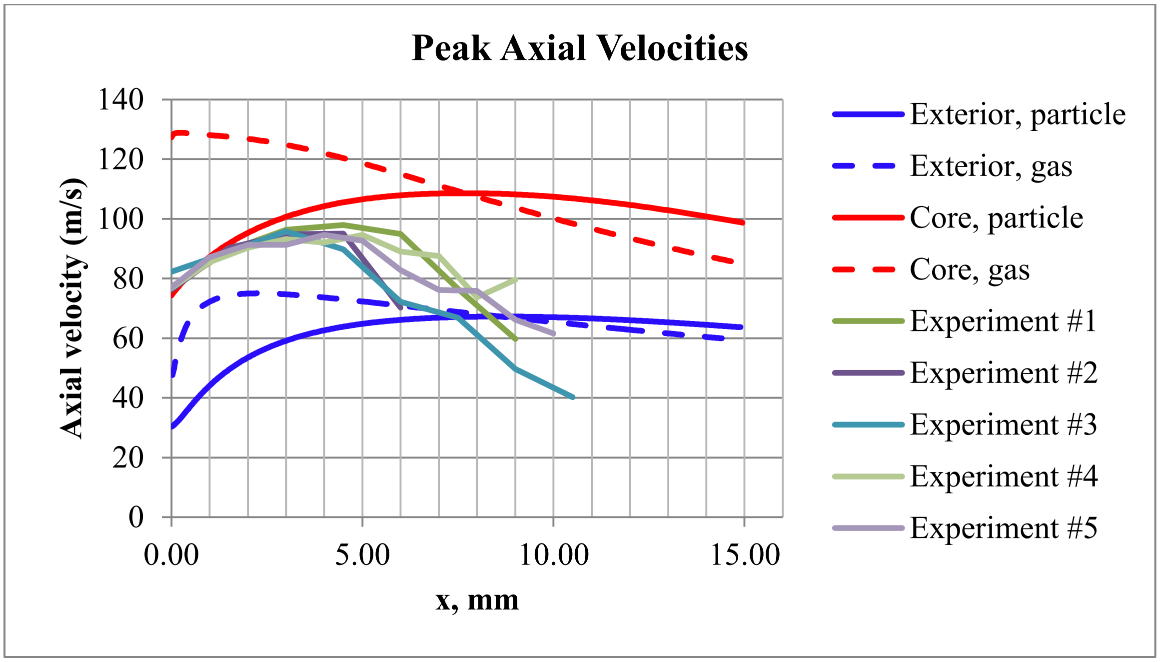

Figure 27. Graph of peak axial velocities of silica particles flowing through linear converging nozzle with total flow rate of 180 sccm.

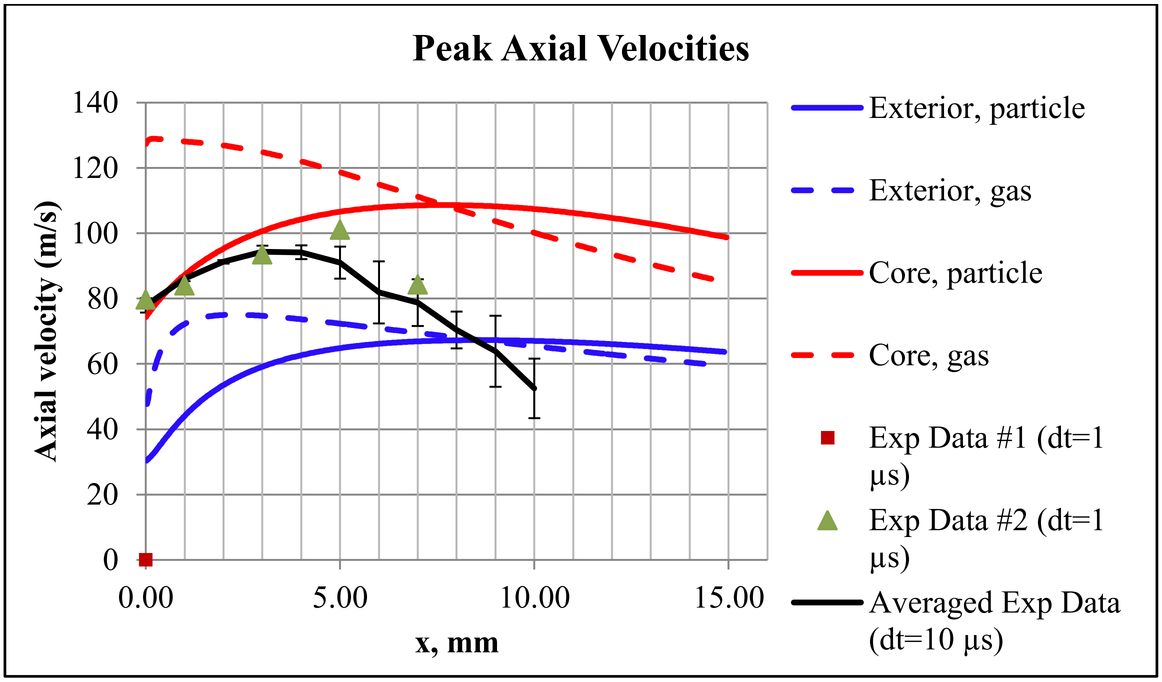

Figure 28. Comparison of the peak axial velocities after *dt* has been adjusted from 10 μs to 1 μm.

The result of changing the time between exposure from 10 µs to 1 µs did have a positive effect on the experimental results in that it increased the measured peak velocities. However, the peak velocites still did not match the modeling results. This raised doubts in the accuracy of the measurements of the velocity vectors. The timing setting of the shadowgraphy system was checked to ensure that the laser pulse was occurring during the exposure time of the camera. If the timing settings did not match, velocity vectors lengths would be incorrectly measured. An oscilloscope and a laser detector were used to measure the time between laser pulses. The *dt* setting was varied as shown in Table 4, along with the experimentally measured time between laser pulses, *Δt.*

Table 4. Comparison of *dt* setting in Davis software with measured *Δt* by laser detector with oscilloscope.

dt setting in Davis (µs)	*Δt measured by osciliscope (ns)*
0.4	399
0.6	597
.08	797
1.0	998
1.2	1.198
1.4	1.39
2.0	1.998
4.0	3.996

The experimentally measured time setting matched within a few nanoseconds of the Davis setting ensuring that the velocity vectors were calculated correctly.

These conclusions suggest that the velocity measurements were accurate and the theoretical model needed to be reexamined. It was determined that compressibility was playing a role in the calculations causing overestimation of the particle velocity. After using an iterative approach to correctly specify inlet pressure such that the outlet gas flow rate matched the flow rate set in the experiments the particle velocity was recalculated and, as shown in Figure 29, matched experimental results.

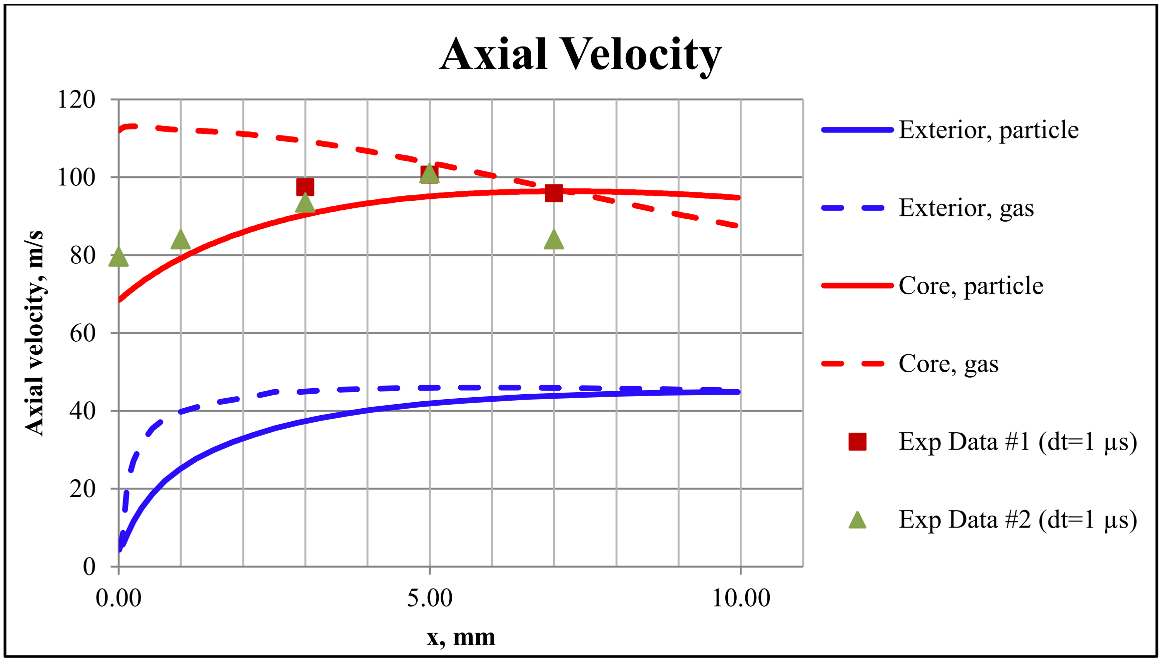

Figure 29. Experimental results matching adjusted modeling results.

An alternative representation of the data was sought to offer a better look at the velocity comparison. This was achieved by looking at all of the velocity results as compared to only the peak results. Although still unable to determine the radial position of the particles, it was decided that by examining the profile of the axial velocites from the z-axis, the distribution of the velocites in the x-axis could be compared with theoretical results. This allowed for matching the particle velocities along the center slice (x-y plane though the centerline) of the beam as compared to only at the center of the gas flow.

Comparing the experimental and theoretical velocity profiles, showed similar trends in both peak velocity and the profile shape. The process was repeated for a flow of 120 sccm to to offer another compartison of the results and to illustrate consistency at a flow rate much closer to the flow used during actual printing processes.

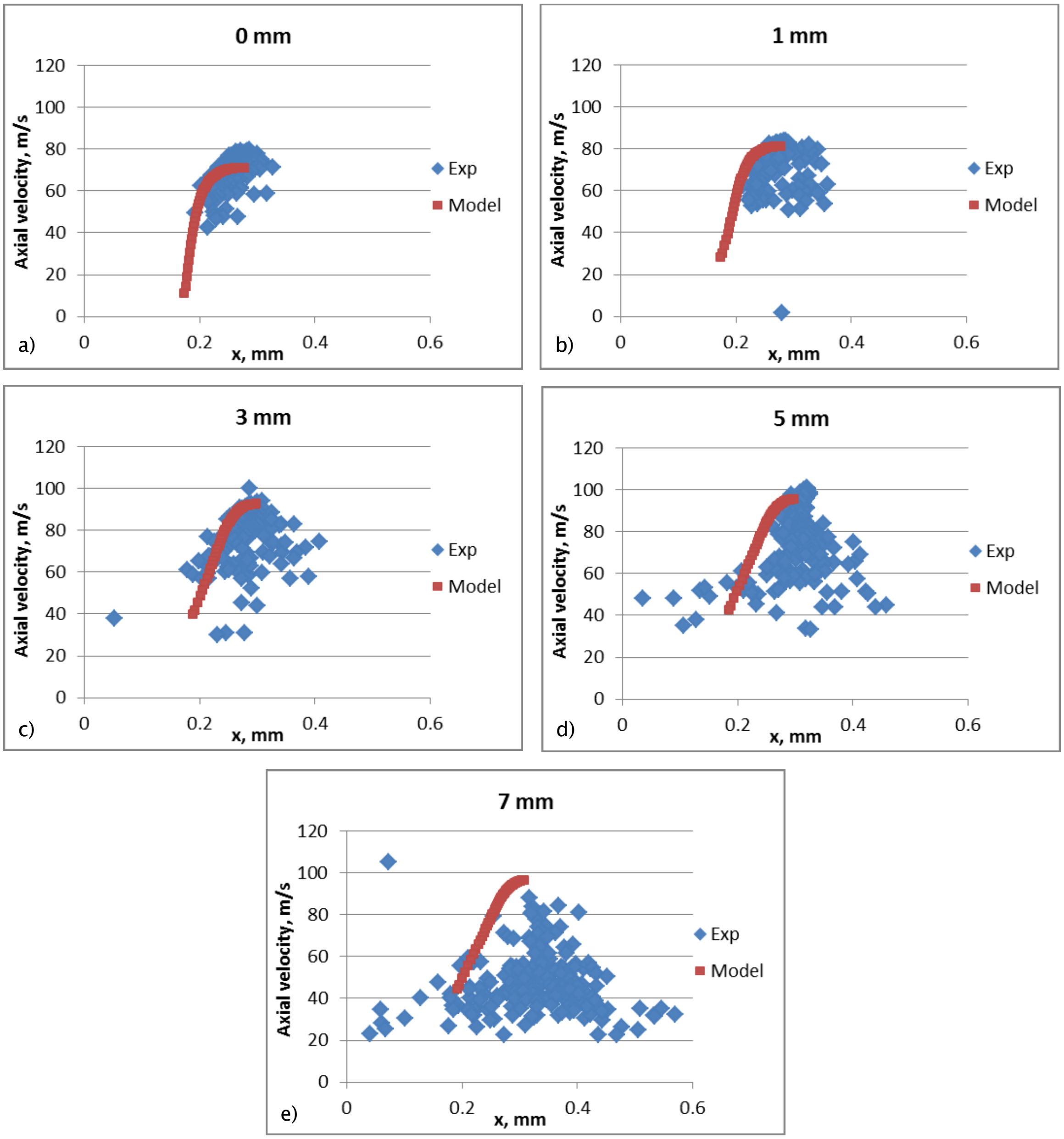

Figure 30. Axial velocities for silica particles through a linear converging nozzle with a flow of 180 sccm at a) nozzle exit, b) 1mm, c) 3mm, d) 5mm, e) 7mm.

The results in Figure 31 show that the particle velocities match well with the modeling results at a flow rate of 120 sccm. Some particles were identified with unusually high velocities. After manually checking it was determined that the particle velocities were correctly calculated. While no explanation was discovered for this discrepancy, these values were still considered erroneous because they were outside of the standard deviation of the peak particle velocities. From these results it was concluded that the model is correctly predicting the particle velocity suggesting that Stokes force is being modeled appropriately.

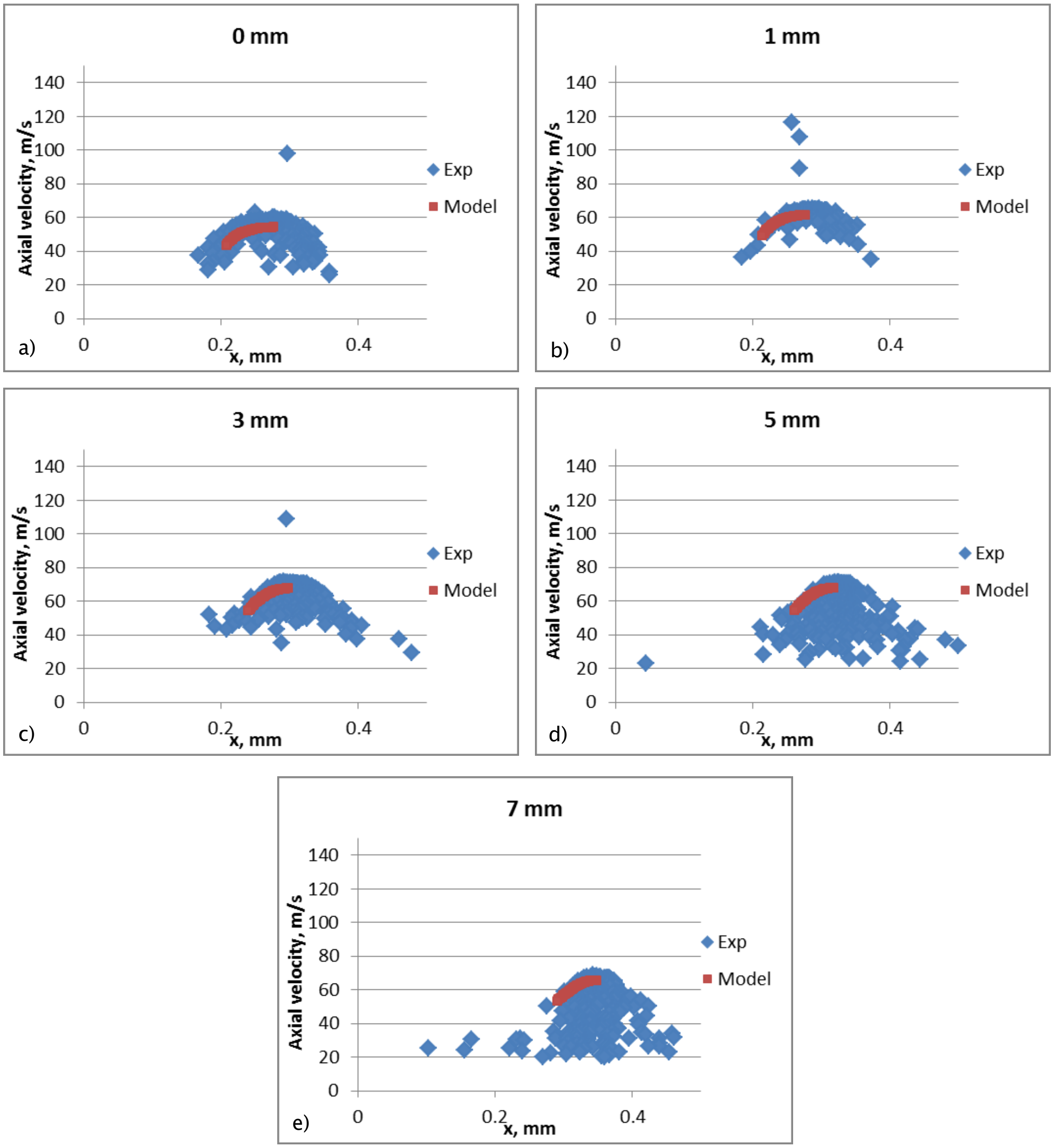

Figure 31. Axial velocities for silica particles through a linear converging nozzle with a flow of 120 sccm at a) nozzle exit, b) 1mm, c) 3mm, d) 5mm, and e) 7mm.

3.4.6. Inlet Conditions via Shadowgraphy with Relaxed Processing

The theoretical model requires input information regarding the percentage of area which the particles occupy when entering the nozzle inlet. Because the nozzle inlet is inside the deposition head, it is impossible to examine this beam width directly without destroying the deposition head. Initial efforts were to attach a straight section which was cut to the shortest length possible which allowed for viewing with shadowgraphy. It was hoped that this short straight section would have a minimal effect on particle focusing and the resulting beam width would accurately reflect the inlet conditions. Polyurethane and Peek tubing were cut to lengths of approximately 8.3 mm and inserted into the deposition head. Although this technique produced seemingly reasonable results, it was impossible to check its accuracy. For that reason the straight tube was replaced with a nozzle identical to the deposition nozzle that had been cut to a shortened length of 6.83 mm. The inlet conditions were measured with shadowgraphy (see Figure 22, Figure 23, and Figure 24) using this inlet condition nozzle, and the model was adjusted such that the particles were introduced 6.83 mm from the actual inlet. Measuring and processing inlet conditions in this manner was the most accurate reasonable technique available. The inlet conditions seemed to vary from experiment to experiment during the 180 sccm flow. For that reason, a variety of inlet conditions were used in the theoretical modeling. Those values are listed in Table 5.

Table 5. Inlet condition beam widths.

Total Gas Flow Rate (sheath +carrier)(sccm)	*Beam Width (μm)*
40	410
120	260
180	260, 311, 360, 516

3.5. Mie Scattering

While the shadowgraphy techniques were successful in characterizing the particle beam, another method was investigated to both solidify the shadowgraphy characterization techniques and to decrease the data acquisition times. As mentioned previously, the CW laser was used to center the particle beam before shadowgraphy experiments were performed. This technique, illustrated in Figure 32, views Mie scattering of the CW laser off the particle beam. The scattered light is recorded by the camera. Compared to shadowgraphy, in which the laser is pulsed, the CW laser is continuous. This allows for increasing data acquisition rate by increasing the cameras exposure time. Typical setting would range from 20 milliseconds to 60 milliseconds which results in acquiring data approximately 10^6 times faster than shadowgraphy. Also this technique does not require the double frame acquisition but subsequently is unable to measure particle velocity.

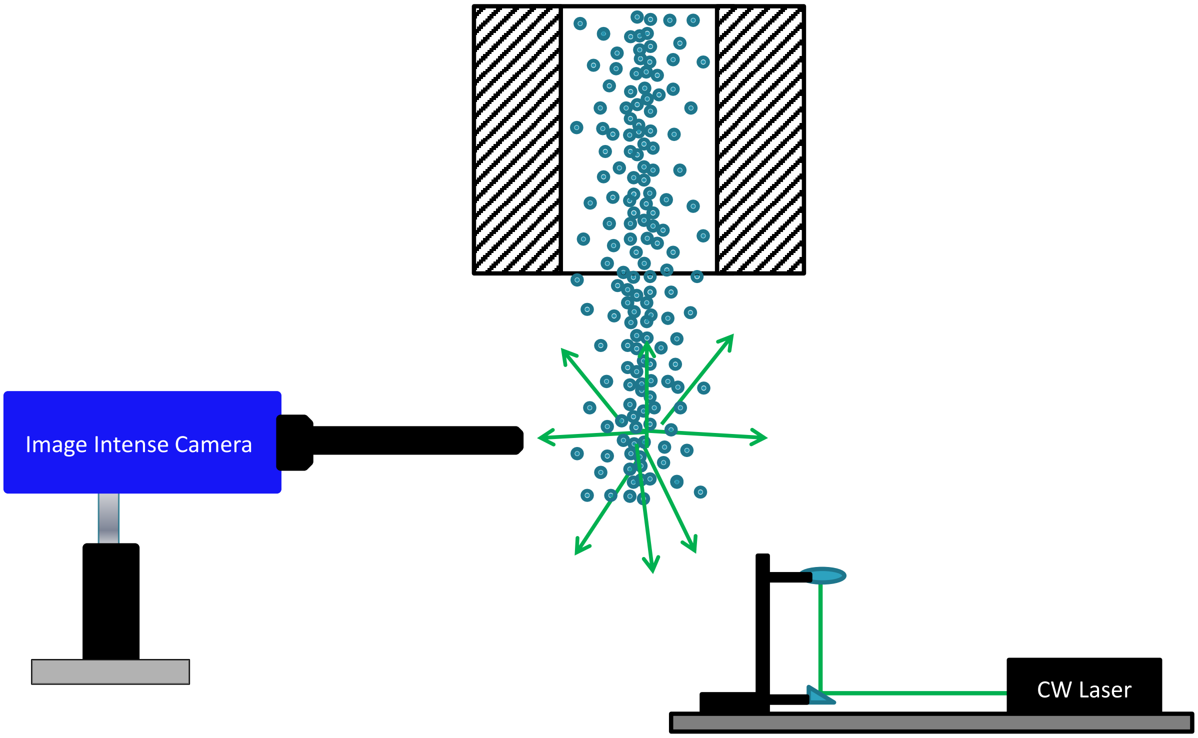

Figure 32. Cartoon illustrating Mie Scattering of CW laser off silica particles.

3.5.1. Beam Widths

Typical experiments involved acquiring 100 images, at different distances below the nozzle exit. In these images brighter pixels correspond to higher intensity and therefore represent higher particle concentration. A particle density profile can be created through any row of pixels with the x-axis being the pixel location and the y-axis intensity. Figure 33, shows an example of a particle beam with the associated intensity profile.

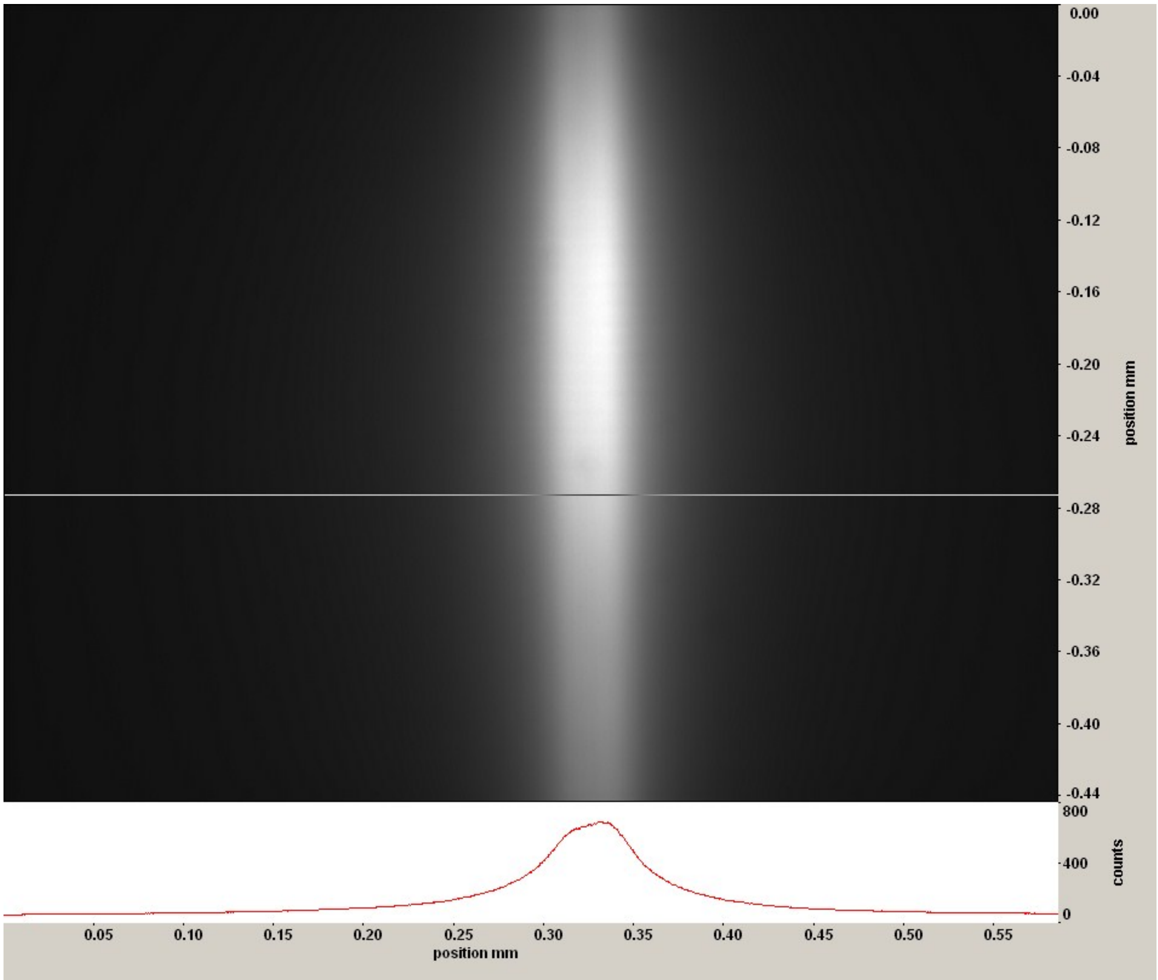

Figure 33. Averaged CW image of particle beam with intensity profile through cursor line.

These images are processed using the Matlab algorithm BWCalc.m. This algorithm normalizes the data then examines 10 rows of pixels through the brightest section of the beam. It searches for the edges of the beam in each row by identifying pixels where the intensity corresponds to a percentage of the normalized intensity, such as half max, 1/e, or 1/e^2. The distance between these edges defines the beam width for that row of pixels. The 10 beam widths are averaged and the result is the beam width for the image. It should be mentioned that for large steady beam widths with movements in the x-direction much smaller than the beam width, it is appropriate to calculate the beam width of the averaged images. The 100 images taken at each distance from the nozzle exit are averaged in Davis before being exported for Matlab processing. Alternatively, for very thin beams, where any translation in the x-axis would be on the same order as the beam width, the 100 images are not averaged before Matlab processing. Instead the beam widths are calculated for each of the images and the 100 resulting beam widths are averaged. Summarizing, for large beams, the single beam width for the averaged 100 images is calculated. For small beams, the 100 beam widths for each image are averaged. This process was applied to a beam of silica particles flowing through the linear converging nozzle at a rate of 180 sccm. The beam was relatively large and therefore the images were averaged in Davis and the beam widths of the averaged images calculated. The results for 3 experiments are shown below in Figure 34.

The results of these three experiments were averaged and standard deviations calculated. The averaged results, shown in Figure 35, show that the experimental beam widths match reasonably well to the beam widths expected when only Stokes force is focusing the particles. There are large divergences at the beginning and end of the partile beam. The divergence at the beginning is suspected to be artificial due to scattering from the nozzle. However, the divergence at the end has yet to be accounted for.

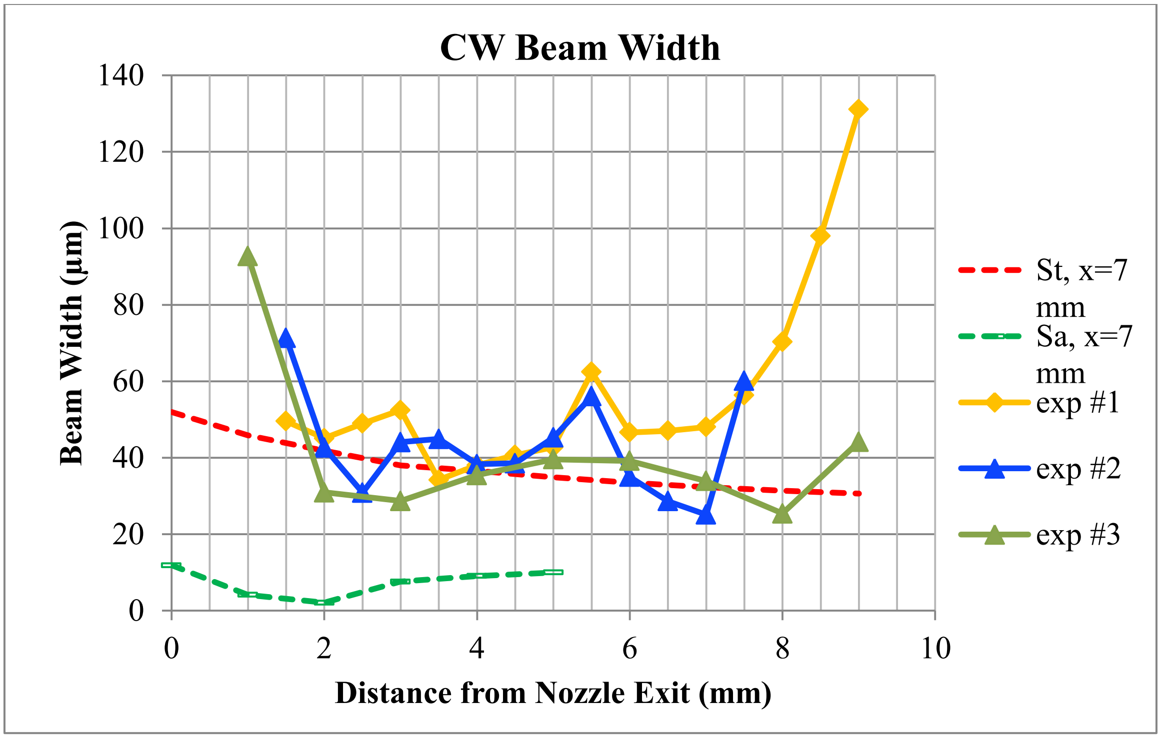

Figure 34. Beam width results from Mie scattering experiments for 180 sccm flow through linear converging nozzle.

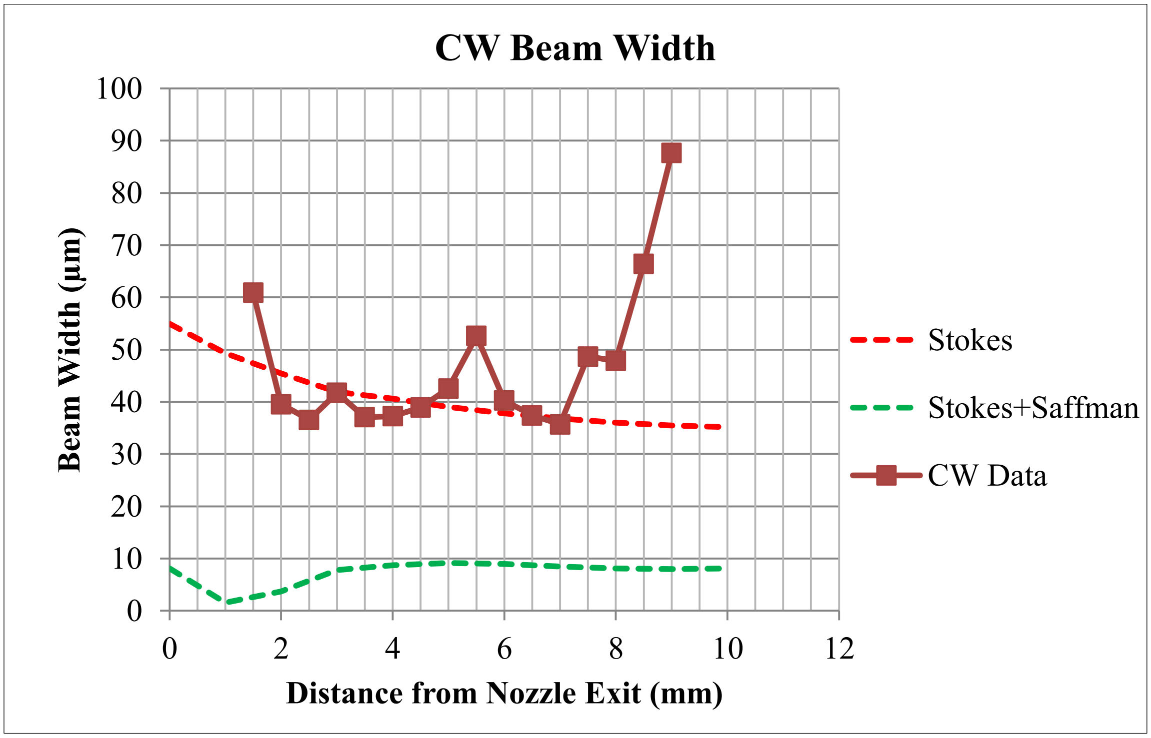

Figure 35. Averaged beam width results from Mie scattering experiments for 180 sccm flow through linear converging nozzle.

3.5.2. Inlet Conditions

Typical experiments make visualization of the particle beam at the exit of the nozzle with Mie scattering challenging because the nozzle usually reflects much more light than the particle beam. To prevent over exposure of the camera the exposure time must be decreased and subsequently there is not enough scattering from the particle beam for visualization. This is exceptionally pronounced when the tungsten carbide nozzle is used due to its highly reflective nature. Comparatively, the ceramic nozzle produces less scatter. Unfortunately, the scatter still is too intense for visualization of a focused particle beam exiting the two stage converging ceramic nozzle. If the particle concentration could be increased such that the beam reflected a comparative amount of light as the nozzle, the beam would be visible. This situation occurs when the ceramic inlet condition nozzle is used. The large increase in particle density can be seen at the exit of the nozzle in Figure 36. This technique was used to confirm the findings in Table 5. The variation seen from experiment to experiment was still unaccounted for and was attributed to inconsistencies in atomization.

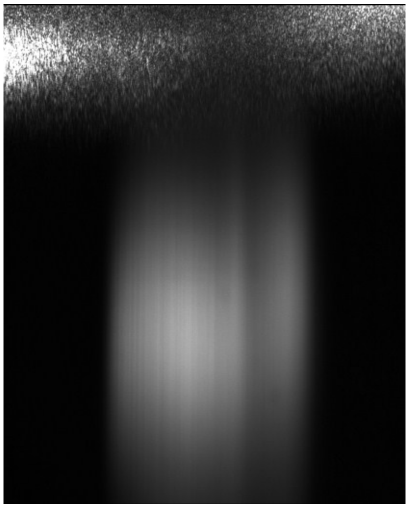

Figure 36. Inlet conditions out of inlet condition nozzle via Mie scattering with CW laser.

It is likely, that these effects are noticeable during the inlet condition experiments and not during the converging nozzle experiments due to the lack of particle focusing during the prior.

3.6. Comparison of Mie Scattering and Shadowgraphy Beam Width Results

After developing two beam width measuring techniques, and applying these techniques to flow through the linear converging nozzle, at 180 sccm, with 3.8 µm silica particles, it was found that the measured beam widths were in agreement. The CW experiments over estimated beam widths at the nozzle exit due to scattering off the nozzle. Both experiments, shown together in Figure 37, indicated divergence of the particle beam however shadowgraphy indicated this divergence earlier. Two to six µm from the nozzle exit, both experiments matched very well with the beam width as predicted by Stokes force only model. While these results are fairly conclusive, different nozzle geometries would make focusing due to Saffman force more pronounced.

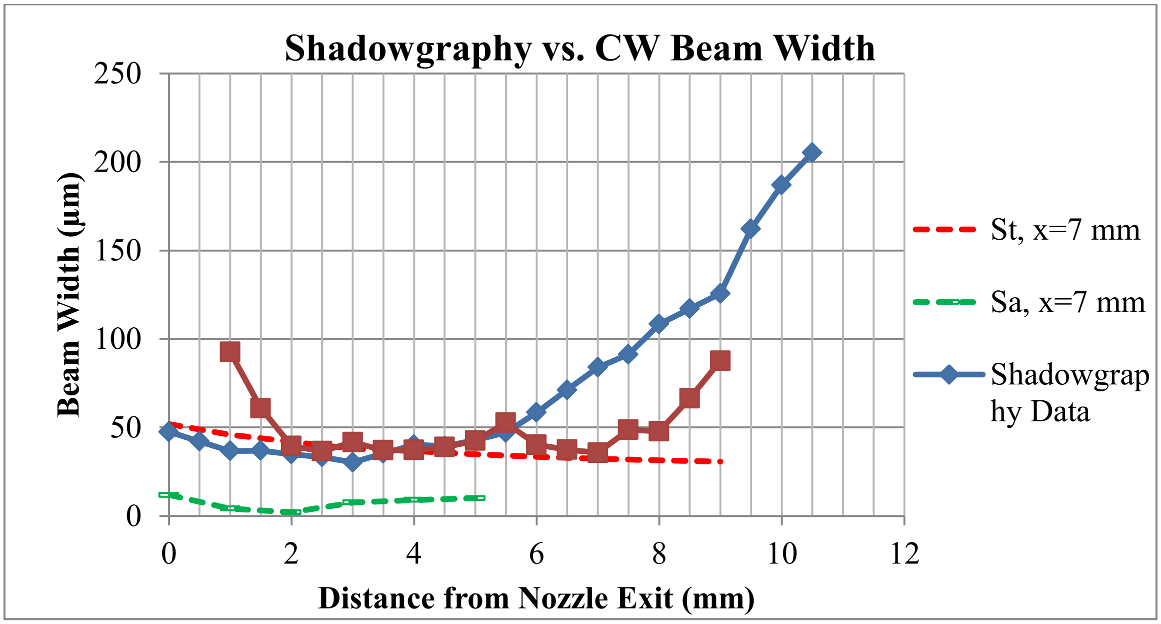

Figure 37. Comparison of CW and Shadowgraphy beam widths for 180 sccm flow through a linear converging nozzle.

3.7. Small Particle Sizing Algorithm

This section is an excerpt from “Development of a Small Particle Sizing Algorithm for sub-10 μm Particles using Shadowgraphy”, presented in the ASME conference proceedings in Houston, TX, 2012, by Michael Robinson et al. [28].

Characterization of aerosol borne particles has paramount importance for the performance of aerosol-jet direct write technologies. Particle characterization in general includes size, velocity, and location with respect to the jet axis. The aerosol jet typically consists of poly-dispersed particles ranging from submicron to 10 μm in sizes. Currently available particle sizing methods are limited to measuring particles within a narrow depth-of-field and are capable of measuring particles of 5 μm or larger in diameter [19]. The research demonstrates a unique method capable of measuring particles' sizes of 1 – 10 μm and locations outside the depth-of-field of the imaging system with reasonable accuracy.

3.7.1. Algorithm and In-focus Criteria

The experimental apparatus, Figure 38, operated in the following manner: A Quantel USA Inc. dual cavity Nd:YAG 532 nm Q-switched laser was converted into incoherent light by a high efficiency diffuser that uses a fluorescent dye. A light guide fiber delivered incoherent light through a collimating Fresnel lens. The light was then attenuated by neutral density filters. Filter optical densities were selected such that an intensity of approximately 2500-3500 counts was achieved while the laser power was maximized. This created consistency between laser pulses without over exposing the Imager Intense Camera. The camera optical system included a 12X variable zoom lens and a 10X objective lens that has a depth-of-field of less than 12 μm. A linear translation stage was used as a mount for the glass slides and was controlled by a Newport ESP 100 Motion Controller. The entire system was located on an active isolation self-leveling frame with an optical honeycomb breadboard. Davis Software version 7.2 was used for minor initial preprocessing which included particle identification and location in the x-y plane and velocity measurements.

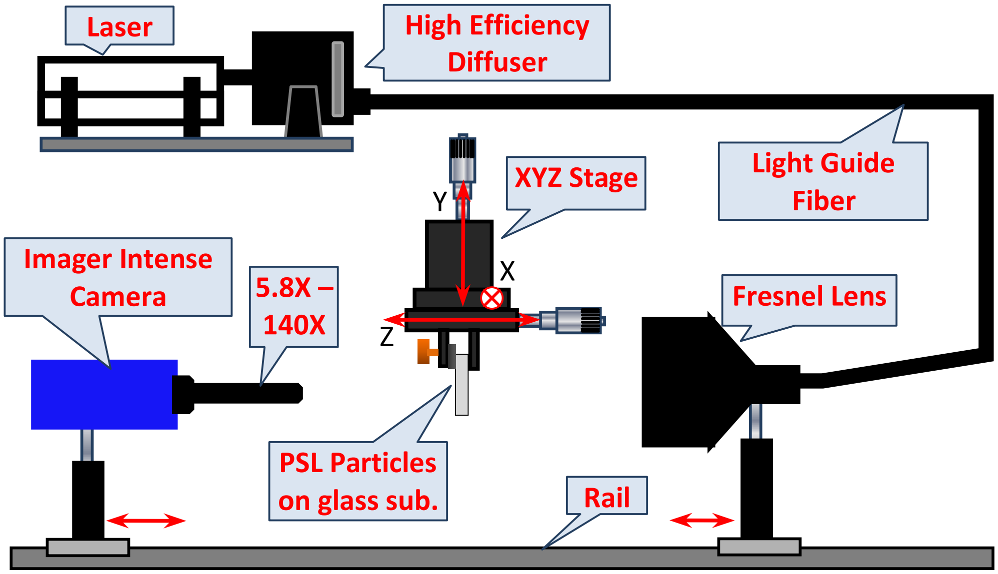

Figure 38. Experimental shadowgraphy apparatus [28].

Table 6. List of sizes and standard deviations of PSL spheres used for calibration curves and experimental data[28].

Particle Size (µm)	*Size (µm)*	*Std. Dev. (µm)*
1.0	1.010	0.021
2.0	2.077	0.045
3.0	3.004	0.065
4.7	4.770	0.177
5.8	5.883	0.283
10.0	9.977	0.412

The particle sizing algorithm identifies two in-focus criteria of the diffraction pattern created by a particle, image size and image slope. The combination of these two characteristics is unique to a particle of a given size at a given z-position, therefore over a specified operating range there will not exist two particles that have the same image size and image slope but differ in size or distance from the object plane of the camera. This allows the SPSA to simultaneously determine the size of a particle as well as its distance from the object plane.

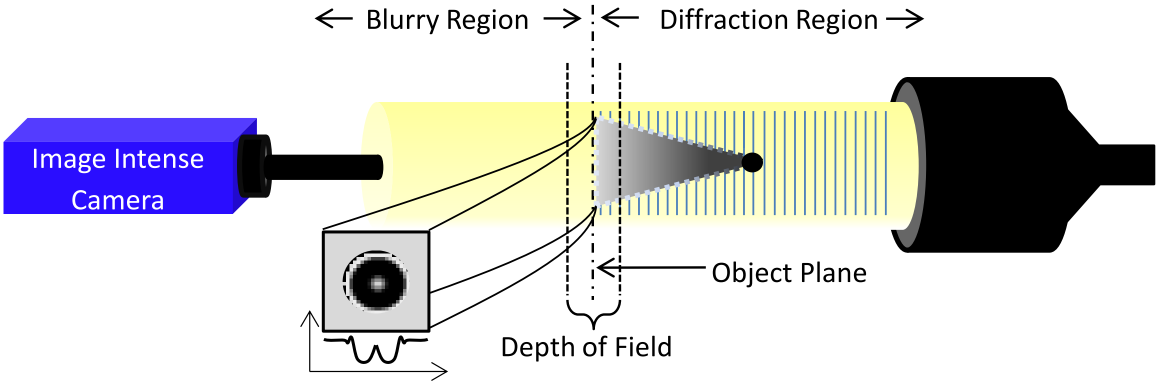

Figure 39. Diagram of particle illuminated by shadowgraphy system creating a diffraction pattern [28].

1.0, 2.0, 3.0, 4.7, 5.7, and 10.0 μm polystyrene latex (PSL) particles (Polysciences Inc., Warrington, P.A.) were diluted with deionized water and deposited on glass slides using a micro-pipette and allowed to dry. The sizes and standard deviations are listed in Table 6. Once dried, the slides were mounted individually on the translation stages. The coordinate system is defined such that the slide is in the x-y plane while the z-axis (camera system optical axis) is orthogonal to the slide. Two regions are now defined, the "Diffraction Region" and the "Blurry Region". The diffraction region (see Figure 39) refers to particles located in and between the object plane and the light source until the particles are no longer distinguishable from the background intensity. When particles in this region are out of the depth-of-field, the camera sees their diffraction patterns in the object plane. Meanwhile, particles between the object plane and the camera that are not in the depth-of-field are out of focus. Because of this, all images of particles in this region are "blurry".

Figure 40 illustrates the differences between the same particle in the diffraction region, object plane and blurry region. From Figure 40, the same size particle, on opposite sides of the object plane, produces dissimilar diffraction patterns. For this reason, the SPSA was designed to apply only to particles located in the diffraction region. All distances referring to the z-axis are assumed to be in the diffraction region unless specified otherwise.

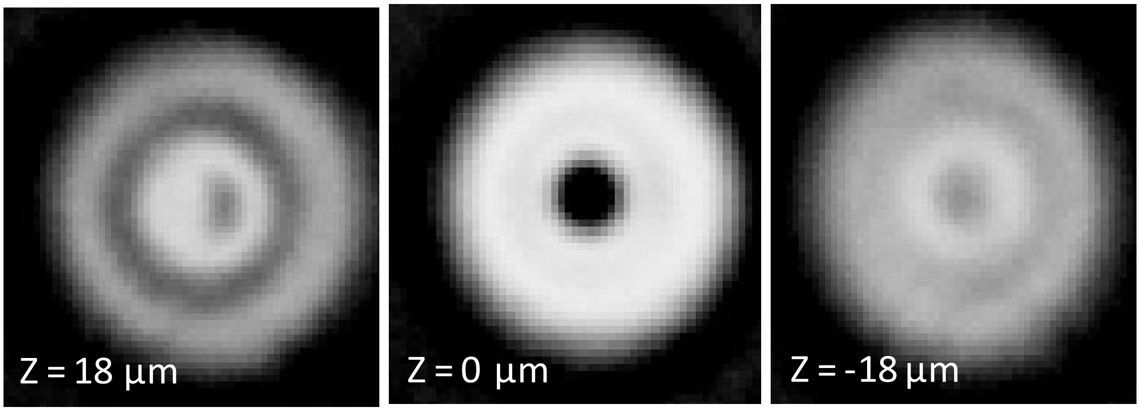

Figure 40. The left, center, and right images show inverted images of a particle in the blurry region, object plane, and diffraction region, respectively [19].

Two different magnifications were used such that a reasonable number of particles over the range of 1.0 µm to 3.0 µm particles (57.8X) and 3.0 µm to 10.0 µm (23.4X) could be captured in the image window without adjusting the camera magnification. Particles were translated to the center of the object plane manually using the linear stage. This plane of best focus was specified as an approximate z = 0 µm position. Due to misalignment and the slight non-coplanar nature of the particles the actual z = 0 position is adjusted later in the algorithm. Beginning at the approximate z = 0 µm, the slide was translated into the diffraction region using the Newport ESP 100 Motion Controller. An image was taken at each interval. Once the images were acquired for each slide, the system was calibrated and the magnifications were found to be 0.173 and 0.427 µm/pixel.

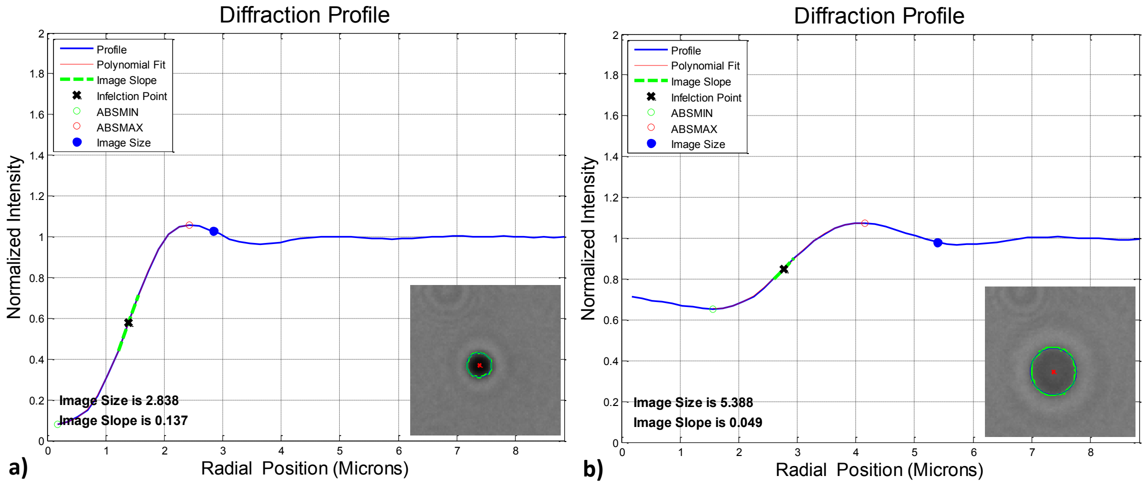

Figure 41. Radial diffraction profiles of a particle 15 µm into the diffraction region (a.) and 15 µm into the blurry region (b.) [28].

Processing of the data using Davis Software created particle lists numbering all recognized particles and measuring particle location coordinates in the X-Y plane. Images were exported from Davis as 16 bit Tagged Image Format file, but the resolution of the Imager Intense Camera limited actual resolution of the image to 12 bit. Images were imported into Matlab version 7.0 as 16 bit files to ensure the no data was lost in compression. The particle location recorded by Davis software was used to define a cropping window around each particle for analysis.

The in-focus Criteria, Image size and Image slope, for a diffraction pattern are calculated by standard image processing techniques. Image size is calculated by determining a gray-level threshold intensity for the image using Otsu's principle. Otsu's method [29] searches for the intensity which minimizes intra-class variance of an image. The intra-class variance is defined as.

$$\sigma_w^2(t) = w_1(t)\sigma_1^2(t) + w_2(t)\sigma_2^2(t), \tag{8}$$

where $\boldsymbol{w_i}$ represents the probabilities of the two classes and $\boldsymbol{\sigma_i^2}$ is the variance of each class individually if separated by a threshold $\boldsymbol{t}$. Otsu's method minimizes the difference between the number of pixels in an image which are above the threshold and the number of pixels below the threshold by varying the threshold value. The values of w_i, σ_i^2 and ultimately t are software generated through the use of the MATLAB function "graythresh" which was applied to the cropped window of each particle.

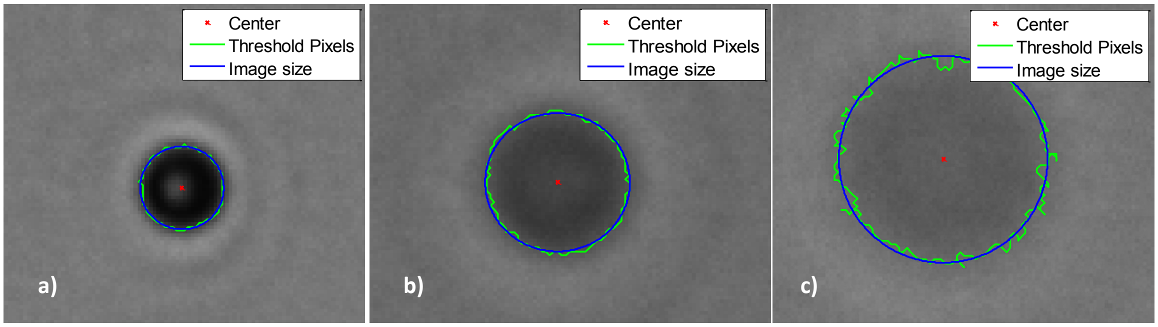

Figure 42. Diffraction profiles of the same 3.0µm PSL sphere at z = 0 µm (a), z = 15 µm (b), and z = 30 µm (c) into the diffraction region. The corresponding image sizes are 3.8 µm, 6.3 µm and 9.5 µm, respectively[28].

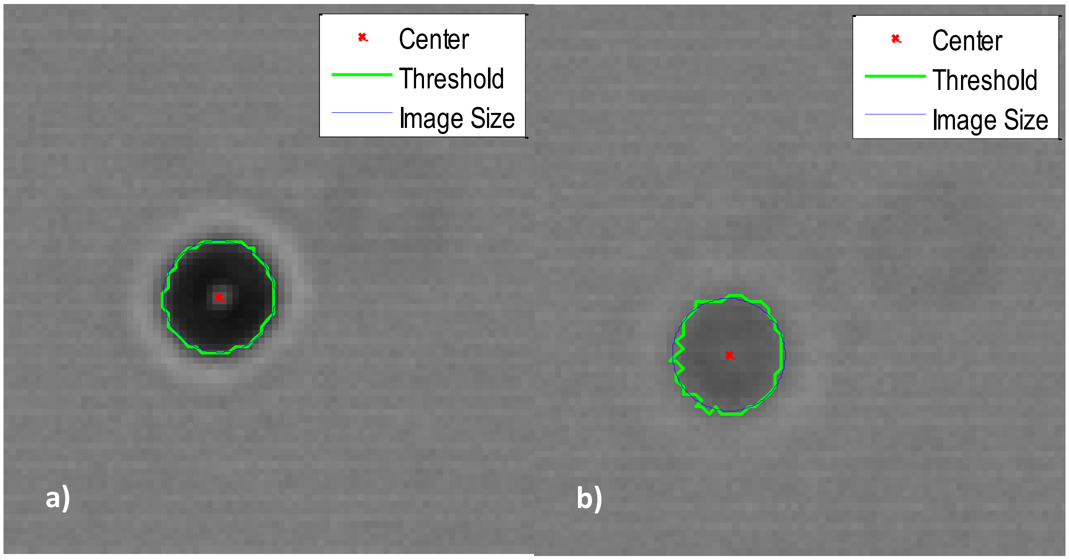

Figure 43. (a) A 3.0 µm particle with an associated image size of 7.31 µm at z = 41 µm from the object plane. (b) A 5.8 µm particle with an associated image size of 7.27 µm at z = 8 µm from the object plane [28].

Once the gray level threshold is found using Otsu's method, the image is then scanned in search of locations where the pixel intensity transitions across the threshold. After these locations are identified a circle is fit to the highlighted pixels, the diameter of which is specified as the image size.

Figure 42 shows three images of the same 3 µm particle at different z-positions and the associated image size. The image to the left at z = 0 shows that in the object plane image size is similar to particle diameter. However, as the particle moves from the object plane towards the light source (Fresnel lens), increasing its z-position, (center and right images in Figure 42), the image size increases and therefore no longer accurately identifies the particle's diameter. Because image size changes with z-position, it alone cannot be used to determine particle size. Figure 43 shows a 3 µm particle (a) and a 5.8 µm particle (b) at different z-positions which have approximately the same image size. In order to distinguish between them another parameter is required, image slope.

Image slope is calculated by finding the maximum slope between the absolute max and absolute minimum in the particles diffraction profile. Diffraction profiles were calculated in two different manners initially, shown in Figure 44. The first technique generated profiles by plotting the intensities of the row of pixels traveling though the center of the diffraction pattern. The second technique improved upon the first by including the information from all the pixels in the image instead of only the center row. The radial distance of each pixel from the center of the best fit circle was found. The intensities of all particles equidistant from the center were averaged resulting in a radial position vs. average intensity diffraction profile where r = 0 represents the center of the particle. The image slope was calculated from the average intensity diffraction profile. The slope is defined as the steepest slope occurring between the absolute minimum intensity and absolute maximum intensity, which occur just outside of the spot of Arago (center of the diffraction profile) and just outside of the shadows edge, respectively. The slopes along this section are found by fitting a polynomial over this region and evaluating its first derivative at discrete values corresponding to radial distances from the center. Image slope directly reflects the degree of focus of the particle. A particle in the object plane will have a steeper image slope than a particle further from the object plane. This can be explained visually by correlating the image slope to the sharpness of the particle image. High Image slope will be seen as a sharp edge or a rapid transition from the black shadow to the gray background. On the contrary, low image slope will be seen as a soft edge or a gradual transitioning from shadow to background. After calculating the image sizes and image slopes the z-position is adjusted such that z = 0 occurs at the maximum value for image slope and the minimum value for image size. This correction is typically less than 5 µm and does not change the image size or image slope values. However it does greatly decrease the variance seen in the calibration curves.

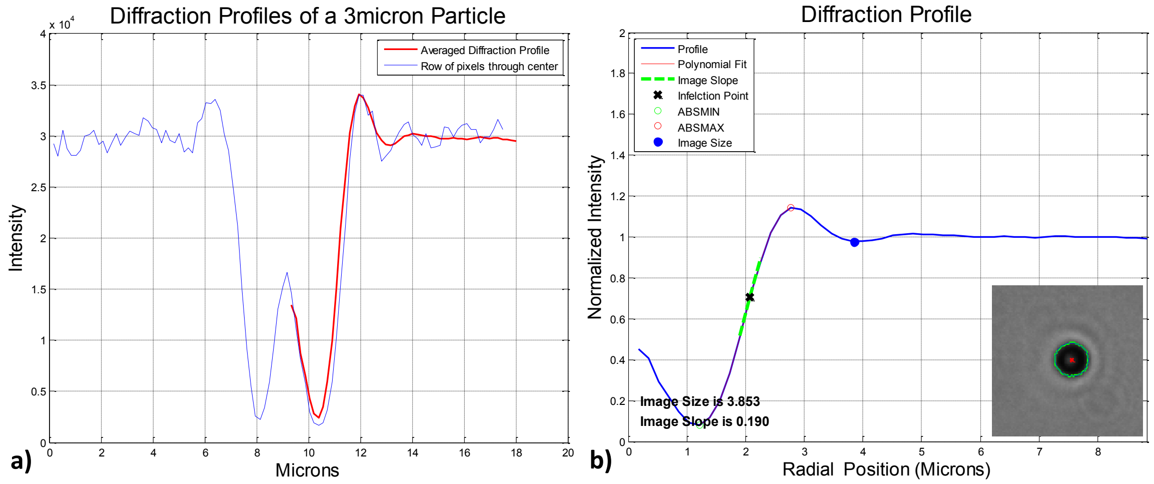

Figure 44. Graph of diffraction profile for (a) generated by a single row of pixels through the particle center and (b) averaged radially[28].

3.7.2. Sizing and Positioning Surfaces

After compiling the experimental data for PSL particles a trend was found relating image slope to image size (Figure 45). The graphs clearly show distinguishable curves for the combinations of image size and image slope which represent different particle sizes. If the image slope and image size of a particle of unknown size are measured, and are consistent with any of the curves in Figure 45, they can be correctly identified on an associated curve. If the data falls between the curves, an interpolation must be implemented.

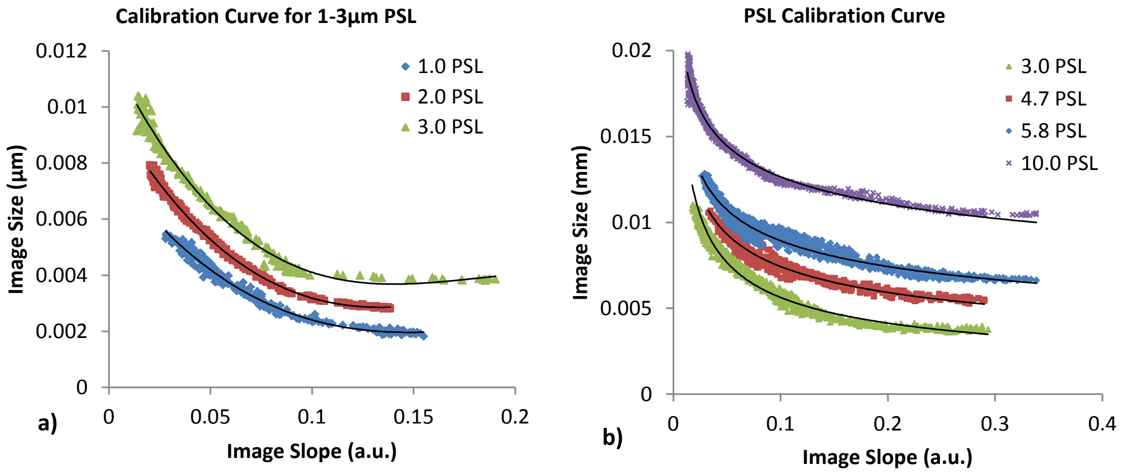

Figure 45. Calibration curve for (a) high magnification, and (b) low magnification[28].

Once it was confirmed that particles of discrete sizes can be identified by optical measurements of image size and image slope, the algorithm was improved to accommodate particles with actual sizes between 1.0 µm and 10.0 µm. Polynomial curve fits were applied to image size and image slope combinations for 1.0, 2.0, and 3.0 µm for the high magnification (57.8X). Power functions fit better to 3.0, 4.7, 5.7, and 10.0 µm particles in the low magnification (23.4X) data. The six particle sizes and their fitting expressions are shown in Table 7 and Table 8.

Table 7. Expressions representing trends relating in-focus criteria at high magnification (0.173 µm/pixel) for 1.0, 2.0, 3.0 µm PSL particles[28].

Particle size	*Expression-High mag. (0.173µm/pixel)*
1.0µm	$y = -0.8079x^3 + 0.5118x^2 - 0.0984x + 0.0079$
2.0µm	$y = -1.125x^3 + 0.7005x^2 - 0.1271x + 0.01$
3.0µm	$y = -1.6306x^3 + 0.8798x^2 - 0.1506x + 0.012$

Table 8. Expressions representing trends relating in-focus criteria at low magnification (0.427 µm/pixel) for 3, 4.7, 5.8, and 10 µm PSL particles[28].

Particle size	*Expression-Low mag. (0.427µm/pixel)*
3.0 µm	$y = 0.002x - 0.445$
4.7 µm	$y = 0.0035x - 0.327$
5.7 µm	$y = 0.0048x - 0.265$
10.0 µm	$y = 0.0081x - 0.193$

Figure 46 displays particle size as a function of image size and image slope for particles ranging from 3.0 to 10.0 µm. After these calibration lines were determined, linear interpolation was used to create data points for the spaces between the expressions for 3.0, 4.7, 5.7, and 10.0 µm particles. This was accomplished through the use of the MATLAB Surface Fitting Toolbox where the x-input, y-input and z-output were the image slope, image size and actual particle diameter from the calibration data, respectively. As image slope decreases below 0.05 a distinction between the 4.7 and 5.8 µm data becomes difficult and the scatter in the data overlaps. Due to this, calibration curves are limited to image slope values above 0.05. The calibration surface in Figure 47 was used to size experimental PSL particles of the same sizes as the particles used to make the calibration data. The image size and image slope of the experimental particles were calculated using the algorithm.

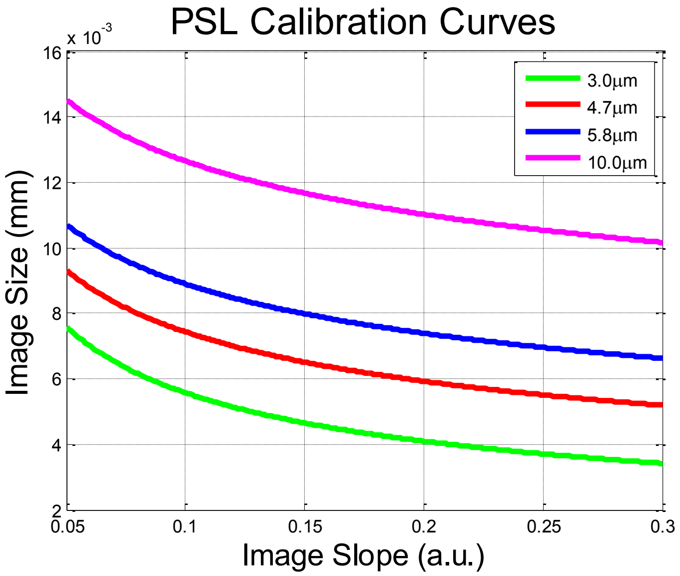

Figure 46. Trendlines for 3.0-10.0μm particles limited to image slopes greater than 0.05 due to near overlap of image size and image slope combinations of 4.7 and 5.8μm particles far from the depth of field[28].

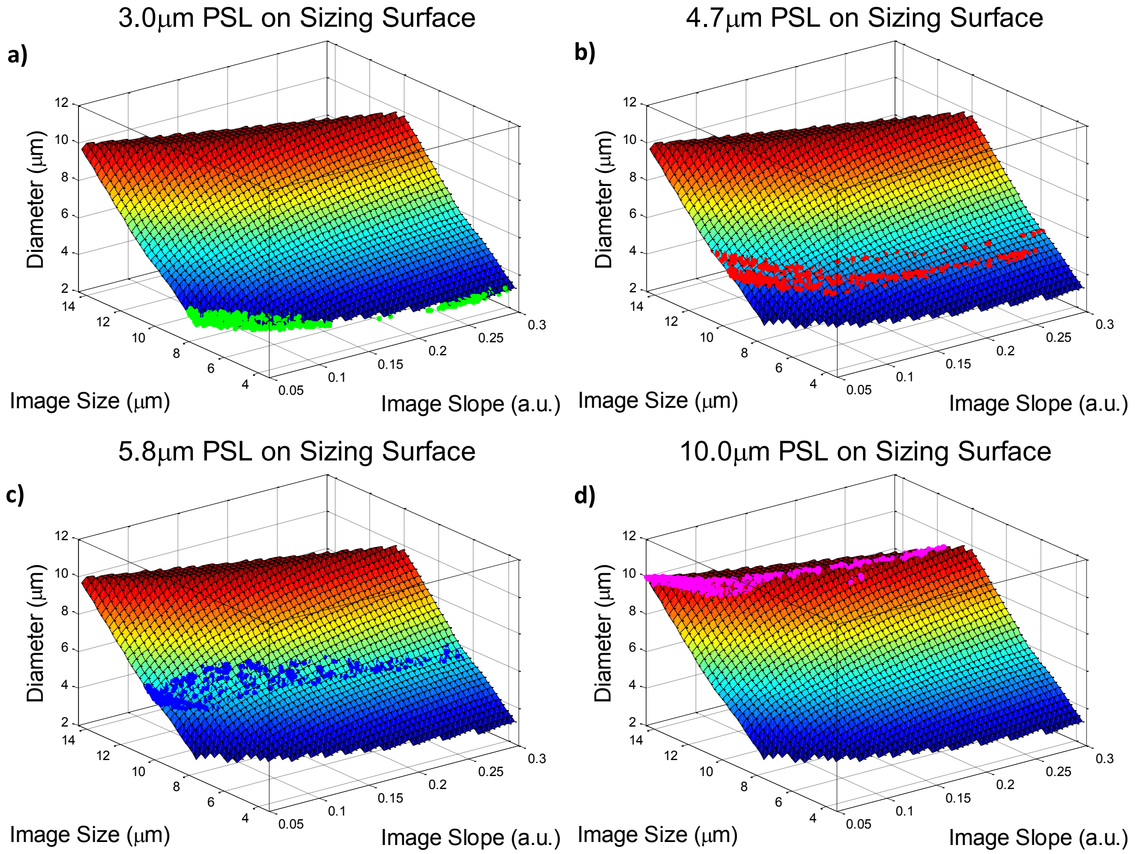

Figure 47. Sizing calibration surface for PSL particles of a) 3.0 μm, b) 4.7 μm, c) 5.8 μm, and d) 10.0 μm diameter[28].

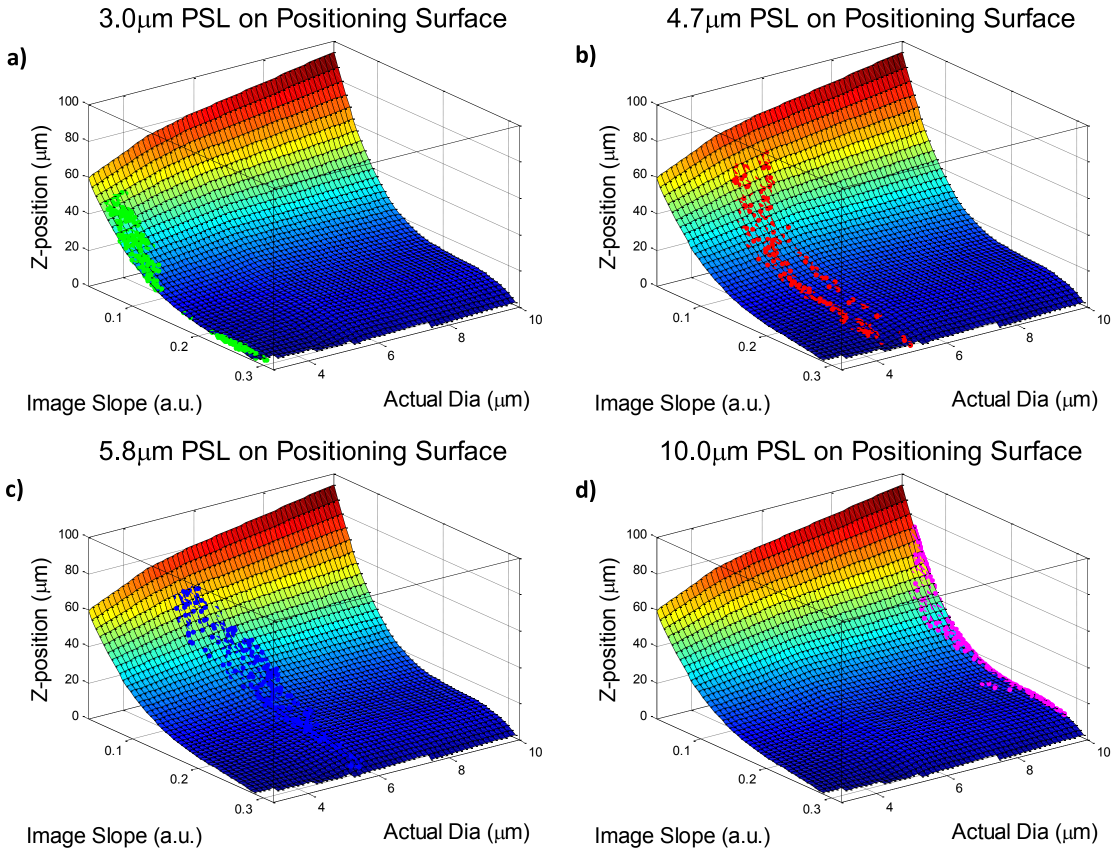
3.0μm PSL on Positioning Surface

4.7μm PSL on Positioning Surface

5.8μm PSL on Positioning Surface

10.0μm PSL on Positioning Surface

Figure 48. Positioning calibration surface for PSL particles of a) 3.0 μm, b) 4.7 μm, c) 5.8 μm, and d) 10.0 μm diameter[28].

The resulting combinations of image size and image slope were input into the calibration surface and the diameter calculated. Sized experimental particles of size 3.0 μm, 4.7 μm, 5.8 μm and 10 μm are as shown in Figure 47. a), b), c), and d), respectively.

The z-positioning calibration surface was created and tested in a similar manner. Because the images were acquired beginning in the blurry region, then stepped far into the diffraction region, the z = 0 μm position for each particle must be found. This was accomplished by examining the image size image slope pairs for all the calibration images. Because the steepest image slope and smallest image size did not always occur in the same image, image size was ultimately used to identify the z = 0 μm position. Some discretion was required when particles had image sizes which did not change significantly from one image to the next. In these cases the maximum image slope was selected. Once the z = 0 µm image was identified, the data for images in the blurry region were removed, and the correct z-position assigned for the data in the diffraction region. The positioning surface, Figure 48 was then created using the Surface Fitting toolbox in Matlab, where the x-input, y-input and z-output were, image slope, actual diameter and z-position, respectively. After creating the positioning surface, the image size and slope pairs of the experimental data were measured, and the sizing surface was used to calculate the actual diameter. This data was input into the positioning surface and the z-positions calculated. The accuracy of the positioning surface was checked against the experimental z-positions which were corrected in the same manner as the calibration data.

After thoroughly investigating the PSL with the SPSA, silica particles were sized on the calibration curve generated from PSL data. Using the same methods as PSL, trends relating image size and image slope were obtained. The silica particles were obtained from Cospheric Inc. (Santa Barbara, CA, USA). The average diameter as confirmed by SEM imaging is 3.8 µm. Specifications from the manufacturer sized the particles at 4.0 µm ±10%. Because of this dispersity, the particles were filtered in two ways: First particles with concentricity less than 85% were removed. Second, only particles within 2% of the mean image size (4.3 µm) were included. This assures that only very similar silica particles were include in this testing of the SPSA. It was found the silica followed a different trend than the PSL. This difference caused silica to be slightly under-sized near the depth of field, correctly-sized at image slopes near 0.2, and over-sized at image slopes above 0.2 as shown in Figure 49.

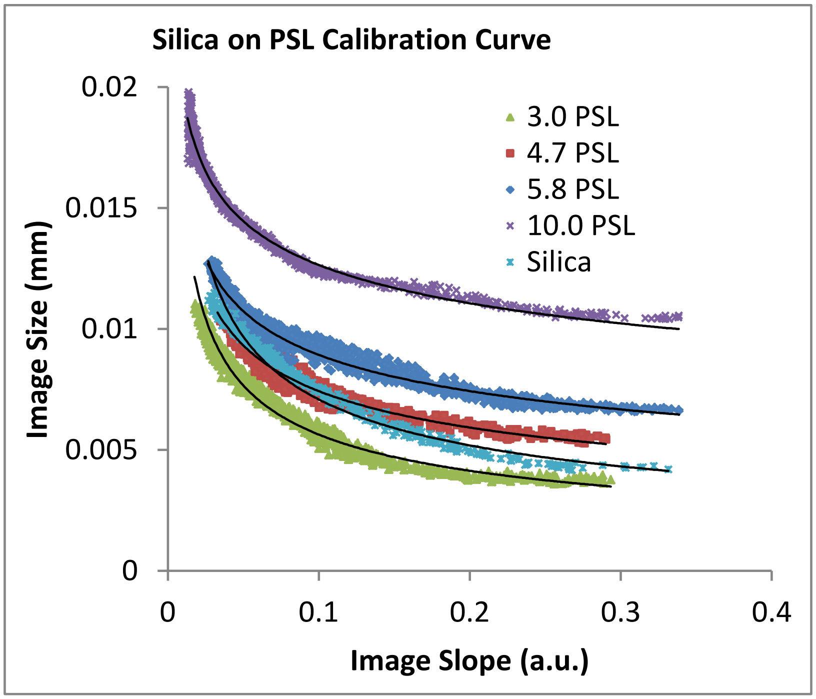

Figure 49. Graph of Image size vs. image slope for 3.8 µm silica spheres plotted on the PSL calibration curve[28].

Table 9 and Table 10 show the accuracy of the sizing and positioning surfaces for PSL experimental data. The largest sizing error was found in the 4.7 and 5.8 µm particles. The 10 µm particles were sized the most accurately. It appears that larger particles may be sized more accurately than small particles. This may be attributed to the fact that at equal magnifications large particles have more edge pixels when compared to smaller particles. During the creation of the radial diffraction profile, this would lead to more data included in the averaging and therefore more consistent results. Additionally, the 4.7 µm particles seemed to have visible differences when comparing two particles of the same diameter. Specifically, some particles seemed to have lower concentricity than the other particle sizes. Even with averaging this may cause the particles image size to be altered. However, the extent to which this affects the results was not discovered. The silica particles exhibited in-focus criteria relationships which crossed between the 4.7 µm PSL trend line. This may be attributed to a surface roughness in silica than PSL. It may be possible to create a calibration surface for silica in the same manner as PSL if different sizes of silica are available.

Table 9. Accuracy of Sizing Surface[28].

	3 µm	4.7 µm	5.8 µm	10 µm
Mean Size (µm)	3.29	5.01	5.77	9.86
Mean Size % Error	9.6 %	6.6 %	0.5 %	1.4 %
Std. Dev. (µm)	0.18	0.35	0.35	0.18

Table 10. Accuracy of Positioning Surface[28].

	3 µm	4.7 µm	5.8 µm	10 µm
Std. Dev. (µm)	1.05	2.71	2.75	2.07

Figure 50 shows the relationship between the actual particle positing in the z-axis and the position as calculated by the positioning algorithm. This relationship is approximately 1:1 for all particle sizes.

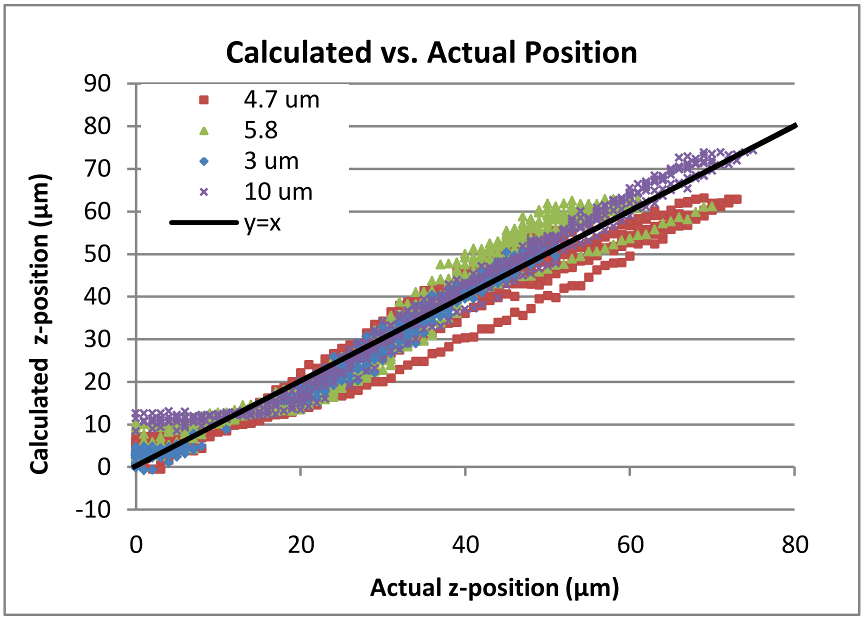

Figure 50. Graph showing relationship of actual z-positong and calculated z-postiong for 3.0 4.7 5.8 and 10.0 µm PSL particles[28].

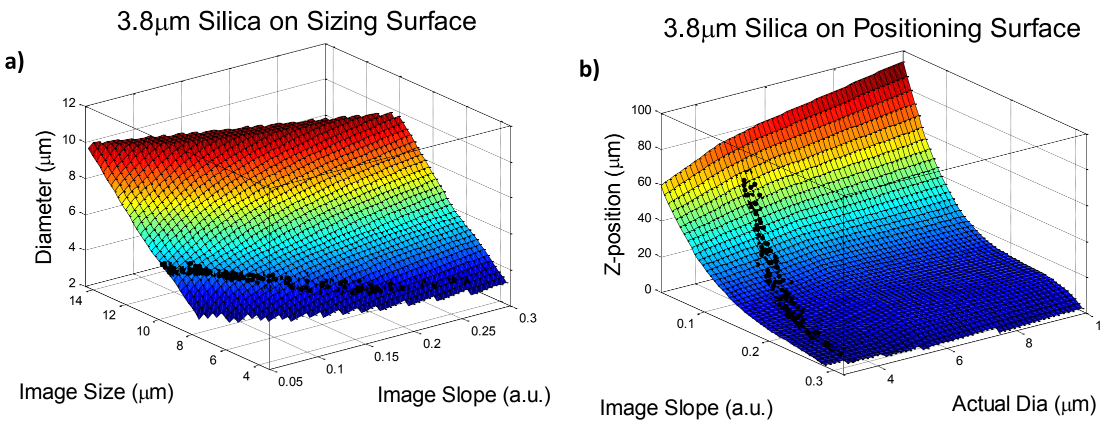

Figure 51. Silica particles on positioning surface[28].

Figure 51 shows the 3.8μm silica particles on the positioning surface. Unlike the trends for the PSL on the positioning surface, the silica does not follow a line of constant diameter. As noted previously, the sizing surface under sizes in focus particles and over sizes out of focus particles. This error is illustrated in the positioning surface as the actual diameter increases with z-position.

A small particle sizing algorithm was developed which has the capability to both size and position particles. Through the use of the sizing algorithm and the positioning algorithm, SPSA has the unique ability to determine size and position relative to the depth of field of PSL particles between 1 μm and 10 μm in diameter. Experimental mean particle size differed from actual size by a range of 0.5% to 9.6%, where generally, larger particles were sized more accurately than smaller particles. Experimental mean positioning error ranged from 1.79 μm to 3.93 μm and was not related to particle size, except at the object plane where smaller particles were more accurately positioned than lager particles. When silica particles were sized on a PSL calibration curve they displayed slightly different trends than PSL. These results may have a large benefit to the aerosol community for the visualization of micro aerosol flows and ultimately lead to a better understanding of the fluid-particle interactions in aerosol focusing.

3.7.3. Beam Characterization

Because the SPSA was determined to be material dependent, (the silica and PSL spheres displaying different trends), it was inappropriate to use the PSL calibration curves to size and or position the silica spheres. Likewise it would be in poor practice to use the SPSA to size liquid ink spheres until further testing can be performed. It is likely possible to create a silica calibration curve for particle sizing with silica particles of various sizes but as the silica is already monodisperse, creating a sizing calibration is not beneficial. However, the SPSA may still be utilized to position silica particle in the z-axis. This would allow for generation of a 3-D visualization of the particle beam.

4. ALTERNATIVE NOZZLE GEOMETRIES

Initial results from shadowgraphy and Mie scattering experiments showed that Stokes was the primary focusing force, and that Saffman force was negligible. Before Saffman force could be conclusively disregarded, it was important to check a scenario where it would be more pronounced. Attaching a straight capillary to the linear converging section provided this scenario. Compared to the linear converging nozzle alone, adding the straight section would cause minimal change in the particle beam width due to Stokes force. However, if Saffman force was present, the beam width would be noticeably thinner.

Peek couplers were used to join the linear converging nozzle to the straight capillaries. Initially the smaller 200 µm capillaries were used but perfect alignment was unachievable. This resulted in abrupt edges which disturbed the flow and ruined results. The larger 264 µm inner diameter capillaries were used instead. The capillaries and couplers are shown in Figure 52.

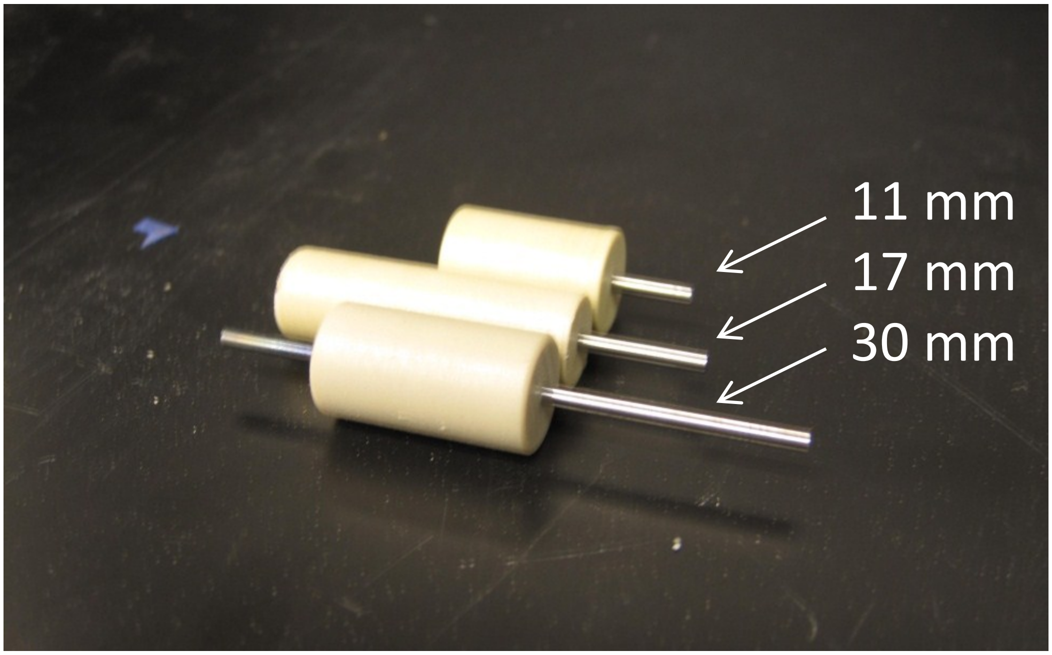

Figure 52. 264 µm capillaries coupled with linear converging nozzles.

The inner geometry of the linear converging nozzle coupled with the straight section is illustrated in Figure 53 where the y-axis is the radial distance from the center line. The blue lines represent particle trajectories if only Stokes force is applied. As expected the blue lines focus a very small amount while traveling through the capillary showing that focusing due to Stokes force is not increased by adding the straight section. The red lines in Figure 53 a) are the particle trajectories if both Stokes and Saffman forces are applied. The green lines in Figure 53 b) are the particle trajectories if both Stokes and 22% of Saffman forces are applied. This 22% is the required correction factor to make the model match the experimental results. It should be noted that experiments were only run for the 30 mm nozzle because this is where the difference between Stokes and Stokes + Saffman force would be the largest.

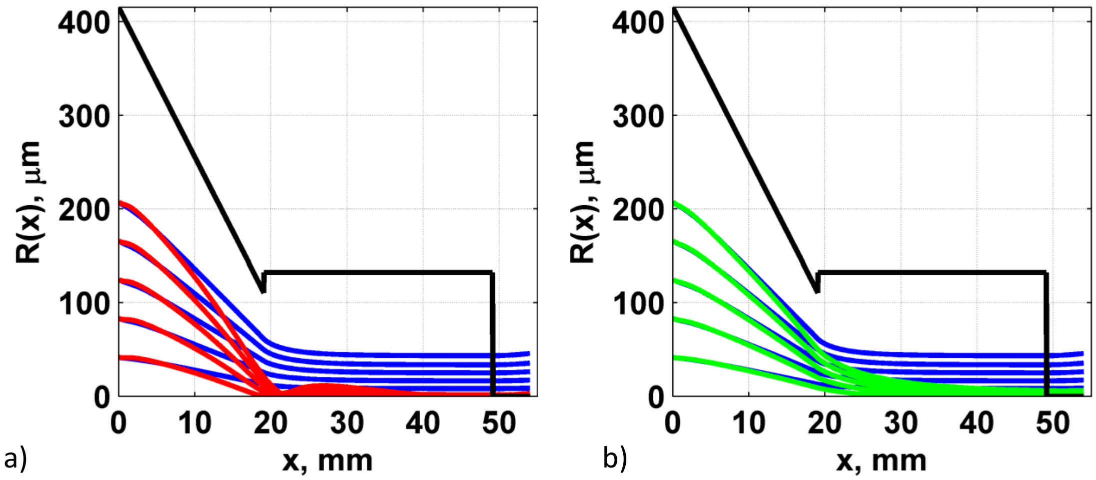

Figure 53. Images showing geometry of linear converging nozzle with attached 30 mm straight section. Blue lines are particle trajectories with only Stokes force applied. a) Red lines are particle trajectories with Stokes and Saffman force present. b) Green lines are particle trajectories if Stokes and 22% of Saffman force is applied.

The Mie scattering technique was used to acquire the experimental data for beam widths using the linear converging nozzle coupled with a 30 mm straight capillary. These results were repeated for three experiments and averaged. Due to the small beam widths the beam widths were first calculated then averaged as described in section 3.5.1. The experimental results and the theoretical results are plotted in Figure 54.

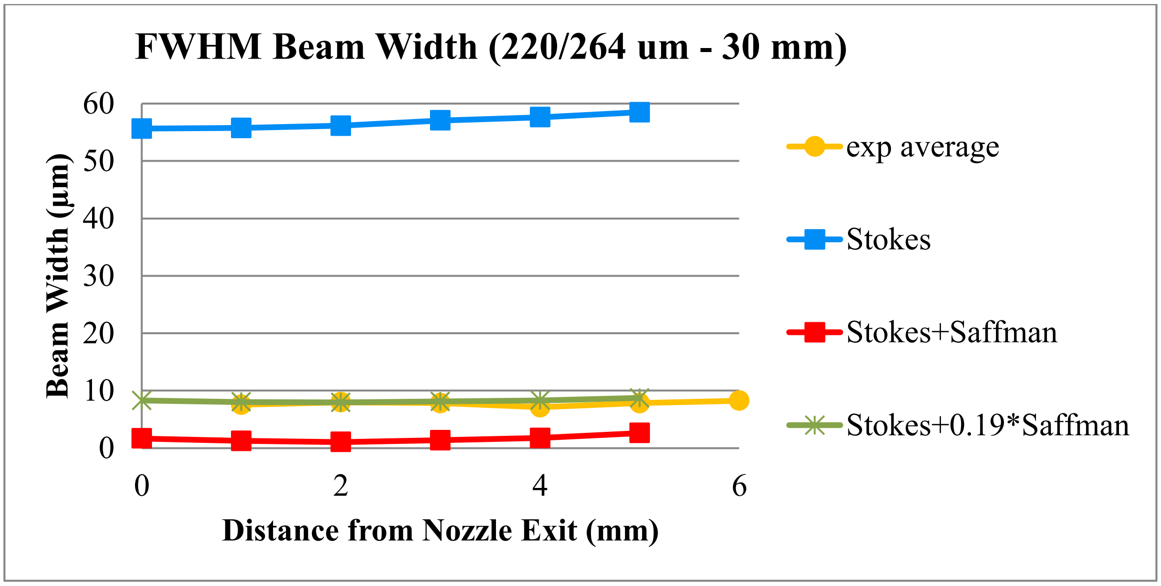

Figure 54. Graph of experimental beam width results via scattering technique compared to modeling results.

As mentioned previously, applying full Saffman force causes the model to over predict the focusing of the particles. It was found that for the given nozzle geometry, flow and particles size, a 19% correction factor was appropriate. This correction factor may not be universal and more experiments are required to determine if and how the correction factor is related to particle size, flow rate, and nozzle geometry.

In addition to testing the Linear converging nozzle with capillaries attached, the ceramic nozzle was coupled with a number of straight sections. This was done for three reasons. First, the ceramic nozzle allowed testing of a different inner nozzle diameter and fit more easily with the small 200 µm capillaries as their outer diameters were approximately the same. Secondly, ceramic nozzles were available where the nozzle exit diameter was small enough that they could be used with the 200 µm capillaries without creating an abrupt edge allowing for variation of the inner diameter of the capillary. Third, capillary length was varied from 11 to 17 to 30 mm. The geometry of the ceramic nozzle coupled with the 30 mm straight section is illustrated in Figure 55.

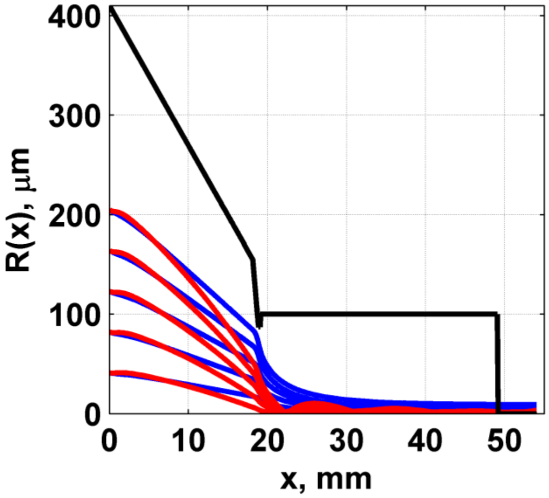

Figure 55. Image of a 175 µm ceramic nozzle coupled with a 30 mm 200 um inner diameter straight section. Blue lines represent particle trajectories with Stokes force only. Red lines represent particle trajectories with both Stokes and Saffman force.

The experimental results for a 175 µm ceramic nozzle coupled with three different lengths of straight capillaries flowing silica particles at 120 sccm are presented in figures Figure 56, Figure 57 and Figure 58 .

Figure 56 shows both shadowgraphy and Mie scattering results. The shadowgraphy results are close to the beam widths as measured by Mie scatting but have large fluctuations in beam widths. This is primarily due to the relatively small amount of data that was collected. The histograms created had bins with less than 10 particles in the peak bin. More data collection would result in a more accurate histogram and therefore a more accurate and smoother beam width line. Because the inlet conditions were not consistent, the results for Stokes force are plotted for inlet condition where particle occupy both 50% and 40 % of the nozzle inlet.

Figure 56, shows that the geometry is accurately predicted by Stokes force only and that the change in inlet conditions can could be the cause for any discrepancies between the model and the experiments.

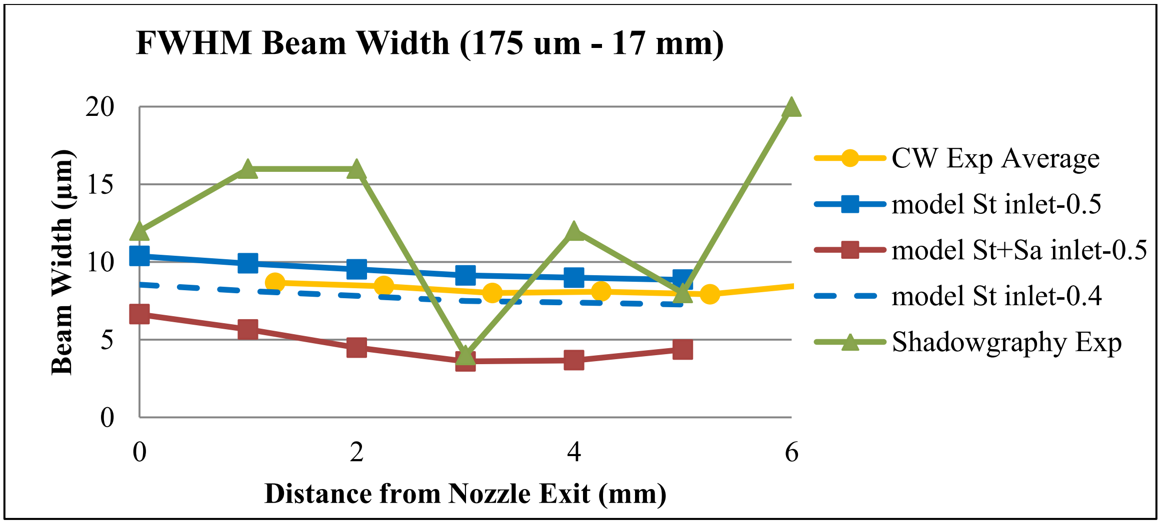

Figure 56. Graph of experimental beam widths via shadowgraphy and Mie scattering compared to modeling results for 175 µm ceramic nozzle coupled with 17 mm capillary.

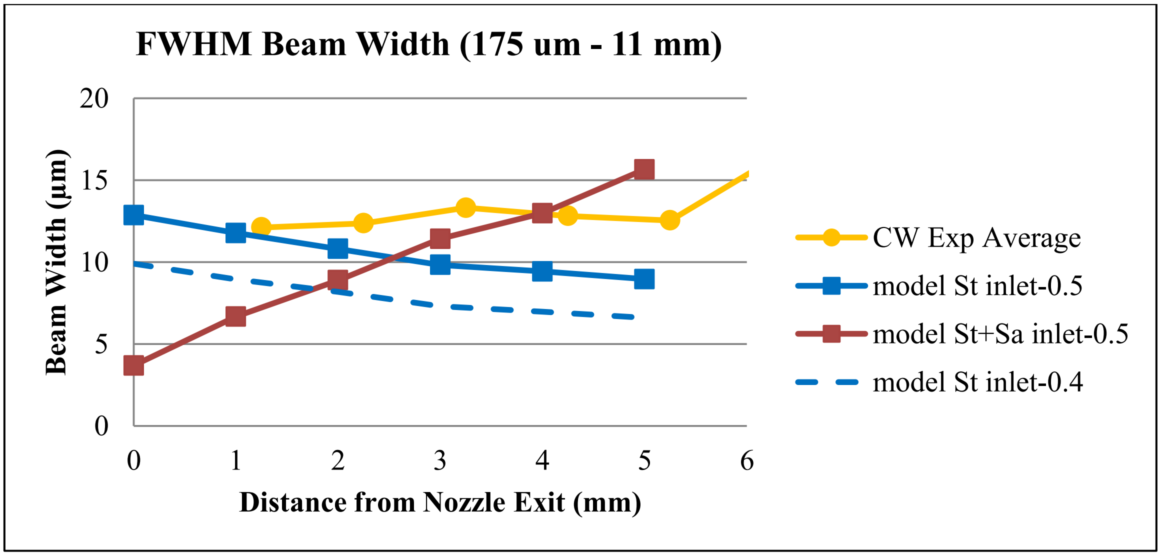

Figure 57. Graph of experimental beam widths via Mie scattering compared to modeling results for 175 µm ceramic nozzle coupled with 11 mm capillary.

Figure 57 shows that Stokes force alone predicts that the particles should be focusing, whereas, the experimental and the Stokes + Saffman results show/predict a beam that is diverging.

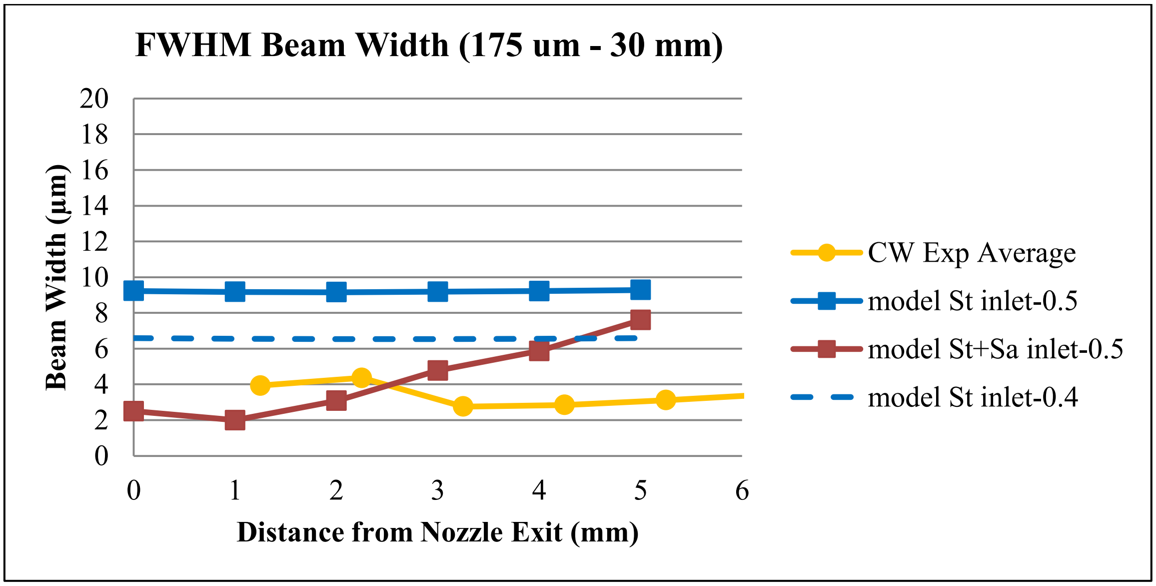

Figure 58. Graph of experimental beam widths via Mie scattering compared to modeling results for 175 µm ceramic nozzle coupled with 30 mm capillary.

Finally, Figure 58 shows that together Stokes and Saffman force accurately predict the beam width but predict a divergence not seen in experiments. Stokes force alone predicts a collimated beam, but over predicts beam width as the experimental results are outside the deviations associated with inlet conditions. The experimental beam widths in this geometry illustrated a beam which was almost perfectly collimated. The width of the beam was the same as the width of the particles, approximately 4 µm. Although the particles were silica and cannot be used for printed electronics, it gives credence to the idea that it is possible to create an optimized geometry which could achieve perfect collimation and be used with conductive inks or powders.

5. SUMMARY AND RECOMMENDATIONS

Two shadowgraphy methods, Mie scattering and a particle sizing algorithm were investigated as to their ability to characterize particle beams generated by aerosol flow through micro-capillaries. Shadowgraphy was used successful to visualize silver ink particles from which data sets were generated during the slicing method experiments. Though this, the accuracy of centering with the CW laser was confirmed. Also, it was used to measure inlet conditions which were critical in the theoretical modeling. Additionally, shadowgraphy determined particle velocity confirming the models ability to predict the effect of Stokes force. Finally, it was used to determine beam widths generated by flowing silica particles through the various nozzles at multiple flow rates. Although shadowgraphy measures particle locations very accurately, processing beam widths requires a large amount of data. Additionally, data is acquired at a relatively slow rate and for that reason shadowgraphy should be used only to confirm Mie beam width results on an as needed basis. It is however invaluable, when measuring particle velocity, which does not require as large data sets for accurate results.

Mie scattering was shown to be a fast and effective method for gathering information regarding beam widths. It was successfully used to characterize beam widths from multiple nozzle geometries. Also it is an acceptable means by which the center of a particle beam can be identified. Although it is useful tool for measuring beam widths, it was not used for gathering particle velocity data. Mie scattering results showed that using a 175 μm ceramic nozzle coupled with a 30 mm straight section was sufficient to collimate 3.8 μm silica particles to a beam width consistent with their diameter.

A small particle sizing algorithm was developed which has the capability to both size and position particles. Through the use of the sizing and the positioning algorithm, the SPSA has the unique ability to determine size and position relative to the depth of field of PSL particles between 1 μm and 10 μm in diameter. Experimental mean particle size differed from actual size by a range of 0.5% to 9.6%, where generally, larger particles were sized more accurately than smaller particles. Standard deviation associated with positioning error ranged from 1.00 μm to 2.75 μm. When silica particles were sized on a PSL calibration curve they displayed slightly different sizing trends than PSL. It was determined that sizing silica with the PSL calibration curve was inappropriate but, it may be possible to position silica particles given that the particle diameter is known. This process should be tested and if successful would offer a method by which a 3D image of the particle beam could be created.

Both shadowgraphy and Mie scattering techniques were shown to produce similar results for a given experiment. This agreement from two experimental methods gives strong confidence in the acquired results. Further experiments should be performed where nozzle geometry, flow rates and particle size are varied to investigate how these parameters affect the Saffman correction factor. Although the resulting beam widths left unanswered questions regarding the extent of the roles Stokes and Saffman forces play in particle focusing, the measurement techniques accurately measured beam widths and particle velocities confirming their ability to be used as aerosol characterization methods.

6. REFERENCES

1. K. K. B. Hon, L. Li, and I. M. Hutchings, "Direct writing technology—Advances and developments," *CIRP Annals - Manufacturing Technology,* vol. 57, pp. 601-620, 2008.
2. J. M. Hoey, A. Lutfurakhmanov, D. L. Schulz, and I. S. Akhatov, "A review on aerosol-based direct-write and its applications for microelectronics " *Journal of Nanotechnology,* vol. 2012, pp. 1-22, 2012.
3. Y. T. Gizachew, L. Escoubas, J. J. Simon, M. Pasquinelli, J. Loiret, P. Y. Leguen, J. C. Jimeno, J. Martin, A. Apraiz, and J. P. Aguerre, "Towards ink-jet printed fine line front side metallization of crystalline silicon solar cells," *Solar Energy Materials and Solar Cells,* vol. 95, Supplement 1, pp. S70-S82, 2011.
4. M. Lejeune, T. Chartier, C. Dossou-Yovo, and R. Noguera, "Ink-jet printing of ceramic micro-pillar arrays," *Journal of the European Ceramic Society,* vol. 29, pp. 905-911, 2009.
5. J. Zhang, X. Li, X. Shi, M. Hua, X. Zhou, and X. Wang, "Synthesis of core–shell acrylic–polyurethane hybrid latex as binder of aqueous pigment inks for digital inkjet printing," *Progress in Natural Science: Materials International,* vol. 22, pp. 71-78, 2012.
6. Z. Bao and J. A. Rogers, "Thin-film Transistors From Organic Semiconducting Materials, Processing Technologies for," in *Encyclopedia of Materials: Science and Technology (Second Edition)*, K. H. J. B. Editors-in-Chief: , W. C. Robert, C. F.

Merton, I. Bernard, J. K. Edward, M. Subhash, and V. Patrick, Eds., ed Oxford: Elsevier, 2001, pp. 9319-9323.

7. J. D. Newman, S. F. White, I. E. Tothill, and A. P. F. Turner, "Catalytic Materials, Membranes, and Fabrication Technologies Suitable for the Construction of Amperometric Biosensors," *Analytical Chemistry,* vol. 67, pp. 4594-4599, 1995/12/01 1995.

8. E. W. C. Lim, S. Heng Koh, L. Kuang Lim, S. Hoon Ore, B. Kiat Tay, Y. Ma, and C.-H. Wang, "Experimental and computational studies of liquid aerosol evaporation," *Journal of Aerosol Science,* vol. 39, pp. 618-634, 2008.

9. J. Koch, S. Schlamp, T. Rösgen, D. Fliegel, and D. Günther, "Visualization of aerosol particles generated by near infrared nano- and femtosecond laser ablation," *Spectrochimica Acta Part B: Atomic Spectroscopy,* vol. 62, pp. 20-29, 2007.

10. J. Koch, S. Heiroth, T. Lippert, and D. Günther, "Femtosecond laser ablation: Visualization of the aerosol formation process by light scattering and shadowgraphic imaging," *Spectrochimica Acta Part B: Atomic Spectroscopy,* vol. 65, pp. 943-949, 2010.

11. J.-W. Lee, M.-Y. Yi, and S.-M. Lee, "Inertial focusing of particles with an aerodynamic lens in the atmospheric pressure range," *Journal of Aerosol Science,* vol. 34, pp. 211-224, 2003.

12. S. Fuerstenau, A. Gomez, and J. F. Delamora, "Visualization of aerodynamically focused subsonic aerosol jets," *Journal of Aerosol Science,* vol. 25, pp. 165-173, Jan 1994.

13. G. R. Toker and J. Stricker, "Holographic study of suspended vaporizing volatile liquid droplets in still air," *International Journal of Heat and Mass Transfer,* vol. 39, pp. 3475-3482, 1996.

14. R. Das and D. J. Phares, "Expansion of an ultrafine aerosol through a thin-plate orifice," *Journal of Aerosol Science,* vol. 35, pp. 1091-1103, 2004.

15. N. P. Rao, J. Navascues, and J. F. De la mora, "Aerodynamic focusing of particles in viscous jets," *Journal of Aerosol Science,* vol. 24, pp. 879-892, Oct 1993.

16. K.-S. Lee, S.-W. Cho, and D. Lee, "Development and experimental evaluation of aerodynamic lens as an aerosol inlet of single particle mass spectrometry," *Journal of Aerosol Science,* vol. 39, pp. 287-304, 2008.

17. W. H. Benner, M. J. Bogan, U. Rohner, S. Boutet, B. Woods, and M. Frank, "Non-destructive characterization and alignment of aerodynamically focused particle beams using single particle charge detection," *Journal of Aerosol Science,* vol. 39, pp. 917-928, 2008.

18. P. Liu, P. J. Ziemann, D. B. Kittelson, and P. H. McMurry, "Generating particle beams of controlled dimensions and divergence: 2. experimental evaluation of particle motion in aerodynamic lenses and nozzle expansions," *Aerosol Science and Technology,* vol. 22, pp. 314-324, Apr 1995.

19. Z. Mahmud, J. M. Hoey, A. Lutfurakhmanov, J. Daugs, O. F. Swenson, D. L. Schulz, and I. S. Akhatov, "Experimental characterization of aerosol flow through a micro-capillary," in *ASME Conference Proceedings*, Montreal, Canada, 2010, pp. 949-958.

20. K. S. Kim and S. S. Kim, "Drop Sizing and Depth-of-Field Correction in Tv Imaging," *Atomization and Sprays,* vol. 4, pp. 65-78, Jan-Feb 1994.

21. S. M. De Corso, "Effect of ambient and fuel pressure on spray drop size," *Trans. ASME J. Eng. Power,* vol. 82, pp. 10-18, 1960.

22. A. J. Yule, N. A. Chigier, and N. W. Cox, "Measurement of particle sizes in sprays by the automated analysis of spark photographs," in *Particle Size Analysis Proceedings of teh Analytical Division of the Chemical Society*, Univeristy of Salfor, 1978, pp. 61-73.

23. K. U. Koh, J. Y. U. Kim, and S. Y. Lee, "Determination of in-focus criteria and depth of field in image processing of spray particles," *Atomization and Sprays,* vol. 11, pp. 317-333, Jul-Aug 2001.

24. S. A. Schaub, D. R. Alexander, and J. P. Barton, "Theoretical-Model for the Image Formed by a Spherical-Particle in a Coherent Imaging-System - Comparison to Experiment," *Optical Engineering,* vol. 28, pp. 565-571, May 1989.

25. A. Lutfurakhmanov, "Fluid Dynamics of Material Micro-Deposition: Capillary-Based Droplet Deposition and Aerosol-Based Direct-Write," Doctoral of Science Dissertation, Mechanical Engineering, North Dakota State University, Fargo, ND, 2012.

26. I. S. Akhatov, J. M. Hoey, O. F. Swenson, and D. L. Schulz, "Aerosol flow through a long micro-capillary: collimated aerosol beam," *Microfluidics and Nanofluidics,* vol. 5, pp. 215-224, Aug 2008.

27. A. Vandenhoeck, "Product-Manual for DaVis 7.2," ed. Germany: Gottingen, 2008.

28. M. J. Robinson, "Development of a Small Particle Sizing Algorithm for sub-10 μm Particles using Shadowgraphy " in *Proceeding of IMECE 2012*, Houston, Texas, 2012.

29. N. Otsu, "Threshold Selection Method from Gray-Level Histograms," *Ieee Transactions on Systems Man and Cybernetics,* vol. 9, pp. 62-66, 1979.